



This is to certify that the

dissertation entitled

Half-life of 325; By Projectile Frament Implantation

presented by

Yuming Chen

has been accepted towards fulfillment of the requirements for

Ph.D degree in Physics

Date May 22, 1992

Majoroprofessor

An E Kashiy

0-12771

### LIBRARY Michigan State University

PLACE IN RETURN BOX to remove this checkout from your record. TO AVOID FINES return on or before date due.

DATE DUE	DATE DUE	DATE DUE

MSU Is An Affirmative Action/Equal Opportunity Institution

# HALF-LIFE OF <sup>32</sup>Si BY PROJECTILE FRAGMENT IMPLANTATION

 $\mathbf{B}\mathbf{y}$ 

Yuming Chen

#### A DISSERTATION

Submitted to
Michigan State University
in partial fulfillment of the requirements
for the Degree of

DOCTOR OF PHILOSOPHY

Department of Physics and Astronomy

1992

#### **ABSTRACT**

#### HALF-LIFE OF <sup>32</sup>Si BY PROJECTILE FRAGMENT IMPLANTATION

By

#### Yuming Chen

The experimental measurements of the half-life of <sup>32</sup>Si in the present work represent the first measurement of the half-life of <sup>32</sup>Si using an implantation method. Nuclei of <sup>32</sup>Si produced by the fragmentation of 65 MeV/A <sup>40</sup>Ar on Be were implanted into two Al foils in two separate experiments, with different methods of counting the number of nuclei implanted and of measuring their activity. In the first experiment, a total of 6.7×10<sup>8</sup> 32Si nuclei were implanted into an Al foil of 123 mg/cm<sup>2</sup> thick, and in the second experiment, a total of 7.7×10<sup>8</sup> 32Si nuclei were implanted into an Al foil with a thickness of 247 mg/cm<sup>2</sup>. The two Al foil samples were counted in a low background environment. The detection efficiency of the counting system in the first experiment was based on the activity of <sup>31</sup>Si nuclei. In the second experiment, the efficiency of the counting system was obtained by measuring the activity of implanted <sup>32</sup>P nuclei. The half-life for <sup>32</sup>Si obtained was 132±12 years. To get the reaction yield of <sup>32</sup>Si for implantation, the momentum distributions of projectile fragments in the reaction of 80 MeV/A <sup>40</sup>Ar on Be and Ta at 0° were measured. These were compared with model calculations. The agreement in reaction cross sections between the experiment and calculation was found to be within a factor of three. Some disagreement in the shape of the isotope distribution was also found.

# Contents

LI	IST OF TABLES				
LI	ST (	OF FIGURES	v		
1	Intr	roduction	1		
	I	<sup>32</sup> Si half-life	1		
	II	Momentum distribution	6		
2	Exp	perimental devices	9		
	I	Background and the Activity Determination	9		
	II	A1200	19		
	III	The devices for implantation	31		
3	Exp	perimental Setup	34		
	I	The Implantation	34		
	II	Momentum Distribution	57		
	III	Counting	60		
4	Ana	alysis	80		

	I	<sup>32</sup> Si half-life	80
	II	Momentum distributions	105
5	Cor	nclusion	125
	I	<sup>32</sup> Si half-life	125
	II	Momentum distribution	126
LI	ST (	OF REFERENCES	130

# List of Tables

2.1	Background rate measured by Si detector (above 200 KeV)	17
4.1	Number of radioactive nuclei in the sample as 7PM 2/26/91	87
4.2	Number of nuclei of various isotopes implanted in the samples	94
4.3	The measured count rate of <sup>32</sup> P source	100
4.4	The measured decay rates of the 32P source with different conditions	•
	at different time	101
4.5	Uncertainties in half-life determination (from different sources)	104
4.6	Calibration parameters for positions measured by PPAC 2	106

# List of Figures

1.1	Summary of half-life measurements of <sup>32</sup> Si. The results are labeled	
	by the method or the respective natural reservoir, and by the half-life	
	value in years	,
2.1	Decay scheme of <sup>32</sup> Si nuclei from [Bro 86]	11
2.2	Calculated energy spectrum of electrons from the decay of $^{32}P$	i
2.3	The calculated decay rates of <sup>32</sup> Si and <sup>32</sup> P as functions of time. Assum-	
	ing the half-life of <sup>32</sup> Si is 100 years, initially, there are no <sup>32</sup> P nuclei,	
	and there are $8\times10^8$ 32Si nuclei at the beginning	14
2.5	Shielding arrangement to reduce the background for the activity counter.	18
2.6	Schematic setup of electronic modules for activity determination	20
2.7	Background energy spectra taken by the two activity counters,[a.) is	
	taken by detector 1, b.) taken by detector 2.]	21
2.8	Background time spectra taken by the two activity counters, [a.) is	
	taken by detector 1, b.) is taken by detector 2]	22
2.9	A schematic drawing of the A1200 analyser	24

2.10	The principle of resistive charge division for position measurements.	
	The charge of an electron avalanche, created by a fast charge particle	
	entering the gas volume of the detector, is collected by a series of	
	anode strips which are connected in series with resistors. the charge is	
	split into two fractions, which propagate towards the two ends of the	
	resistor series. The ratio of the signals at the ends of the resistor series	
	is directly related to position	29
2.11	Schematic diagram of the standard electronic setup for experiments	
	using the A1200. Where ADC: analog-to-digital converter, CFD: con-	
	stant fraction discriminator, FA: Fast amplifier, GDG: gate and de-	
	lay generator, QDC: Charge-to-digital converter, TAC: time-to-analog	
	converter, TFA: timing filter amplifier,	30
2.12	a.) Schematic arrangement of the absorber foil, mesh and detectors b.)	
	Schematic drawing of the collimator frame used to hold mesh, Al foil	
	and Si detector during implementation	33
3.1	Calibration of the PIN diode with the beam, the vertical axis is the	
	energy loss signal of the beam from the PIN diode detector, horizontal	
	axis is the time-of-flight signal	37
3.2	Particle identification histogram. Vertical axis is energy loss of the	
	particles in the PIN diode detector, horizontal axis is time-of-flight	39
3.3	The collection rate of <sup>32</sup> Si nuclei as a function of the dipole field	40
3.4	Particle identification histogram when degrader is used	42
3.5	The position of <sup>32</sup> Si nuclei measured by PPAC 2	43
3.6	Particle identification histogram measured by the monitor detector	45

3.7	Particle identification spectrum measured by the stopping detector	46
3.8	Energy loss spectrum measured by stopping detector	48
3.9	Schematic drawing of the collimator for yield monitor	49
3.10	PID spectrum with magnetic field set for 32P implantation (without	
	degrader)	51
3.11	PID spectrum with magnetic field set for 32Si implantation (without	
	degrader)	52
3.12	PID spectrum with magnetic field set for <sup>32</sup> P implantation (with de-	
	grader)	53
3.13	PID spectrum with magnetic field set for <sup>32</sup> Si implantation (with de-	
	grader)	54
3.14	Measured ratio R(as defined in the text) as a function of beam atten-	
	uation factor before the implantation of <sup>32</sup> P	55
3.15	Measured ratio R(as defined in the text) as a function of beam atten-	
	uation factor before the implantation of <sup>32</sup> Si	56
3.17	Beam positions measured by PPAC1 at image #2 with different field	
	settings	61
3.18	A typical PID histogram during the momentum distribution measure-	
	ment	62
3.19	Actual field setting covered during the momentum distribution mea-	
	surement	63
3.20	Detector arrangement for activity determination	64
3.21	a.) 122 KeV line of the <sup>57</sup> Co measured by detector 1, b.) 356 KeV line	
	of the <sup>133</sup> Ba source measured by the same detector	65

3.22	Background events with energy deposition greater than 100KeV as a	
	function of time.	67
3.23	number of events measured (when the sample was between the two	
	counters) as a function of time immediately after the first implantation	68
3.24	Number of events measured (when sample was between the counters)	
	as a function of time(60 days after the implantation)	69
3.25	Background events as a function of time after the modification of the	
	sample holder and shielding	71
3.26	Measured average background count rates with different threshold as	
	a function of time	72
3.27	Number of events as a function of time (when sample P <sub>1</sub> was between	
	the counters)	73
3.28	Number of events as a function of time (when sample P2 was between	
	the counters)	74
3.29	The average count rates of sample P <sub>1</sub> with different thresholds as a	
	function of time	75
3.30	The average count rates of sample P2 with different threshold as a	
	function of time	76
3.31	The average count rates of sample Si with different thresholds as a	
	function of time.	78
3.32	The number of events as a function of time measured the two counters	
	(when the Si sample was between the counters. Threshold 100 KeV).	79

4.1	The energy deposition of particles in the stopping detector v.s. the	
	time-of-flight of the particles. The groups with higher energy deposi-	
	tions are those particles that were stopped in the detector the groups	
	with lower energies are those particles that penetrated the stopping	
	detectors	81
4.2	Simulated energy deposition of <sup>32</sup> Si nuclei in the stopping detector	83
4.3	measured energy deposition of <sup>32</sup> Si nuclei in the stopping detector	84
4.4	Energy loss spectrum of <sup>32</sup> Si nuclei measured by the PIN diode detector	86
4.7	Simulated energy loss (in the activity counter) spectrum of electrons	
	from the decay of <sup>32</sup> P	91
4.8	measured energy loss (by detector 1) spectrum of electrons from the	
	decay of <sup>32</sup> P source (subtract background)	92
4.9	The decay rate of $^{32}P(\text{count rate - background rate})$ in sample $P_1$	96
4.10	The decay rate of $^{32}P(\text{count rate - background rate})$ in sample $P_2$	97
4.11	The decay rate (count rate - background rate) of sample Si	98
4.12	The number of events measured by the two counters as a function of	
	time(after Al foils were added to equalize the count rates of the sample	
	P <sub>1</sub> measured by the two detectors)	99
4.13	The relative efficiency E, defined in the text as a function of the thick-	
	ness of Al foils that separate the <sup>32</sup> P nuclei from the detector 1	02
4.14	The relative efficiency of the PPAC 1 as a function of channel number 1	06
4.15	The PID histogram and the gates corresponding to different isotopes	07
4.16	The position spectra of <sup>32</sup> P nuclei measured by PPAC 1 at image #2.	
	Target: Be, the dipole field of the first half of the A1200 B = 0.780 T 1	08

4.17	Measured momentum distributions of $A=32$ nuclei from the reactions	
	of 80 MeV/A <sup>40</sup> Ar on Be and Ta. The points with error bars are data	
	points from the experiment and the solid line curves are fitted Gaussian	
	distributions	110
4.18	The widths of momentum distributions of different isotopes as a func-	
	tion of number of nucleons removed from the projectile. The data	
	points represented by different symbols with error bars are the mea-	
	sured widths in the experiment with Be target and the solid line is	
	from the calculation of Goldhaber model using the measured Fermi	
	momentum value of $^{40}$ Ar $p_{Fermi} = 251$ MeV/c. The dotted line is a	
	leastsquare fit of the data based on the Goldhaber model with a fitted	
	$\sigma_0 = 89 MeV/c$	112
4.19	The widths of momentum distributions of different isotopes as a func-	
	tion of number of nucleons removed from the projectile. The data	
	points represented by different symbols with error bars are the mea-	
	sured widths in the experiment with Ta target and the solid line is	
	from the calculation of Goldhaber model using the measured Fermi	
	momentum value of $^{40}$ Ar $p_{Fermi} = 251$ MeV/c. The dotted line is a	
	leastsquare fit of the data based on the Goldhaber model with a fitted	
	$\sigma_0 = 68 MeV/c$	113
4.27	The centroids of the momentum distributions(in p/A) of various iso-	
	topes relative to the beam momentum/nucleon as function of projectile	
	mass loss. The solid line represent the beam momentum/nucleon mea-	
	sured in the experiment with the same target. the dotted line is from	
	the program calculation	123

١.

4.28	The centroids of the momentum distributions(in p/A) of various iso-	
	topes relative to the beam momentum/nucleon as function of projectile	
	mass loss. The solid line represent the beam momentum/nucleon mea-	
	sured in the experiment with the same target. the dotted line is from	
	the program calculation	124
5.1	Summary of half-life measurements of <sup>32</sup> Si. The results are labeled	
	by the method or the respective natural reservoir, and by the half-life	
	value in years. The results except those from this experiment is taken	
	from [Kut 91]	127

• .

.

# Chapter 1

### Introduction

This introduction consists of two parts. In the the first part, the motivation for measuring <sup>32</sup>Si half-life is discussed, the current situation of <sup>32</sup>Si half-life is reviewed, and the results from various measurements with different methods are compared. In the second part, the reasons for making momentum distribution measurements of various isotopes are explored, and the experimental situation in this area is discussed.

### I <sup>32</sup>Si half-life

The nucleus <sup>32</sup>Si is of interest as a naturally occurring radioisotope produced in the atmosphere by spallation of <sup>40</sup>Ar with cosmic-ray protons. Its estimated production rate is about 10<sup>4</sup> times lower than that of <sup>14</sup>C and 10<sup>2</sup> times lower than that of <sup>10</sup>Be, The value of <sup>32</sup>Si for chronological applications has been limited by the large uncertainty in its half-life. Current estimates of its half-life from different methods range from 100 years to about 300 years [Kut 86, Mus 84, Elm 80, Kut 80, Duf 88, Zem 71, Cla 73, DeM 80, Alb 86, Kut 91]. In figure 1.1 (taken from [Kut 91]), various values of <sup>32</sup>Si half-life measured with different methods are plotted against the date of the measurements. As one can see from the figure, large uncertainty in single

measurement as well as disagreement between different measurements outside their respective uncertainties exist in the data.

To understand the methods used in the various measurements, let's summarize them briefly. The measurements in figure 1.1 are classified by the methods used in obtaining the <sup>32</sup>Si half-life. One can see a gap between those results labeled by 'AMS' and the other results mostly from geophysical measurements. Here 'AMS' stands for Accelerator Mass Spectrometry. Cyclotrons were used in most of those measurements to obtain the number of <sup>32</sup>Si nuclei in a sample. In the AMS measurements shown in figure 1.1, 32Si nuclei were produced in some nuclear reactions, for example  ${}^{37}\text{Cl}(p,2p\alpha){}^{32}\text{Si}, {}^{31}\text{P}(n,\gamma){}^{32}\text{P}(n,p){}^{32}\text{Si}$  [Hof 90]. The Si nuclei were separated from other reaction products by chemical means. The ratios of <sup>32</sup>Si/Si (often in the range of  $10^{-7}$ — $10^{-10}$ ) in the resulting samples were then measured using Accelerator Mass Spectrometry by accelerating Si ions produced from the sample to get the relative abundance of the isotopes. The resulting numbers of <sup>32</sup>Si nuclei in the sample is thus measured with typically less than 10 % uncertainty. Once that number is determined, the activities of the samples were then obtained by counting. Due to the small Q-value of  $^{32}Si(0.225 \text{ MeV})$ , it is difficult to detect the  $\beta^-$  particles from the decay of  $^{32}$ Si directly as many low energy  $\beta$  electrons can stop in the source. The counting of the samples is therefore done by detecting the  $\beta^-$  particles from the decay of <sup>32</sup>P which is the daughter of <sup>32</sup>Si. Since the half-life of <sup>32</sup>P (14.282 days) is much shorter than that of <sup>32</sup>Si(100-300 years), the decay chain <sup>32</sup>Si  $\rightarrow$  <sup>32</sup>P  $\rightarrow$  <sup>32</sup>S reaches equilibrium soon after the experiment(after 60 to 80 days). The decay rates of <sup>32</sup>Si nuclei can therefore be obtained by counting the electrons from the decay of <sup>32</sup>P in the sample after the above decay chain reaches equilibrium. The half-life of <sup>32</sup>Si can then be obtained using the following relation.

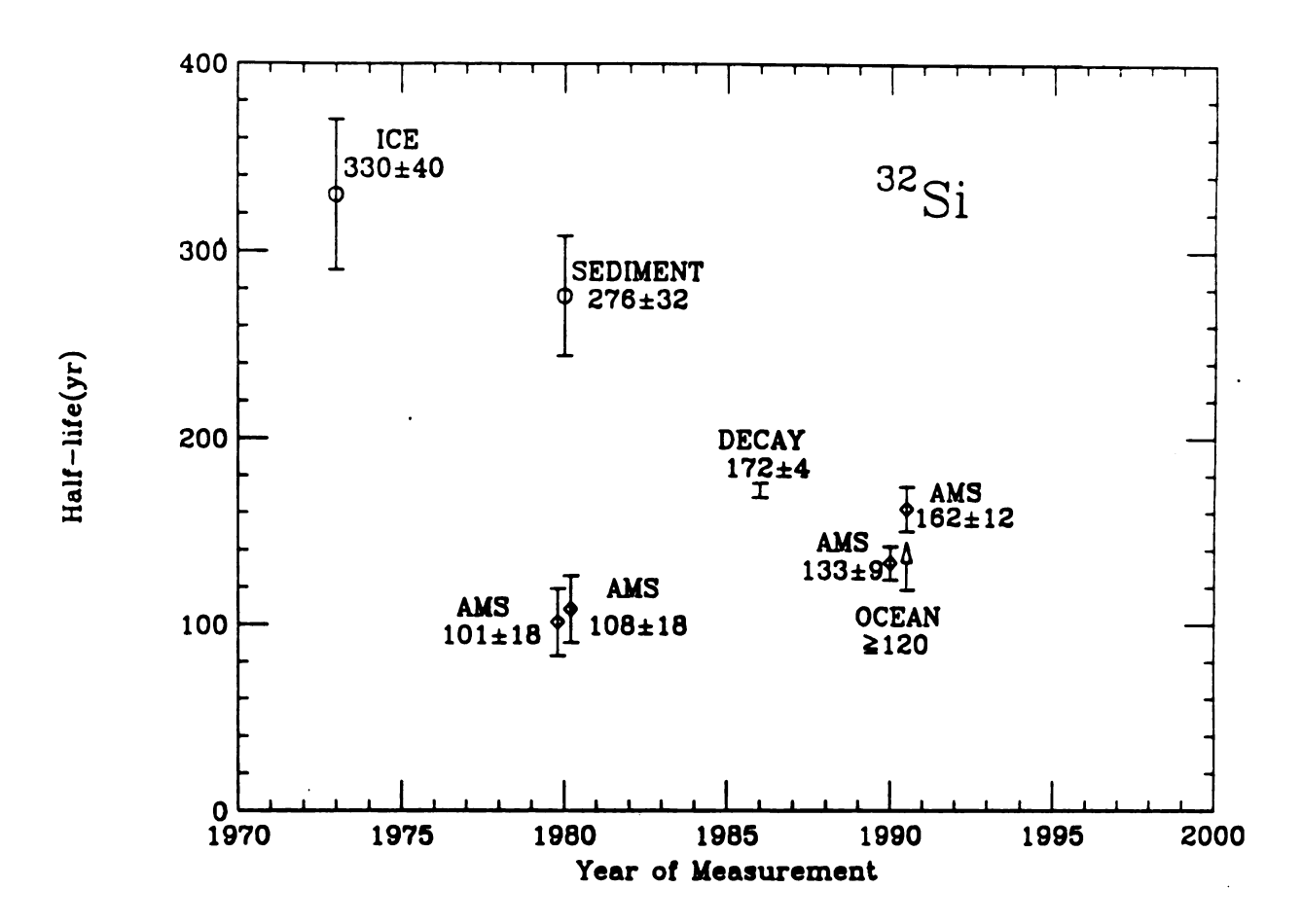


Figure 1.1: Summary of half-life measurements of <sup>32</sup>Si. The results are labeled by the method or the respective natural reservoir, and by the half-life value in years.

$$\frac{dN}{dt} = -\lambda N$$

where  $\lambda$  is the decay probability of <sup>32</sup>Si, N is the number of <sup>32</sup>Si nuclei at time t, and  $\frac{dN}{dt}$  is the decay rate of <sup>32</sup>Si at time t. The use of the above formula and the counting method is often referred as the 'Equilibrium' method[Kut 91]. In contrast, in the 'Decay' method the decay rates of the samples are monitored over a long period of time until the half-life of the nuclei can be extracted from the changes of the decay rates during that period. A real time 'Decay' measurement was carried out by Alburger et al[Alb 86] by following the activity of a 32Si sample over a period of four years. The activity was found to decrease by only 1.6 % during this period, and this required highly precise measurement of the activity. Most of the AMS measurements used 'Equilibrium' method with the exception of the measurement done by Thomsen et al[Tho 92]. The AMS method was used to determine the ratio of <sup>32</sup>Si/<sup>31</sup>Si. They then measured the activities of <sup>31</sup>Si and of <sup>32</sup>Si over a period of time in the sample. The main cause of difficulty in this method is the relatively short half-life of <sup>31</sup>Si (2.6 h), requiring large decay corrections to allow for the time elapsed in the chemical separation and the time required in measuring the isotope ratio. However the result agrees with the only real-time 'Decay' measurement. As can be seen from figure 1.1, the AMS measurements with the 'Equilibrium' method agree with one another within the relatively large uncertainties. But they clearly differ from geophysical results in ice and sediment, and also with real-time DECAY measurements of Alburger et al[Alb 86] and the AMS measurement by Thomsen et al[Tho 92]. The uncertainties with the AMS measurements mostly come from the determination of the ratio <sup>32</sup>Si/Si, in which the efficiency of the ion source, the chemical separation processes all contribute to the resulting uncertainties.

The results of three geophysical measurements are also shown in figure 1.1. Both 'Decay' and 'Equilibrium' methods in determining the half-life of <sup>32</sup>Si are represented. With the decay method, Clausen did one of the early measurements based on the specific activity of <sup>32</sup>Si as a function of depth in the ice cores from Greenland[Cla 73]. By assuming a nearly constant cosmic-ray flux, the half-life of <sup>32</sup>Si was determined. A similar measurement was done by DeMaster in a sediment core from the Gulf of California. With equilibrium method, a lower limit for the half-life was determined by Somayajulu et al from the comparison of the global <sup>32</sup>Si inventory of the oceans with with the average cosmic-ray production rate[Som 91]. However, the difficulties with geophysical measurements are that various uncontrollable factors such as temporal variations of the cosmic ray flux are involved and, due to the lack of data about those factors, various assumptions have to be made. Thus the resulting half-life may be subject to large uncertainties depending on the validity of the original assumptions.

The present investigation of the <sup>32</sup>Si half-life used a different experimental method from the previous ones. <sup>32</sup>Si ions produced by the projectile fragmentation reaction of an <sup>40</sup>Ar beam on a Be target are separated from other reaction fragments using the A1200 mass separator recently completed at the National Superconducting Cyclotron Laboratory (NSCL) [She 89]. As can be seen from the above discussion, if the number of <sup>32</sup>Si nuclei in the sample can be determined more precisely, the half-life of <sup>32</sup>Si can be more simply obtained. With the completion of A1200 mass separator at NSCL, the task of producing <sup>32</sup>Si nuclei in a projectile fragmentation and separating them from other reaction products can be carried out effectively. After the separation, those <sup>32</sup>Si nuclei can be implanted either in a detector or an Al foil which can be counted later to determine the activity. The number of <sup>32</sup>Si nuclei implanted can

be determined during the implantation by either counting a known fraction of the <sup>32</sup>Si nuclei implanted or monitoring the ratio of the number of <sup>32</sup>Si nuclei implanted to the integrated beam current passing through. Since the number of steps involved in producing, separating <sup>32</sup>Si and counting the number of <sup>32</sup>Si nuclei were reduced, smaller uncertainties in the number of <sup>32</sup>Si nuclei are expected. The detailed design of the experiment will be discussed in chapter 2

#### II Momentum distribution

To optimize the collection of <sup>32</sup>Si nuclei for the purpose of implantation, we need data about the production cross section of <sup>32</sup>Si in projectile fragmentation reaction, and knowledge of momentum distribution of <sup>32</sup>Si nuclei produced. There is not much systematic data about isotope and momentum distributions for projectile fragmentation reactions in the intermediate energy range (20 MeV/A-200 MeV/A) [Sou 91]. The systematic measurements available on isotope and momentum distribution for reaction fragments exist mainly for reaction with higher energies protons [Gol 78, Huf 85, Mor 89] and light ions [Hec 72, Gre 75, Viy 79]. The isotope and momentum distributions of target fragments (called spallation products) produced by high energy proton beams and that of the projectile fragments in light ion fragmentation reaction have been thoroughly studied. A rather complete parameterization of the variation has been established and several models have been successful in describing the observation [Gol 74, Oli 79, Mor 79, Fri 83 Sum 90]. At low energies, projectile-like products have also been observed, but the reaction mechanism is different. When the projectile nuclei undergo peripheral collisions with the target nuclei at low energy, the relatively low velocity of the nuclei allows a longer interaction time between the nucleon of the projectile and that of the target [Bon 71, Gel 78, McV 80, Ege 81,

Mur 83, Hom 84]. As a result, direct transfer, deep-inelastic and incomplete fusion reactions can take place. At intermediate energy, heavy-ion beams have become available only during the last few years. The few projectile fragmentation measurements available at the time were not adequate to provide a systematic parameterization and a clear understanding of this transition region[Gue 83, Blu 86, Bor 86, Baz 90]. In addition to the characteristics similar to those observed at higher energies, new features such as orbital deflection [Bib 79, Sil 88], and nucleon transfer(where one or more nucleons are picked-up by the projectile)[Bor 86, Sou 91] have been observed in peripheral collisions. Also, due to the lack of data, the only estimates of the yields and momentum distributions were based on extrapolations of the high energy parameterizations. For example, the computer code "INTENSITY" was developed here at NSCL [Win 91] to calculate the production rates of projectile fragments and help plan new experiments with the A1200. It was based on the parameterizations of Sümmerer and Morrissey [Sum 90] of high-energy fragmentation reactions. Therefore, to optimize the implantation of <sup>32</sup>Si and obtain more data for projectile fragmentation at intermediate energy, we have measured the momentum distribution of A = 32 nuclei in the projectile fragmentation of <sup>40</sup>Ar on Be and Ta target at 80 MeV/A. This work is a first attempt to measure the half-life of <sup>32</sup>Si with the implantation method, the procedures and results of the measurements are presented. In addition, data from the measurement of momentum distribution of some fragments produced in the above projectile fragmentation reaction are analysed, summarized and compared with theoretical results.

In chapter 2, the detailed design of the experiment such as detectors, electronics, the A1200, and the activity counting system are described. Various issues such as the number of <sup>32</sup>Si that should be implanted, the background reductions in the counting

system and whether to implant the <sup>32</sup>Si in an active detector or a passive foil are discussed.

In chapter 3, the experimental procedure for implantation, momentum distribution, and activity determination are described. Problems encountered during the experiments and the solutions are discussed.

indent In chapter 4, the analysis of the data is described, and results, are presented.

Finally, in chapter 5, the results of the experiments are compared with previous experiments and in the case of momentum distributions, also with the theoretical calculations. Conclusions about the results and directions for future improvements with the implantation method are discussed.

# Chapter 2

# Experimental devices

### I Background and the Activity Determination

As mentioned in the introduction, there are two ways to determine the half-life of an isotope, one is the 'Decay' method, another is the 'Equilibrium' method. With the decay method, the activity of the sample which contains the isotope is measured over a period of time until the change in the activity of the sample is large enough to allow a determination of the half-life. In this case, the number of nuclei of the isotope in the sample does not need to be known, since the change of the activity over time is enough to determine the half-life. With the Equilibrium method, the formula  $\frac{dN}{dt} = -\lambda N$  is used. One has to know the total number (N) of the nuclei in the sample and the decay rate  $\left(-\frac{dN}{dt}\right)$  of the isotope at a given time to calculate the half-life of the isotope. In the case of <sup>32</sup>Si which has a half-life of more than 100 years, the Decay method has the disadvantage of having to follow the the decay of the sample over a long period of time (several years at least) to obtain an accurate measurement. The slow change (long half-life) in the decay rate means that the measurement has to be precise and sensitive, and therefore difficult to carry out. With the Equilibrium method, there are two things that have to be determined accurately. The first one is the number of <sup>32</sup>Si nuclei in a sample, the other one is the absolute

decay rate of the sample. The two factors are also related, since if the number of <sup>32</sup>Si nuclei in the sample is small, the decay rate of the sample is also small, and may be even undetectable with a given background. Since the Equilibrium method was used to determine the half-life <sup>32</sup>Si in this work, those factors have to be considered. To determine the decay rate of the sample, a reliable counting system is required, and the background has to be accurately known.

The constraints on the counting system come from two factors; the first one is the requirement of long term stability of the counting system, and the second one is the need of low background. Those requirements are imposed on the counting system by the following considerations.

- Due to the limited number of <sup>32</sup>Si nuclei that were implanted in the experiments, the decay rate of those <sup>32</sup>Si in the sample is low, and therefore to make a statistically accurate measurement, one needs to count in a low background environment for a considerable amount of time.
- As shown in figure 2.1, <sup>32</sup>Si decays through β<sup>-</sup> emission to <sup>32</sup>P, which in turn decays to <sup>32</sup>S by emitting another electron. Since the Q-value of the <sup>32</sup>Si is only 0.225 MeV, it is hard to measure the electron from the decay of <sup>32</sup>Si directly, especially when the <sup>32</sup>Si nuclei are implanted in a passive foil. This problem can be solved by measuring the electrons from the decay of <sup>32</sup>P instead. Since the Q-value of <sup>32</sup>P is 1.71 MeV, most of electrons from the decay of <sup>32</sup>P are for more energetic (as shown in figure 2.2). However, as shown in figure 2.3, <sup>32</sup>P has a half-life of (14.282±0.005) days[Bro 86], and assuming there are no <sup>32</sup>P nuclei in the sample at the beginning, it will take almost 80 days for the decay

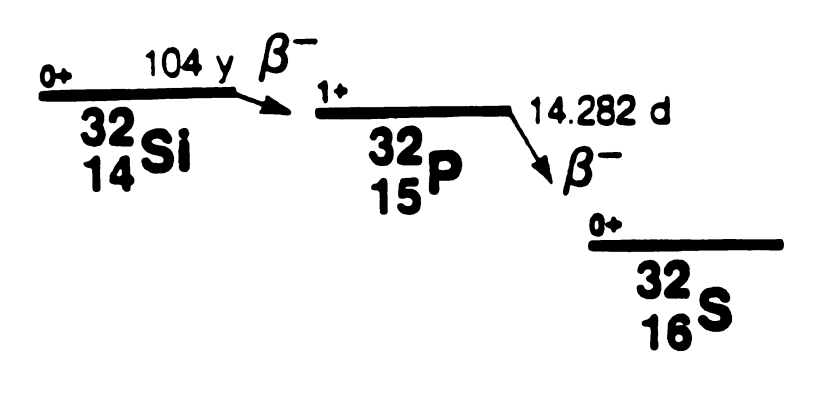


Figure 2.1: Decay scheme of <sup>32</sup>Si nuclei from [Bro 86].

chain  $^{32}\text{Si} \rightarrow ^{32}\text{P} \rightarrow ^{32}\text{S}$  to reach 98 % of equilibrium. Once the above decay chain reaches equilibrium, one can determine the decay rate of  $^{32}\text{Si}$  by measuring the decay rate of  $^{32}\text{P}$ . This delay from the time of implantation to the time of the activity measurement requires that the counting system to be stable over a long period of time so that we can follow the activity of the sample during this period.

In order to measure the half-life of <sup>32</sup>Si accurately, the number of <sup>32</sup>Si nuclei needed in a sample to guarantee a statistically sound activity determination was calculated before the experiment. This number depends on the background level and the counting method used. To have a suitable counting system for the above needs, a systematic background measurement using the same detectors as for the activity determination has to be performed. The initial detector tested for activity determination was a scintillator, because it has the following advantages.

- It can be made into different sizes easily, and <sup>32</sup>Si nuclei can be implanted directly into the detector, the activity can be measured with greater counting efficiency and the need of greater number of <sup>32</sup>Si nuclei due to detector efficiency loss is reduced.
- The detector can be duplicated easily, and the background of one detector can be compared and normalized to the other. This allows the simultaneous determination of background and activity after the implantation.

A large number of background measurements was made with different scintillator under different conditions. For example, with a cylindrical scintillator of 1.25

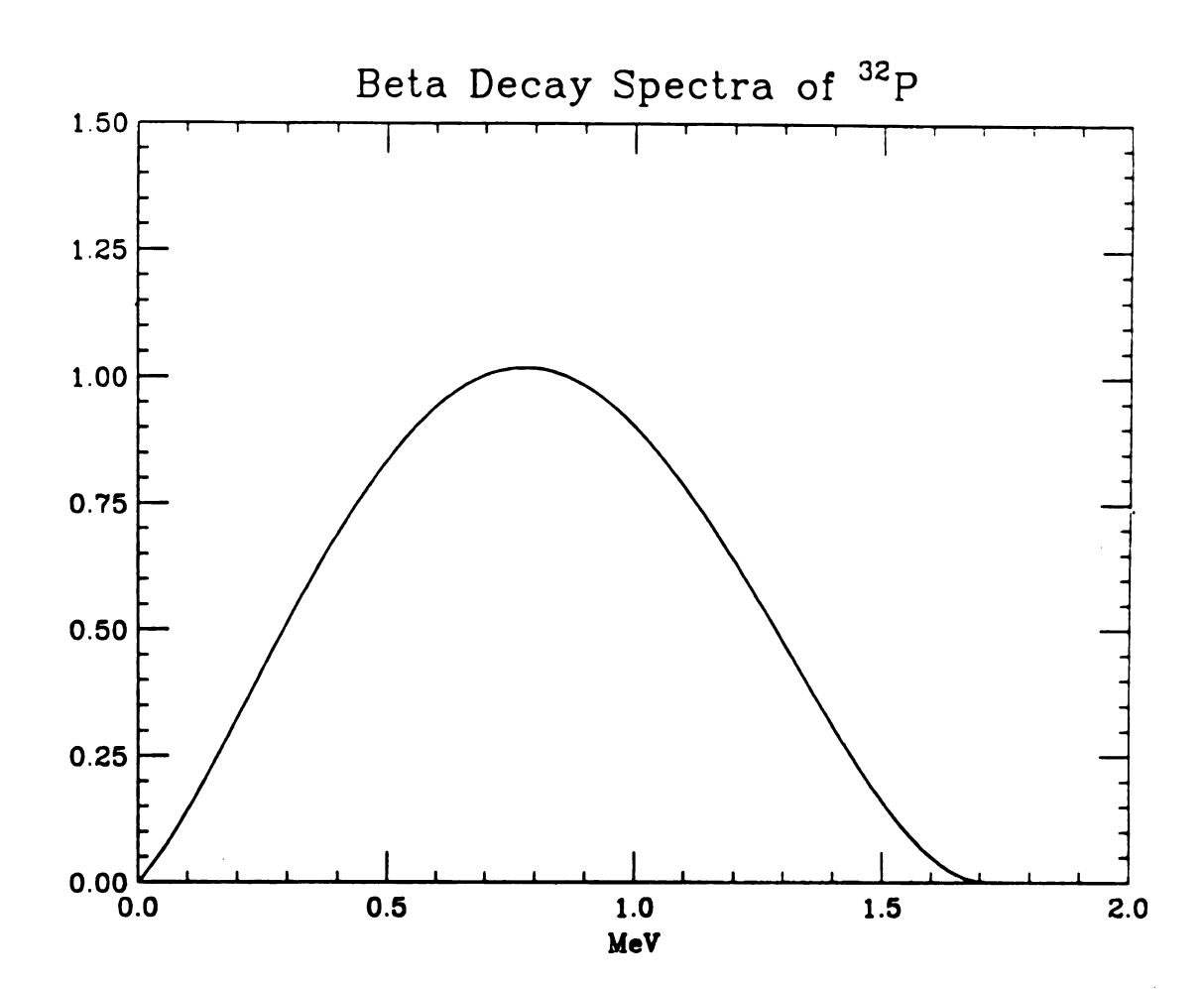


Figure 2.2: Calculated energy spectrum of electrons from the decay of <sup>32</sup>P

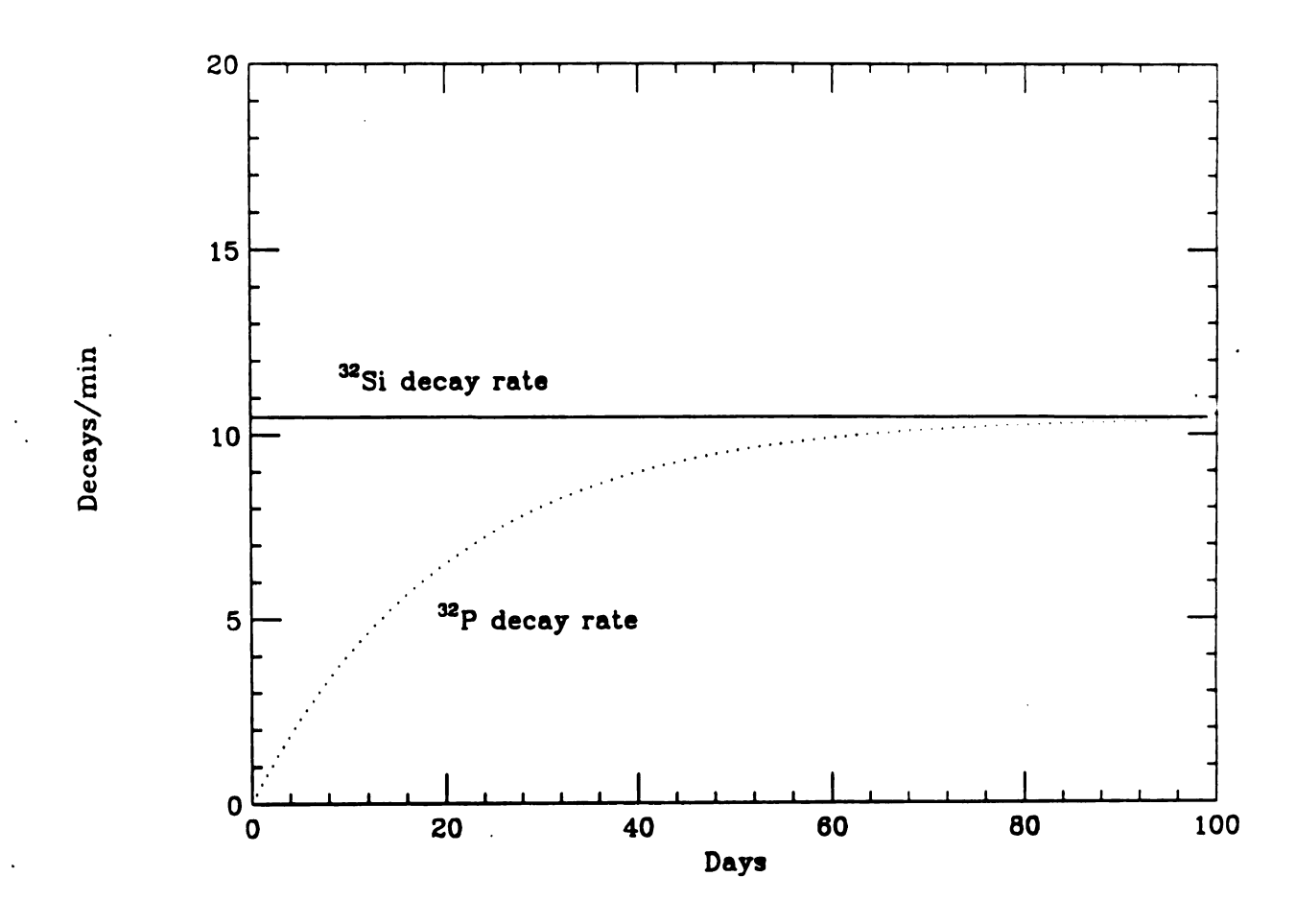


Figure 2.3: The calculated decay rates of  $^{32}$ Si and  $^{32}$ P as functions of time. Assuming the half-life of  $^{32}$ Si is 100 years, initially, there are no  $^{32}$ P nuclei, and there are  $8 \times 10^8$   $^{32}$ Si nuclei at the beginning.

inch in diameter and 0.75 in height, the background with a threshold setting of 200 KeV without any shielding and anti-coincidence arrangement was 5.89/s, with 0.5 inch of Al as shielding, it was reduced to 3.95/s, with 0.375 inch of Cu, it became 3.08/s. The best result was obtained using two photo-tubes in coincidence with a triple shield of 0.5 inch Al, 0.375 inch of Cu, 2.75 inch of Pb and anti-coincidence arrangement was a background level of 0.157/s. A similar measurement was done with smaller scintillator (1.5 cm in diameter, 0.5 cm in height), and the best result obtained was 0.027/s under the same conditions. Other approaches such as using the coincidence of fast and slow components of a piece of scintillator to reduce the background did not improve the measurements. This may be mainly due to the fact that the glass used in the phototube and the Epoxy in the base were all contributors to the background [Kno 89]. With the lowest background level mentioned above, the number of <sup>32</sup>Si nuclei needed to make the activity of <sup>32</sup>Si decay comparable to the level of background would be 108-109. If other fragments were taken into account, the number of nuclei to be implanted into the scintillator would be still larger. As shown in figure 2.4, when such a large number of particles bombard a scintillator, the detector is degraded [Zor 90]. In addition, the phototube was found to lack long term stability, and the detector is hard to calibrate because of its poor resolution. All those are crucial to the half-life measurement.

To overcome the shortcomings of the scintillator mentioned above, we made more background measurements with Si detectors, which, unlike scintillators with phototubes, have good long term stability, but are more expensive. The measurements were done with two detector of 300 mm<sup>2</sup> in area, and with thickness of 500  $\mu$ m. These Si detectors are transmission type detectors, and we will refer to as activity counters. During activity determination, the sample were placed between the two counters. A

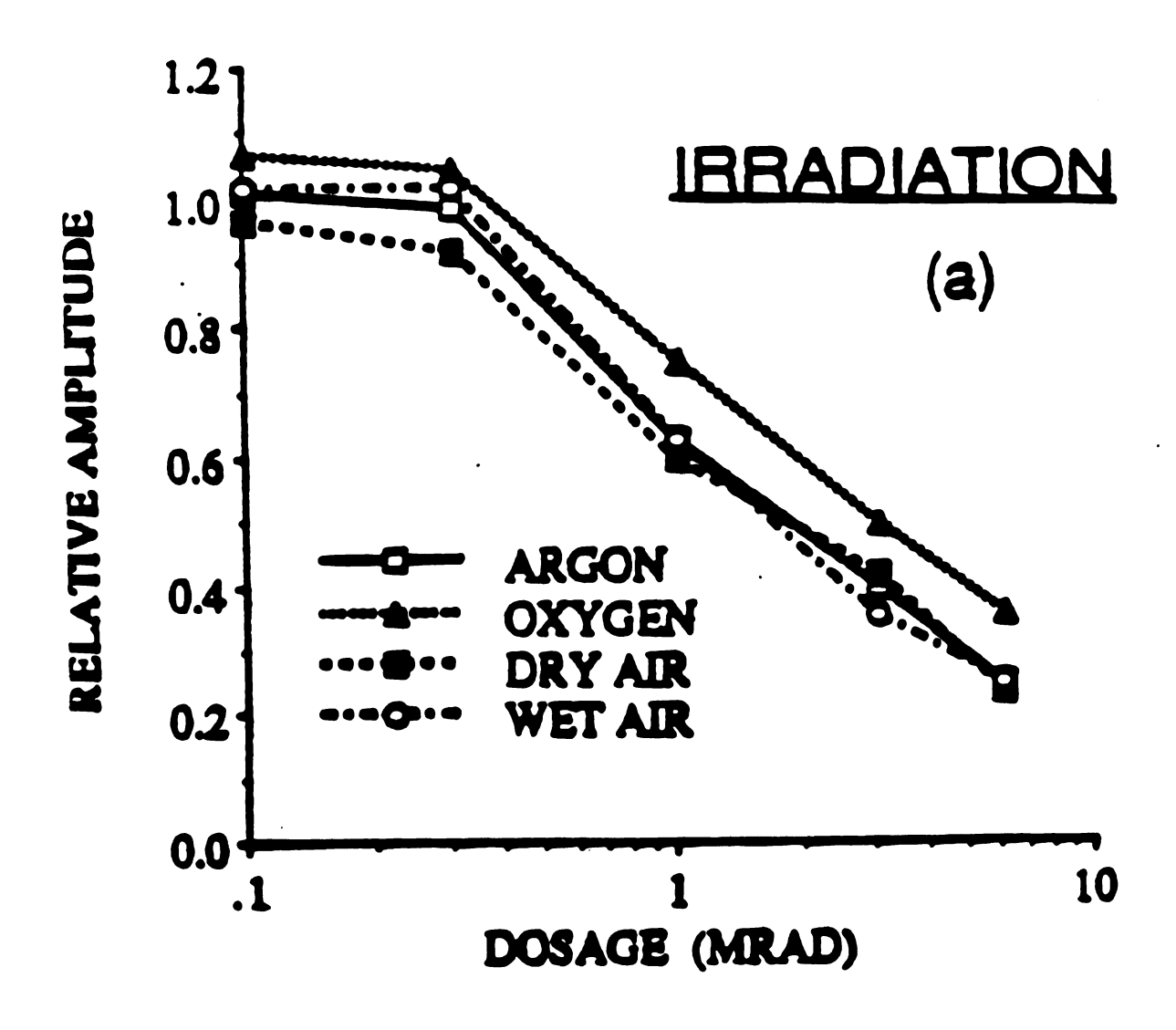


Figure 2.4: Relative scintillator pulse heights for samples of BC408 cylindrical samples (15 mm diameter × 10 mm thickness) irradiated by a <sup>60</sup>Co gamma source (70 Krad/hr in different atmospheres [Zor 90]

Table 2.1: Background rate measured by Si detector (above 200 KeV)

Condition	Unshielded	Shielded
No gate	(0.085±0.004)cnts/s	(0.026±0.002)cnts/s
Anti-muon	$(0.058\pm0.003)$ cnts/s	(0.0094±0.002)cnts/s
coincidence with muons	(0.026±0.002)cnts/s	$(0.0169\pm0.002)$ cnts/s

frame was made to hold the detectors, and new shielding, as shown in figure 2.5, was constructed to reduce the background. The measured backgrounds under different conditions with a threshold setting of 200 KeV are summarized in table 2.1. One can see that the lowest background level obtained was 0.009/s with both shielding and anti-coincidence requirement. The background could be further reduced if we required the coincidence of two Si detectors. This is particularly useful if the number of <sup>32</sup>Si nuclei implanted was less than 10<sup>8</sup>, and a Si detector can be used as implantation media. Activity determination of the implanted detector can then be made by requiring the coincidence of the implanted detector with the activity counters. In this way, the background is reduced but the number of measured true decay events is not. However this approach can't work if the number of <sup>32</sup>Si nuclei implanted is so large that the detector performance is significantly degraded due to the implantation process.

In view of results discussed above, Si detectors were chosen as activity counters. Taking the efficiency of the counting system into account, the number of <sup>32</sup>Si nuclei needed to obtain an activity comparable to the level of background was determined to be 10<sup>8</sup>—10<sup>9</sup>.

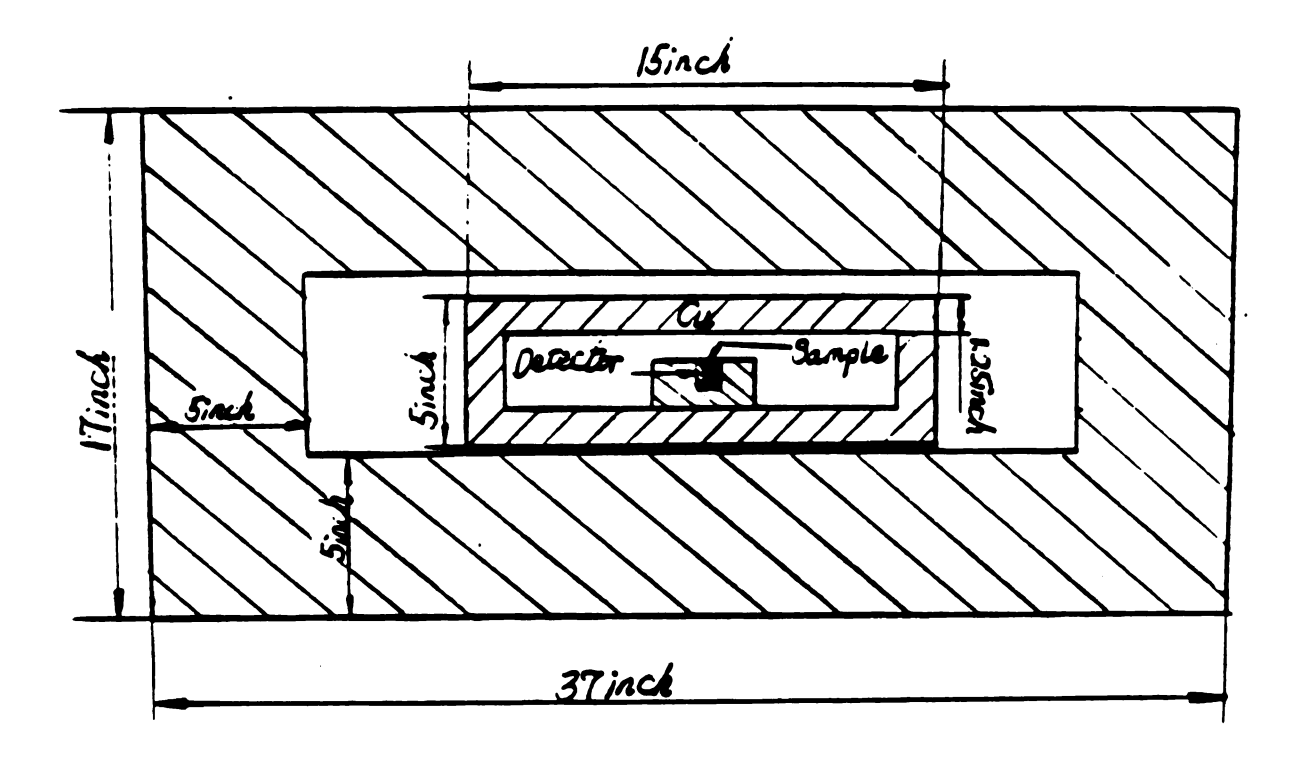


Figure 2.5: Shielding arrangement to reduce the background for the activity counter.

To develop a reliable counting system for the activity determination, a suitable data taking method was needed and the detectors had to be calibrated accurately. To calibrate the detectors, a combination of sources and analog pulsers were used. The two sources used were <sup>57</sup>Co and <sup>133</sup>Ba with the principal transitions at 122 keV for <sup>57</sup>Co and at 81 keV and, 356 keV for <sup>133</sup>Ba. The pulser which was calibrated with those two sources, was used to get calibration points for the detector at higher energy and to check the stability of the detectors periodically. The electronics of the counting system is shown in figure 2.6. The signal from each detector is sent to a preamplifier, and then to an amplifier. The slow output of the amplifier was sent to an analog to digital converter (ADC) and recorded by computer. The fast output was used to generate logical signals to trigger the computer for data taking. With each trigger, the time and energy of the event were recorded and written on disk. This way, the energy and time spectra of every event can be generated later during data analysis, and various conditions such as threshold, coincidence can be imposed in software. In figure 2.7, energy spectra from a typical background measurements are obtained with each of activity counters is shown. In figure 2.8, time spectra corresponding to those same background events are shown. One can see in figure 2.8 that the background remains unchanged during measurement.

#### II A1200

The A1200 beam analysis device[She 89] connects the K1200 cyclotron with the experimental vaults. It can be used either as a beam transport device or as a fragment separator. Used for the latter purpose, it can separate projectile fragments from K1200 beams and deliver them to different experimental devices or it can be operated as single mass spectrometer to study these fragments. As shown in figure 2.9,

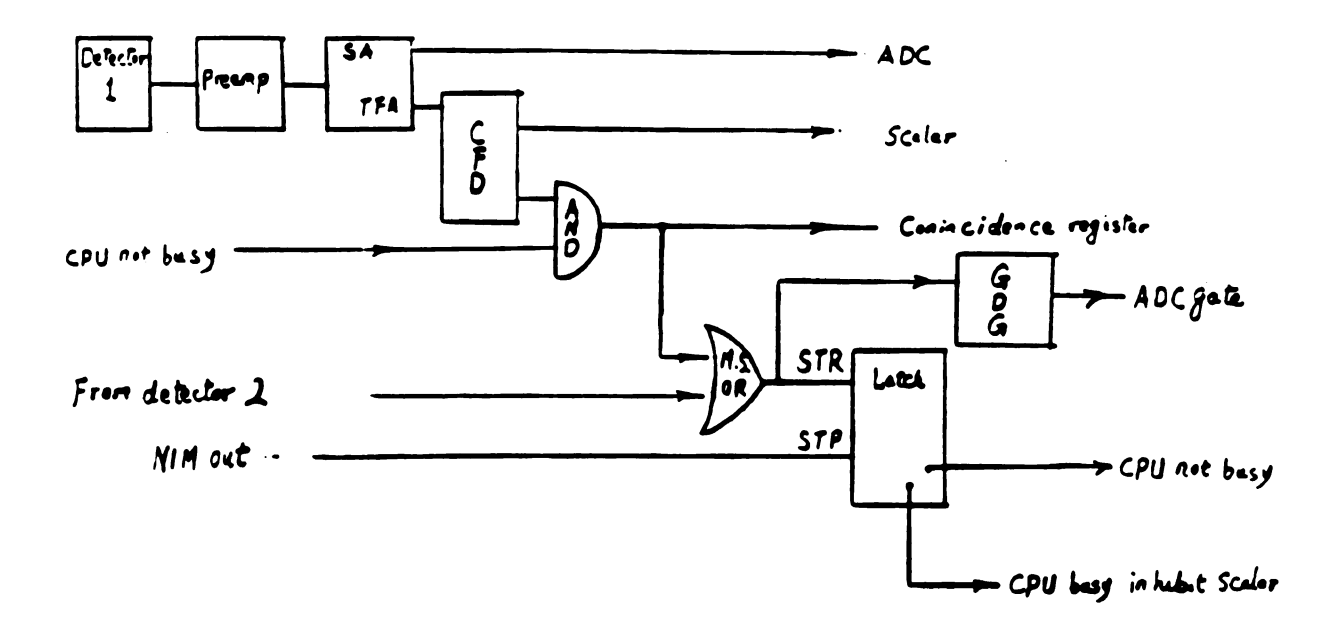


Figure 2.6: Schematic setup of electronic modules for activity determination

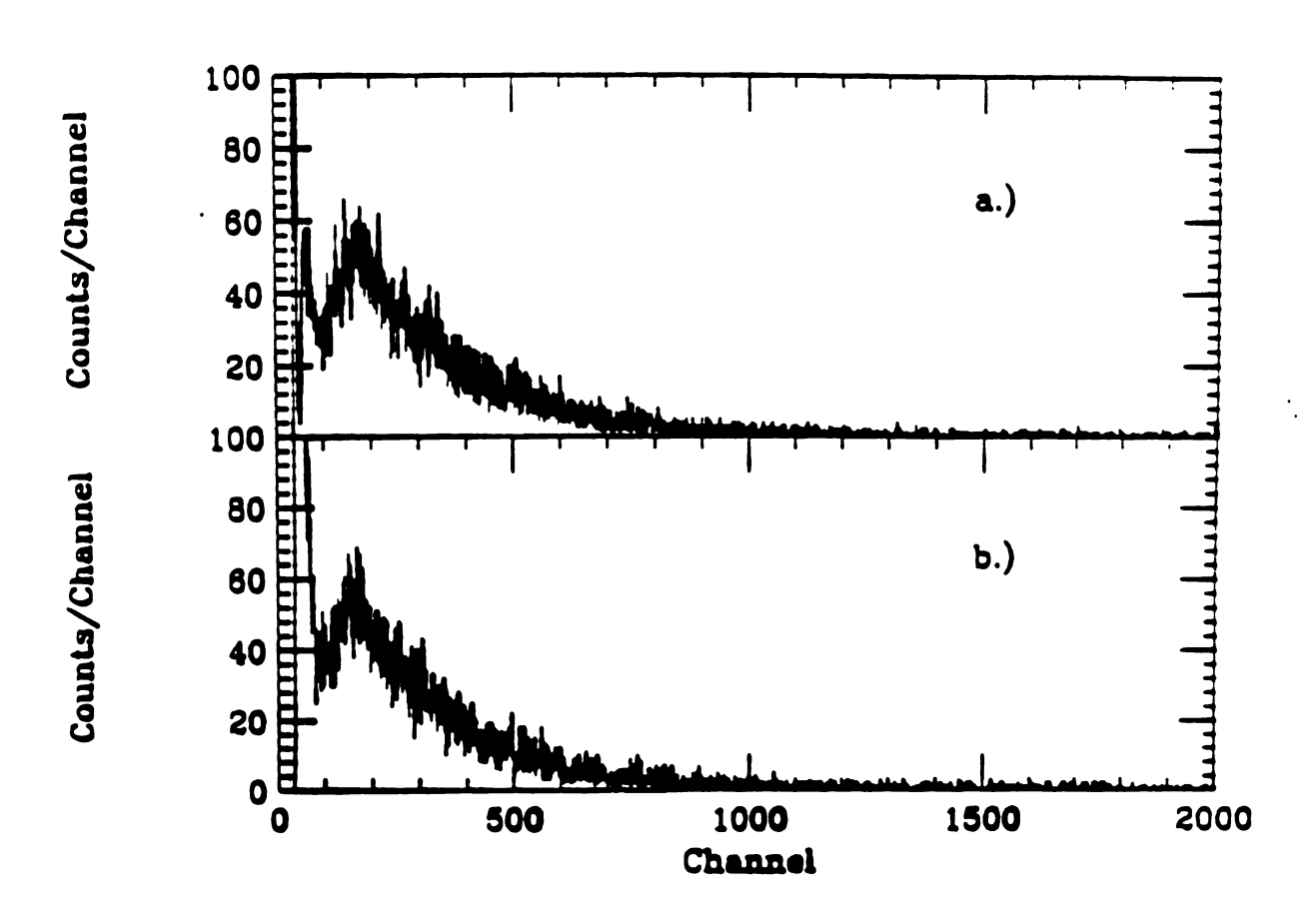


Figure 2.7: Background energy spectra taken by the two activity counters,[a.) is taken by detector 1, b.) taken by detector 2.]

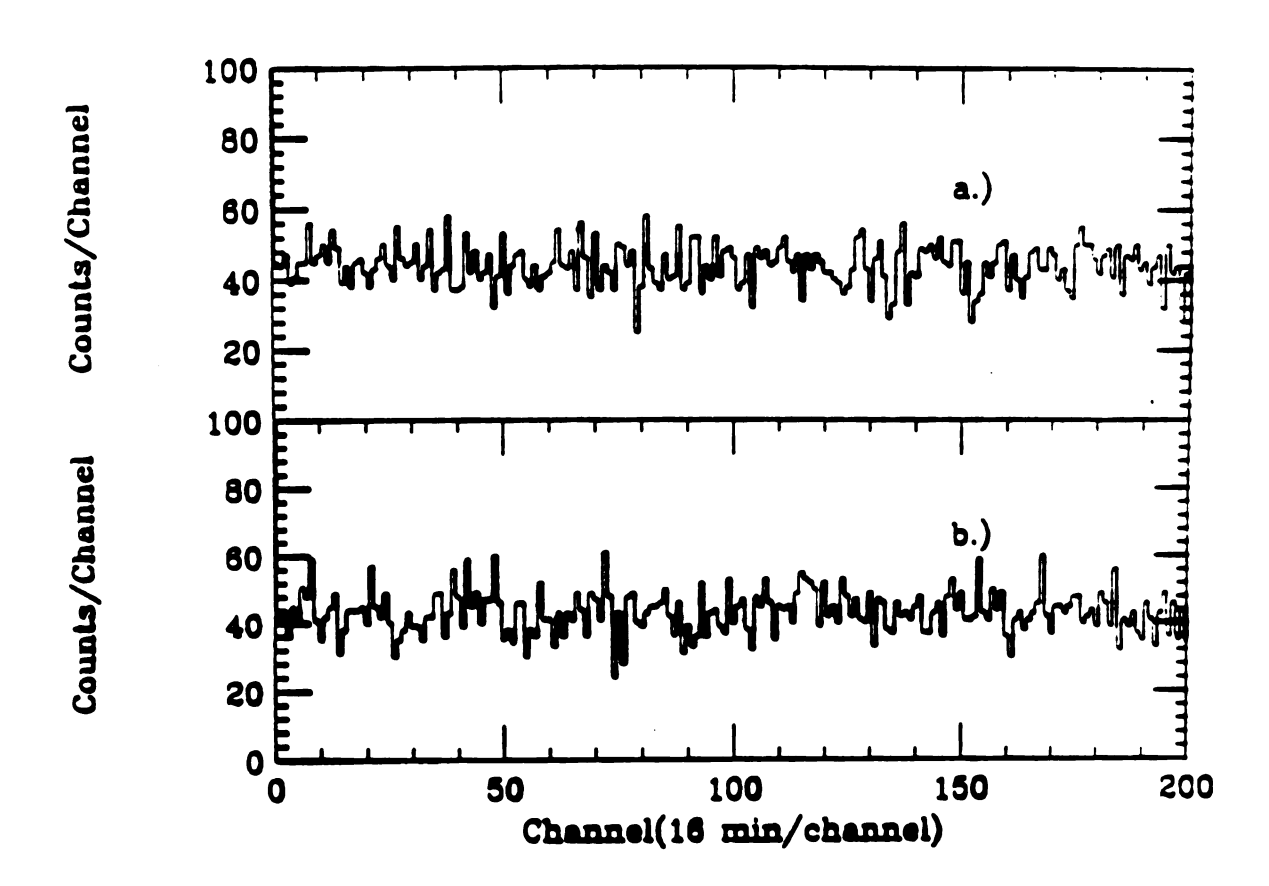


Figure 2.8: Background time spectra taken by the two activity counters, [a.) is taken by detector 1, b.) is taken by detector 2]

the A1200 consists of a large number of superconducting magnets [Zel 85], i.e., four 22.5° dipole bending magnets, four quadrupole doublets and two quadrupole triplets. There are also four room temperature sextupole magnets for aberration corrections. The A1200 has two basic modes of operation: a dispersive mode and an achromatic mode. In the dispersive mode, primarily for accurate cyclotron beam analysis purposes, the dispersions of the two dipole pairs add to give a maximal dispersion an resolving power, with a small acceptance. In the achromatic mode, mainly used for separation of secondary radioactive beams, the dispersions are canceled to provide a final achromatic focus at the end of the device, while creating two intermediate dispersive images (image #1 and image #2 in figure 2.9) between the two pairs of dipoles.

In addition, in the achromatic mode, two different acceptance modes are possible: a medium acceptance mode, if the target is placed at the beginning of the A1200, and a high acceptance mode, if the target is placed near the entrance to the first quadrupole triplet. The characteristics of those A1200 operation modes are summarized in Table 2.2 (taken from [She 89]).

To operate the A1200, the magnets of the A1200 can be conveniently set to a desired  $B\rho$  value with the computer program "Boss" [Mor 91]. For a given magnetic rigidity value the code calculates the currents for the magnets and sends the values to the power supplies. For greater accuracy in rigidity measurements, the fields of the dipole magnets are measured by NMR magnetometers. To stop the primary beam whose rigidity can differ from that of the fragment of interest, anodized aluminum bars are placed in the first pair of the dipoles, along with movable blockers at the exits of these dipoles. Those bars and blockers can be connected in series to a current integrator.

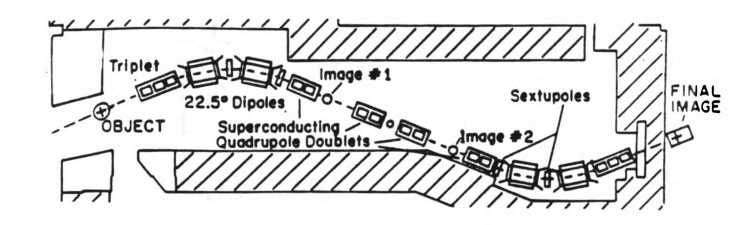


Figure 2.9: A schematic drawing of the A1200 analyser

Table 2.2: Characteristics of the operation modes of the A1200 [She 89]

Parameter	Operation Mode		
	High Res.	Medium Acc.	High Acc.
Ωmsr	0.25	0.8	4.3
$\Delta \theta[mr]$	10	20	54
$\Delta \phi [\mathbf{m} \mathbf{r}]$	10	40	80
$\Delta P/P[\%]$	0.4	3.0	3.0
$B\rho[T-m]$	5.4	7.2	5.4
Resolution	10000‡	3300	1300
(x/x) Int. Image Focal Plane	3.0 1.0	0.47 0.99	1.24 1.0
(x/δ)[cm/%] Int. Image Focal Plane	15.0 10.0	1.67 0.0	1.30 0.0

†1mm beam spot on the production target.

tat the final image, with half the resolution at the center image.

The principle of operation of the A1200 mass separator is as follows. A charged particle moving in a magnetic field is subjected to the electromagnetic interaction called Lorentz force. At every point, the force is perpendicular to the velocity of the particle and the magnetic field. Therefore, it acts as the centripetal force on the moving particle if no other interaction is present. This relation can be written down as follows

$$q\vec{v} \times \vec{B} = \vec{F} = -m \frac{v^2}{\rho^2} \vec{\rho}$$

where q is the charge of the particle,  $\vec{v}$  the velocity of the particle, m the mass of the charge particle,  $\vec{B}$  the magnetic field,  $\rho$  the radius of curvature of the trajectory of the charged particle. In a special case, when  $\vec{B}$  is perpendicular to  $\vec{v}$ , the above relation can be simplified as follows.

$$B\rho = \frac{m}{q}v = \frac{p}{q}$$

Here  $B\rho$  is the "magnetic rigidity" mentioned above, and it is equal to p/q, where p is the momentum of the particle. Since in a projectile fragmentation reaction, the velocity of the fragments are nearly the same as the velocity of the beam, and since at our energies the ions are fully stripped of their orbital electrons, the above formula shows that the dipoles of the A1200 select the fragments according to their A/Z values. The energies of the selected particles are thus proportional to  $\frac{Z^2}{A}$ . However, with this selection alone, the variety of the nuclides collected is still very large. Therefore, an intermediate degrader is placed at image #1 to make the selection of the particles more exclusive. The effect of the degrader is to slow the particles down due to the spe-

cific ionization process which is given by the Bethe's formula approximately as follows.

$$\frac{dE}{dx} \propto \frac{AZ^2}{E}$$

where E is the energy of the particle,  $\frac{dE}{dx}$  is the specific ionization of the particle, A and Z are the same as above. The above energy loss formula can be further transformed as follows.

$$\frac{1}{E}\frac{dE}{dx} \propto \frac{AZ^2}{(Z^2/A)^2} = \frac{A^3}{Z^2}$$

which means that after the first half of the A1200, the particles lose a fraction of their energy(in the degrader) proportional to their corresponding  $\frac{A^3}{Z^2}$  values. This makes the second half of the A1200 more selective of the isotopes. The degrader can be either achromatic or mono-energetic: An achromatic degrader, often a curve shaped foil resulting in a wedge-like absorber, is made in such a way so that the relative momentum spread of the ions is not changed by the degrader. On the other hand, a mono-energetic degrader is made to reduce the energy spread of the ions of each isotope so that after the degrader, the energies of the particles of each isotope are all about the same.

When the A1200 is used as a "stand alone" spectrometer, the reaction products are focused at the end of the device, the "focal plane" of the A1200. At the focal plane, a detector array consisting of two X-Y position sensitive parallel-plate avalanche counters (PPACs) and a totally depleted ion-implanted silicon detector (Called "PIN-diode" or the  $\Delta E$  detector) 325  $\mu$ m thick with an active area of 25 cm<sup>2</sup> are located. The two PPACs upstream of the  $\Delta E$  detector, are separated by about 60 cm and are

used to monitor the focusing of the particles: the first PPAC (called PPAC 2) determines the position of the particles at the focal plane and, combined with the second one (called PPAC 3), the angle with respect to the axis of the device. An upstream PPAC (called PPAC 1) is positioned at the second intermediate image (image #2) of the A1200. At this dispersive image, the horizontal position of the particles changes linearly with respect to their rigidity, and thus the momentum of the particles can be calculated from the measured position when the A1200 is used for measurements of the momentum distribution of the fragments. The position signals from the PPACs are obtained by charge division of an electron avalanche collected on a series of anode strips, the strips are connected in series with a resistor between each strips[Swa 91]. Each detector has two sets of anode strips, one horizontal and the other vertical, thus providing both the X and Y position information. The principle of the resistive charge division is illustrated in figure 2.10. The PPACs operate with isobutane gas at a pressure of 5 torr and at an anode voltage of about 600 Volts. The position resolution (FWHM) of these detectors is typically about 1 mm.

The start signal of the time-of-flight (TOF) of the particles is the fast output from the  $\Delta E$  detector, and stop signal is obtained from the radio frequency signal (RF) from the cyclotron. The combination of the TOF measurement and of the  $\Delta E$  measurement from the PIN-diode provides unambiguous particle identification.

In figure 2.11, a schematic diagram of the electronics modules used in the standard A1200 experiment is shown. It can be briefly described as follows. The four position signals (Left, Right, Top, Bottom) obtained from each of the three PPACs are read by ADC's. The TOF relative to the cyclotron RF is measured with a TAC. The  $\Delta E$  detector signal is sent to an ADC, and its fast timing output is used to generate the

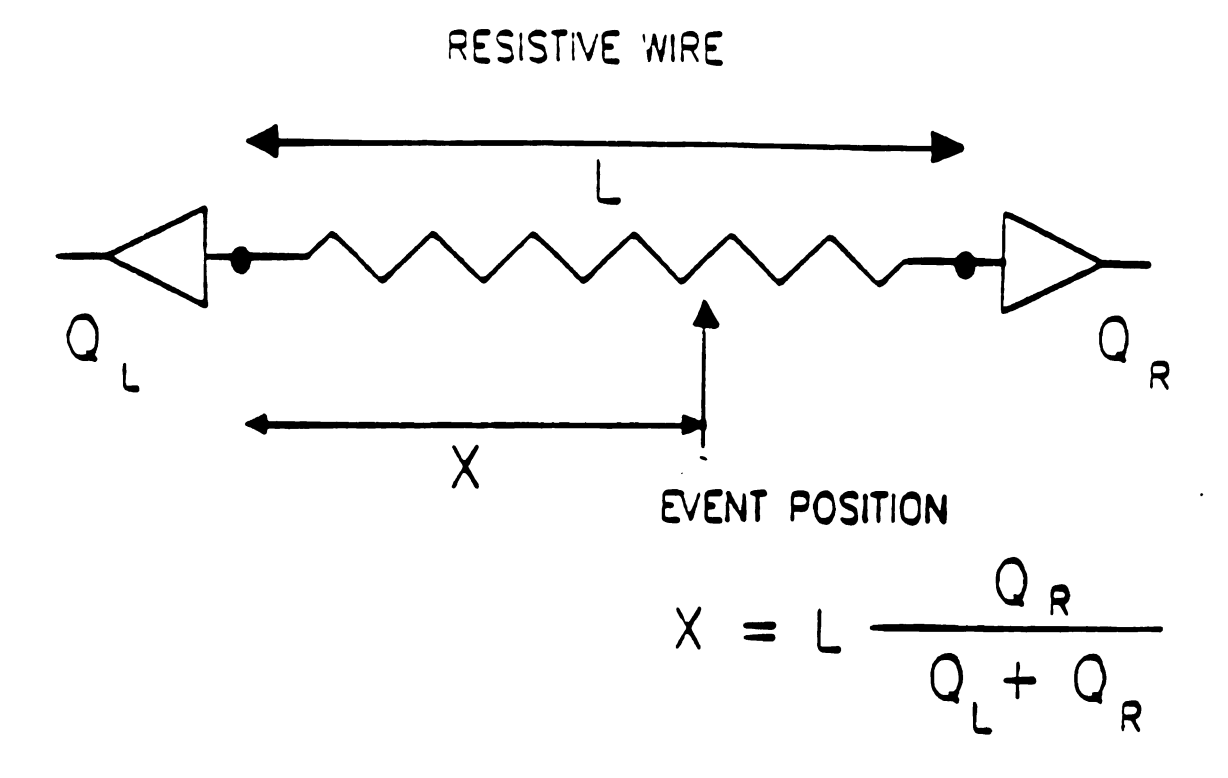


Figure 2.10: The principle of resistive charge division for position measurements. The charge of an electron avalanche, created by a fast charge particle entering the gas volume of the detector, is collected by a series of anode strips which are connected in series with resistors. the charge is split into two fractions, which propagate towards the two ends of the resistor series. The ratio of the signals at the ends of the resistor series is directly related to position

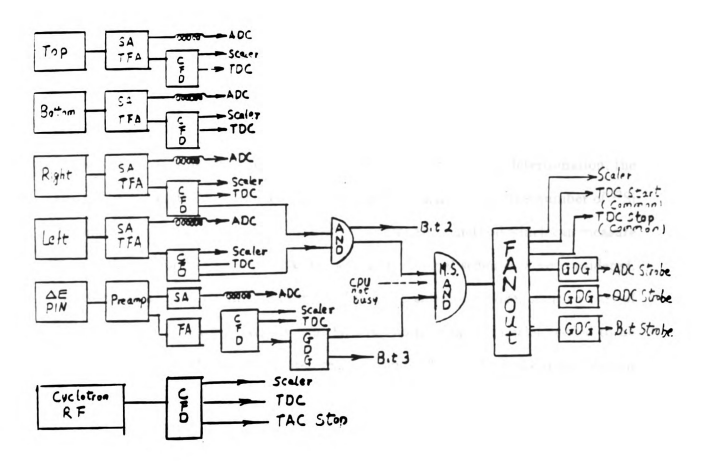


Figure 2.11: Schematic diagram of the standard electronic setup for experiments using the A1200. Where ADC: analog-to-digital converter, CFD: constant fraction discriminator, FA: Fast amplifier, GDG: gate and delay generator, QDC: Charge-to-digital converter, TAC: time-to-analog converter, TFA: timing filter amplifier,

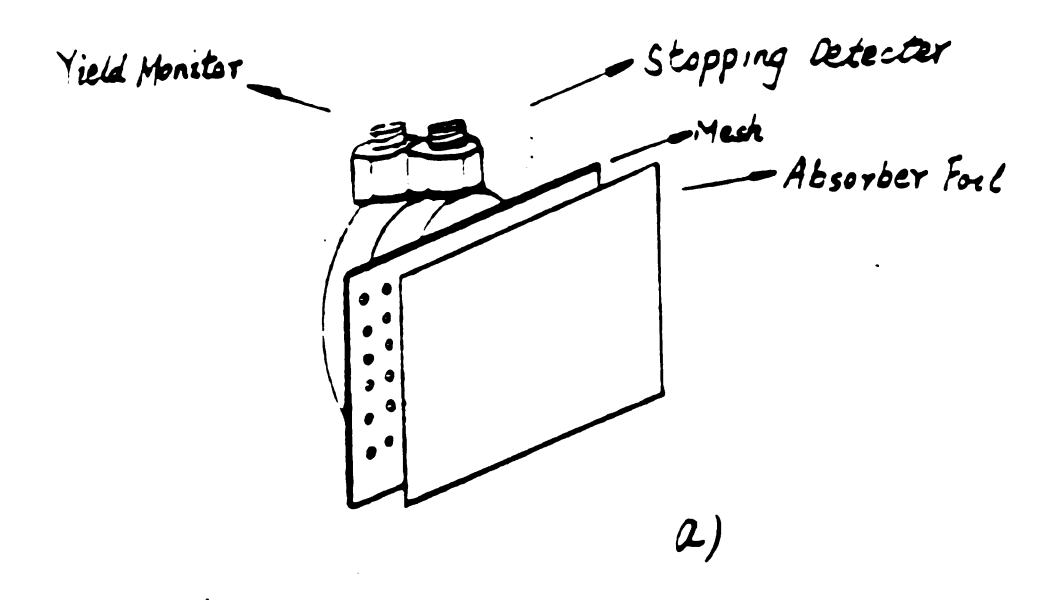
event trigger(Master Gate). TDC(time to digital converter) signals are recorded for all the PPACs, the ΔE detector and the RF timing relative to the master gate. The standard NSCL aquisition system is used to read the electronic modules and write data to tape[Fox 89].

## III The devices for implantation

As mentioned in previous sections, the number of implanted 32Si nuclei needed is large. A detector can be easily damaged in the process of the implantation. We therefore can't use the standard A1200 detectors to measure the number of <sup>32</sup>Si nuclei implanted. Also, since we chose to use Si detector to do activity determination, the size of the implantation spot has to be limited. In addition, since the number of <sup>32</sup>Si nuclei implanted is crucial to the half-life measurements, a method which can measure the number of nuclei implanted has to be found. Several schemes were considered, for example, a small scintillator in front of the implantation device, or using part of the focal plane detector array. Due to the large number of <sup>32</sup>Si nuclei needed to be implanted, those methods are limited by the count rate at which the detectors can operate properly. The method we adopted at first was reduce the number of nuclei that can reach the detector. This was realized using a combination of detectors, Al foils and an Al mesh. The aluminum mesh is made of an aluminum plate of 1.02 mm in thickness with holes of 0.0135 inch in diameter uniformly distributed with 1 mm distance between center of adjacent holes. In figure 2.12, the arrangement is shown. An Al collimator frame hold Si detector, Al foils, and the mesh and limits the implantation spot size. As shown in the figure, they are arranged in the order of mesh, Al foils, and Si detectors. The thickness of the mesh was calculated to allow 32Si nuclei to pass through and be stopped in the middle of the Al foil (or detector) behind it. The particles that pass though the holes of the mesh will have

enough energy to reach the Si detector at the very back and be detected. The mesh limits the number of particles that can reach the Si detector at the back to about one tenth of the total particles and therefore allows the detector to function when the rate of incoming particles is high. Since the transmission coefficient of the mesh can be measured by replacing the Al foil with a Si detector of equivalent thickness, the number of <sup>32</sup>Si nuclei can therefore be monitored during the experiment. The mesh, foil and detectors are described in the next chapter.

With above arrangement to monitor the number of implanted  $^{32}$ Si nuclei, the standard detectors of the A1200 can be turned off during the implantation, and the Si detector takes the place of the PIN-diode  $\Delta E$  detector to provide event trigger, timing signal and energy loss information. The electronics is not be changed from that of figure 2.11, only the  $\Delta E$  signal from the PIN-diode detector is replaced by the signal from the Si detector at the back of the stack.



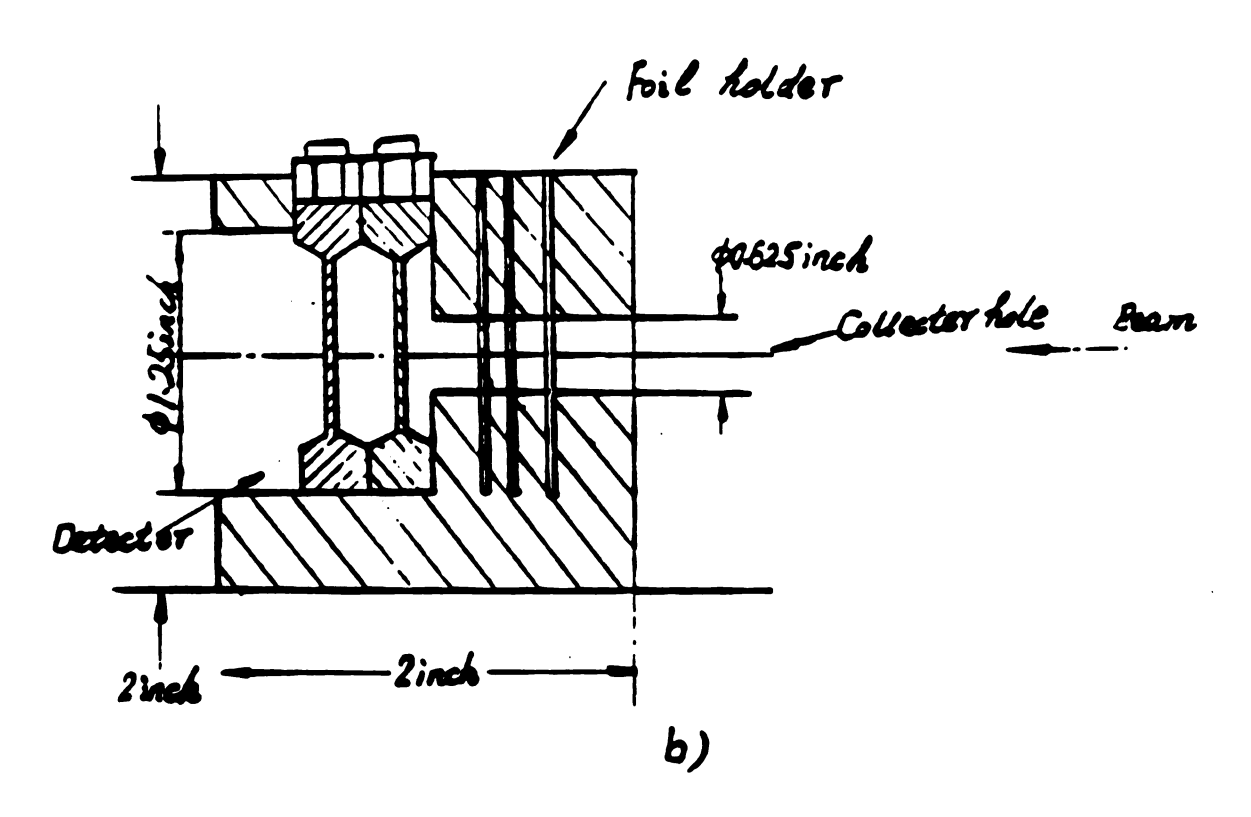


Figure 2.12: a.) Schematic arrangement of the absorber foil, mesh and detectors b.) Schematic drawing of the collimator frame used to hold mesh, Al foil and Si detector during implementation

# Chapter 3

## Experimental Setup

### I The Implantation

#### 1. Introduction

In order to obtain a sample with 10<sup>8</sup>-10<sup>9</sup> nuclei of <sup>32</sup>Si, we used the projectile fragmentation reaction of <sup>40</sup>Ar on Be. The beam energy was 65 MeV/A, optimized for <sup>32</sup>Si yield by taking into account both the energy dependence of the production cross section and the available beam intensities from the K1200 cyclotron at different energies. The target thickness was 235 mg/cm<sup>2</sup>. It was chosen by considering the energy broadening due to scattering in the target and the angular acceptance of A1200 to maximize the <sup>32</sup>Si yield. Both of the above calculations were done with two programs, one Intensity [Win 91], the second, developed by Daniel Bazin originally for LISE [Baz 91]. The results from both programs agree with each other. The magnetic rigidity results obtained in the calculations were used during the experiment as initial setting in finding <sup>32</sup>Si.

The A1200 analyser at NSCL was used as an isotope separator to reduce the number of unwanted isotopes. The selectivity was enhanced by placing a 150 mg/cm<sup>2</sup> Al

wedge a achromatic degrader (as described in chapter 2) at the image 1 position of A1200. The field settings were calculated and later fine tuned on line to maximize the collection of <sup>32</sup>Si nuclei.

### 2. Implantation Experiment I

There were two implantation experiment with different configurations. The first experiment was carried out from April 26th to April 30th in 1991. A 123 mg/cm<sup>2</sup> Al foil was used as the catcher foil into which the nuclei of <sup>32</sup>Si were to be implanted. At the beginning of the run, we used the A1200 focal plane detector described in chapter 2 to identify the particles and to find an optimal setting of fields and focusing. Afterwards the stack of absorbers, Si detectors, and catcher foil was put in position so that the implantation could begin.

The stack mentioned above is shown in figure 2.12. It consisted of a collimator with a hole of 0.75 cm in radius facing the beam, an Al plate 0.102 cm thick with holes of 0.0135 inch in diameter uniformly distributed with 1 mm distance between center of adjacent holes, and following this 'mesh', an Al absorber with a thickness of  $40 \text{ mg/cm}^2$ . Behind the absorber, the third element could be either a Si detector or an Al foil for the purpose of implantation (we called it stopping detector, or stopping foil although some particles get through). The last element in the stack was a  $200 \mu \text{m}$  Si detector to be used as 'monitor', since it 'monitored' the number of  $^{32}$ Si implanted by detecting those particles that passed through the holes of the mesh. The thickness of the  $40 \text{ mg/cm}^2$  absorber was calculated so that the  $^{32}$ Si particles that do not pass through the holes of the mesh would be stopped in the middle of following element. In the beginning of the implantation, a thick  $500 \mu \text{m}$  Si detector was used as the

third element of the stack (after the mesh and Al absorber) so that with a low beam intensity, the transmission rate of the mesh could be obtained by measuring the ratio of counts of the group of <sup>32</sup>Si particles which would reach the monitor detector to the counts of those which would be implanted (those particles which did not pass through the hole of the mesh).

To set up the A1200 properly during the experiment, a fully stripped beam of  $^{40}Ar^{+18}$  was sent through the A1200 to the focal plane. Since the beam energy is well defined and the beam intensity is large enough to view on scintillators at various positions of the beamline, it simplifies the setup of A1200 to a great extent. Once the fields of dipoles and focusing magnets were set and optimized for the beam, any further changes in the A1200 setting can be scaled from this setting by a combinations of software and hardware developed here [Mor 91]. Detector calibrations were also carried out at this stage of the experiment and these used later for particle identification. In figure 3.1, the energy loss signal of the beam in a 325  $\mu$ m Si detector (the PIN diode described in Chapter 2) were plotted against the time-of-flight signal of the beam. The time-of-flight start signal was the fast timing signal from the PIN diode detector and the stop signal was a timing pulse from the RF of the cyclotron. Since the beam energy was well defined, the energy loss of the beam can be calculated, and served as an energy calibration of the PIN diode detector. The time of flight of the beam can also be calculated, and as a result, it served to calibrate the time-of-flight signal.

Once the A1200 was setup and detector calibrations were finished, we began to search for  $^{32}$ Si by setting the B $\rho$  value of the A1200 to the calculated optimal value from program calculations. The focusing was checked by the two position detectors at

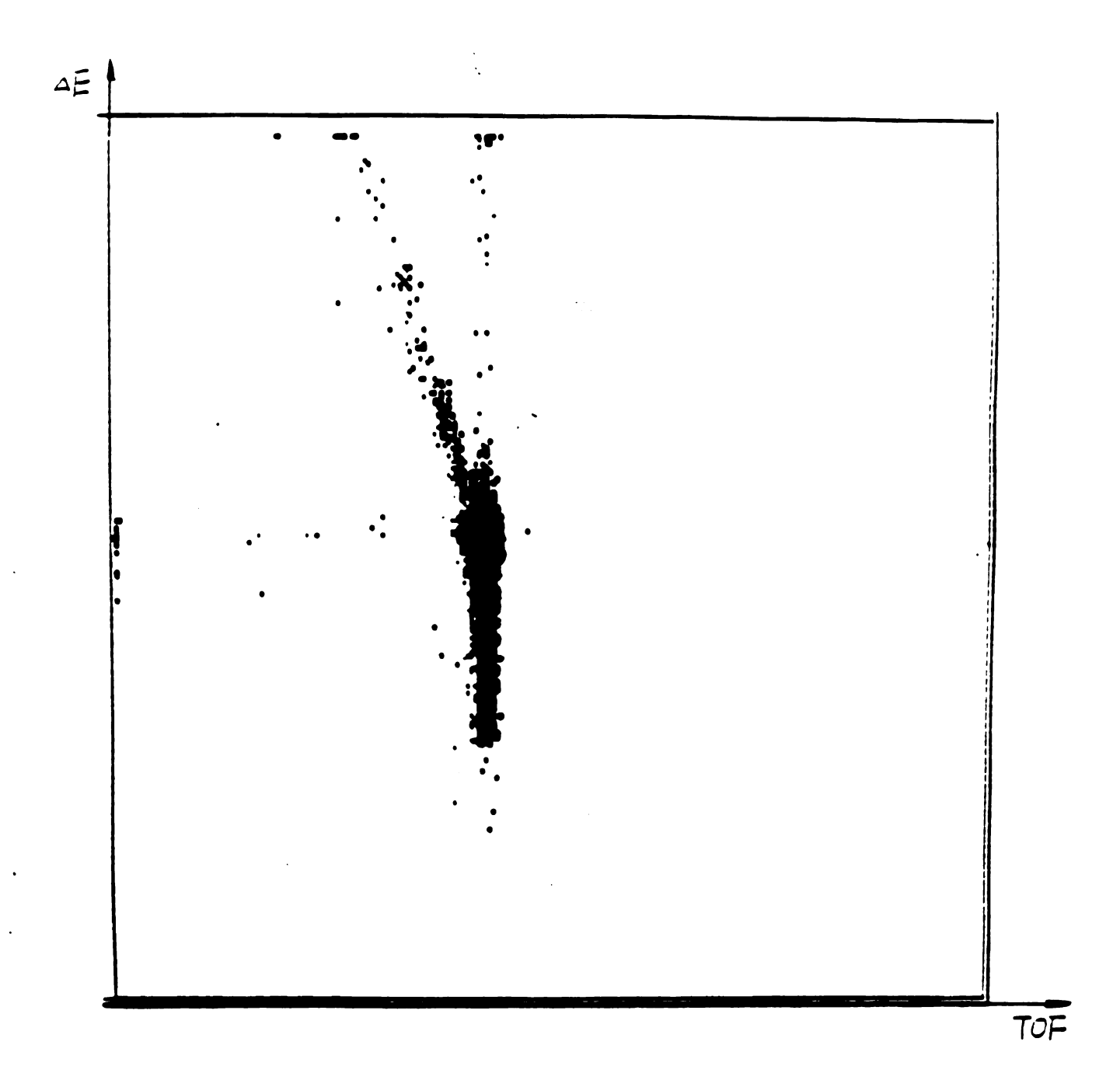


Figure 3.1: Calibration of the PIN diode with the beam, the vertical axis is the energy loss signal of the beam from the PIN diode detector, horizontal axis is the time-of-flight signal

the focal plane (PPAC2 and PPAC3). Since the  $B\rho$  settings of the A1200 were known. the energies and time-of-flights of various particles were also known, and the energy losses of those particles could also be easily calculated. From those calculation and the calibrations obtained in the previous stage, particle identifications could be done by using the two-dimensional histogram of energy loss v.s. time-of-flight as shown in figure 3.2. Once the particles were identified, we proceeded to find the optimal  $B\rho$  setting for <sup>32</sup>Si by scanning the dipole field setting of the A1200 as follows. The dipole fields were changed by a small percentage in one direction. The collection rate of <sup>32</sup>Si nuclei at the new setting was compared with that of the original setting, and if the rate was decreased, we then changed the field settings in the other direction, otherwise we continued the scan until a clear peak of collection rate was seen within the range of the field settings scanned. In figure 3.3. the production rate of <sup>32</sup>Si is plotted against the dipole fields, and a peak can be clearly seen. Unfortunately, this peak setting was very close to a charge state of the beam(+17Ar). And due to the limit of the rate at which the monitor could count, we were forced to move away from this peak by about 2 %. The maximum rate of <sup>32</sup>Si ions at a beam intensity of 40-50 ena was about 6000-8000/sec.

From Figure 3.2., one could see that the number of contaminants (fragments other than <sup>32</sup>Si) were not small which would hurt the experiment in the following ways.

- Due to the limited rate at which the monitor detector can count, one has to reduce the beam for the system to work which in turn reduce the number of <sup>32</sup>Si nuclei that could be implanted.
- Some of the particles may have a relatively long half-lives and therefore complicate the counting later.

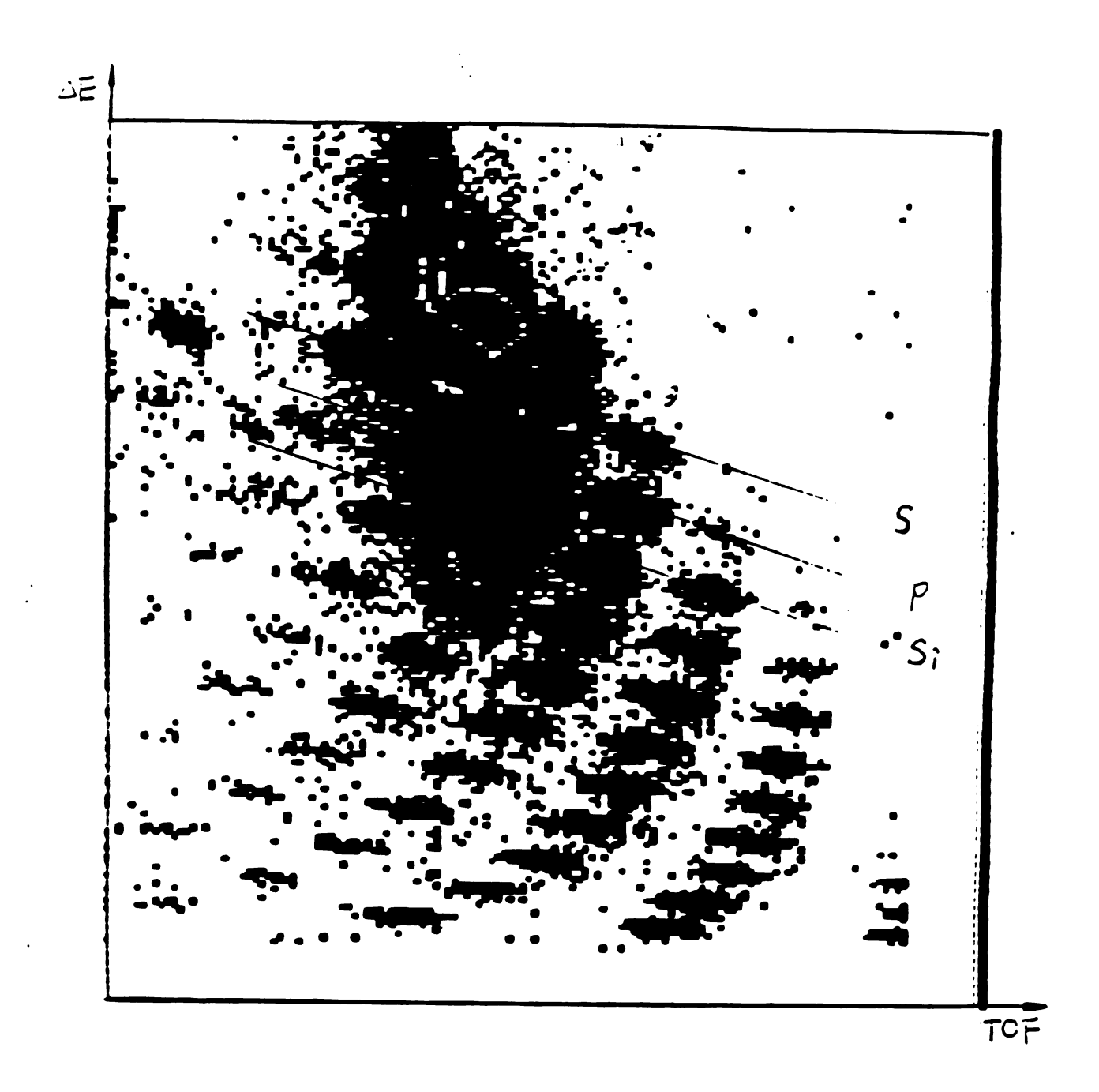


Figure 3.2: Particle identification histogram. Vertical axis is energy loss of the particles in the PIN diode detector, horizontal axis is time-of-flight.

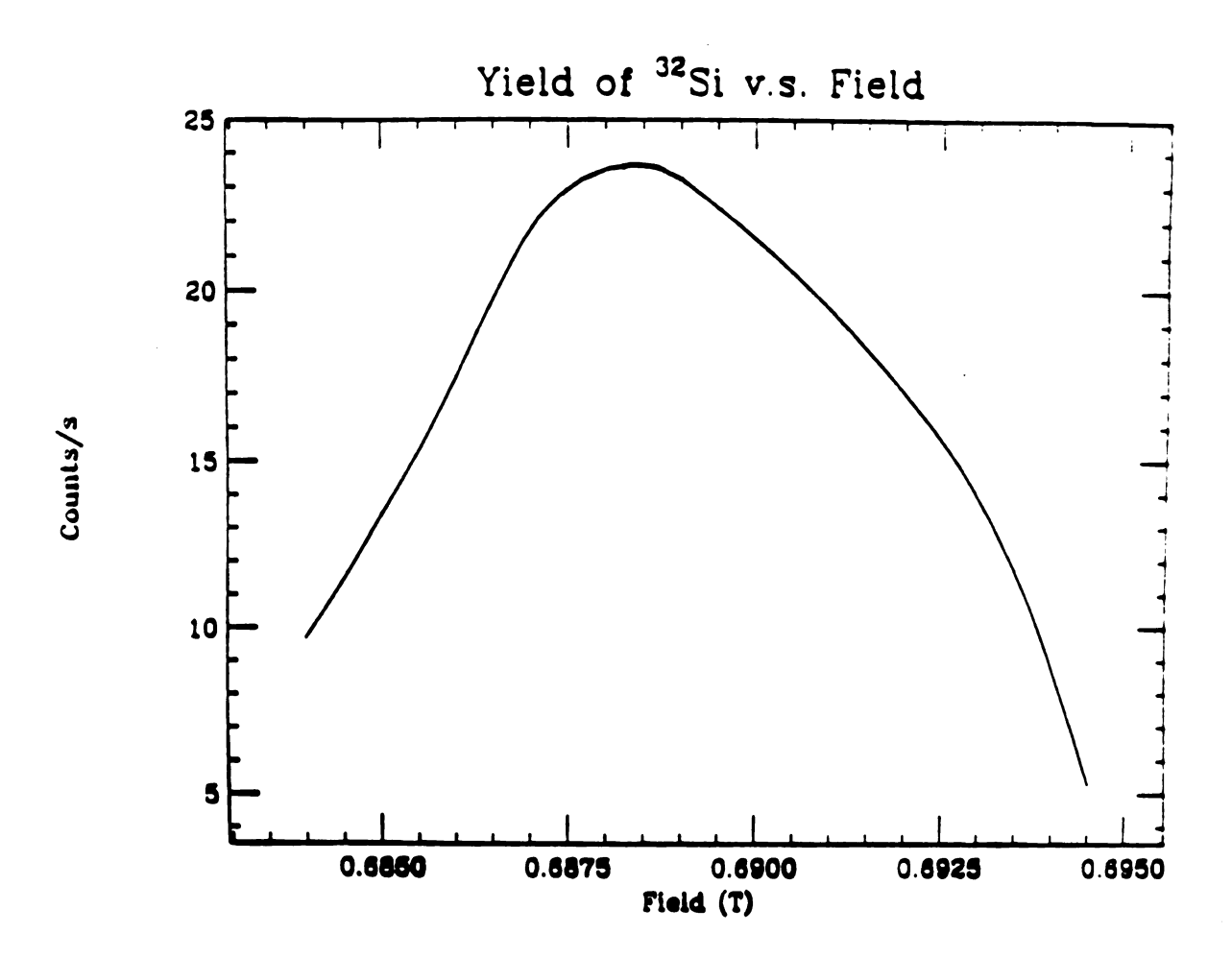


Figure 3.3: The collection rate of <sup>32</sup>Si nuclei as a function of the dipole field.

• Radioactive activation may be a problem if the number of particles that were implanted is very large.

Therefore, to reduce the number of contaminants, a 150 mg/cm<sup>2</sup> Al achromatic degrader was added at the intermediate focal plane of the A1200. The magnetic fields of the second half of the A1200 had to be decreased correspondingly so that the  $^{32}$ Si nuclei after the degrader would still be focused at the focal plane. In figure 3.4, a two dimensional histogram of particle energy loss signal vs. the time-of-flight signal of the particles obtained with the degrader shows that the number of particles is greatly reduced. As explained in chapter 2, this is due to the differences in stopping power of different nuclei. In this case, since we already had the energy calibration of the PIN diode,  $^{32}$ Si could be identified easily by calculating its energy loss in the PIN diode detector with the new B $\rho$  settings for the second half of the spectrometer. The focusing of  $^{32}$ Si nuclei was then adjusted to be optimal so that the number of  $^{32}$ Si nuclei which could get through the collimator of the implantation stack was maximized. In figure 3.5, the 2-dimensional position spectrum of the  $^{32}$ Si nuclei is shown. It was obtained by the two A1200 focal plane detectors PPAC2, and PPAC3.

The implantation stack then replaced the PIN diode Si detector. Initially, the bias voltages of both the monitor detector and the stopping detector were turned on, with the beam intensity low enough ( $\ll 1$  na) so that the count rate in the stopping detector did not exceed the limit at which the detector was able to work properly. As shown in figure 3.6  $^{32}$ Si could be identified. The transmission efficiency of the mesh was calibrated at this stage, and figure 3.7 shows the response of the 500  $\mu$ m Si detector. An estimated value of about 11 % was obtained for the fraction of transmission, and this efficiency together with the number of  $^{32}$ Si measured by the monitor would give us a good estimate of how many  $^{32}$ Si nuclei had been implanted. The implantation was

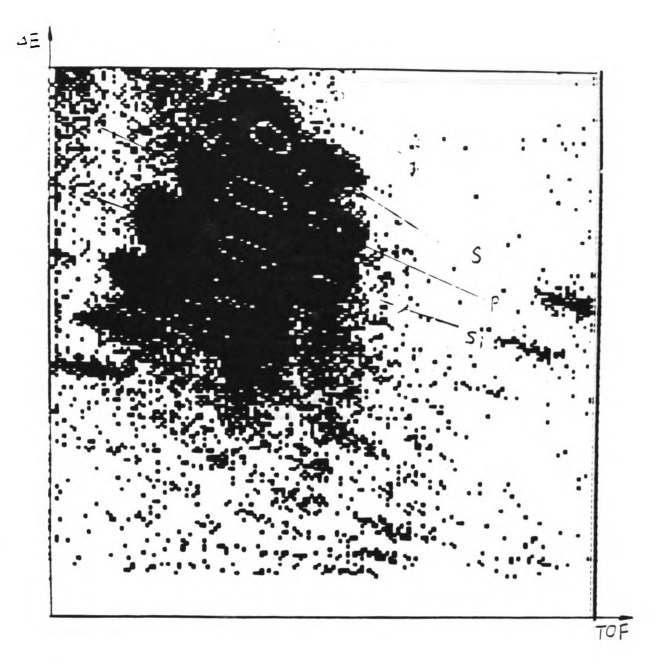


Figure 3.4: Particle identification histogram when degrader is used.

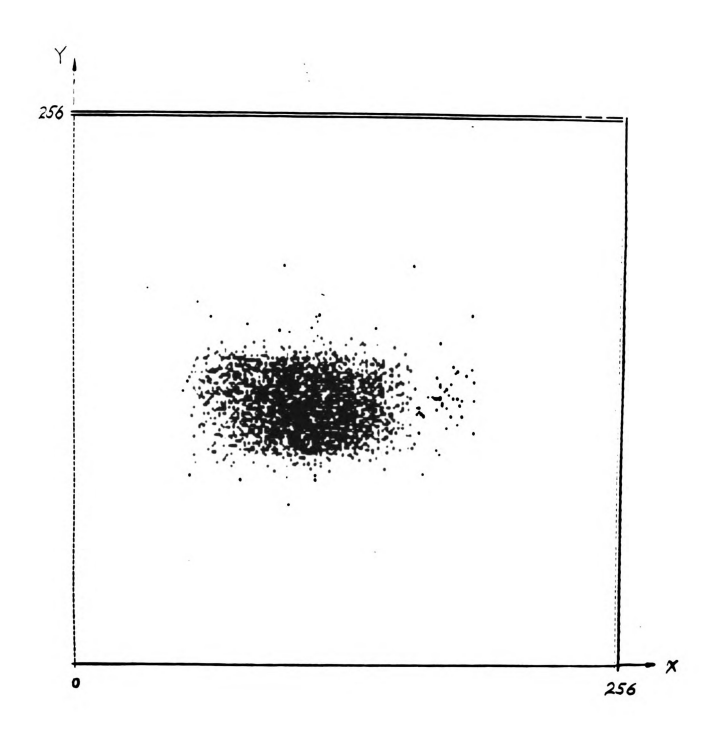


Figure 3.5: The position of <sup>32</sup>Si nuclei measured by PPAC 2

then started by turning off the bias of the stopping detector and turning the beam to full intensity (at about 40-50 ena). As explained in chapter 2, we wanted to implant in a working detector in order to to do a coincidence measurement of the activity in case the production rate of <sup>32</sup>Si was low. Unfortunately, by the time about  $3.0 \times 10^8$  <sup>32</sup>Si nuclei were implanted, the Si detector had lost most of its characteristics and was destroyed as a working detector. Since the collection rate of the <sup>32</sup>Si was large enough (5000–8000/s) to produce a sample with more than  $10^8$  <sup>32</sup>Si nuclei implanted during the experiment, the stopping detector was replaced by a passive Al foil with thickness of 123 mg/cm<sup>2</sup> and a second new implantation with about  $7.0 \times 10^8$  <sup>32</sup>Si nuclei implanted was done.

During the experiment described above, we found two things that presented a problem for us. 1.) Due the limit on the count rate of monitor, and the closeness of the  $B\rho$  settings of the A1200 at the peak production rate of the  $^{32}Si$  to the ( $^{+17}Ar$ ) beam charge state, we could not take the full advantage of the maximum yield. 2.) A puzzling problem presented itself, when we tried to simulate the implantation profile, and thus, the energy loss distribution of  $^{32}Si$  in the stopping detector, and compared the results with the measured spectrum. And as shown in figure 3.8, the measured energy loss of those  $^{32}Si$  nuclei stopped in the Si detector had a width of only about 6 % of the energy deposited, while the calculated energy deposited had a width that amounted about 30 % of that energy. With the knowledge that the A1200 had a momentum acceptance of about 3 % and that once the particles passed through a combination of mesh and absorber their energies would be down from about 42.5 MeV/A to about 16.5 MeV/A, and the absolute width of momentum distribution would be also broadened due to scattering inside the mesh and absorber, a 3 % relative width in momentum distribution was too small. This left a considerable

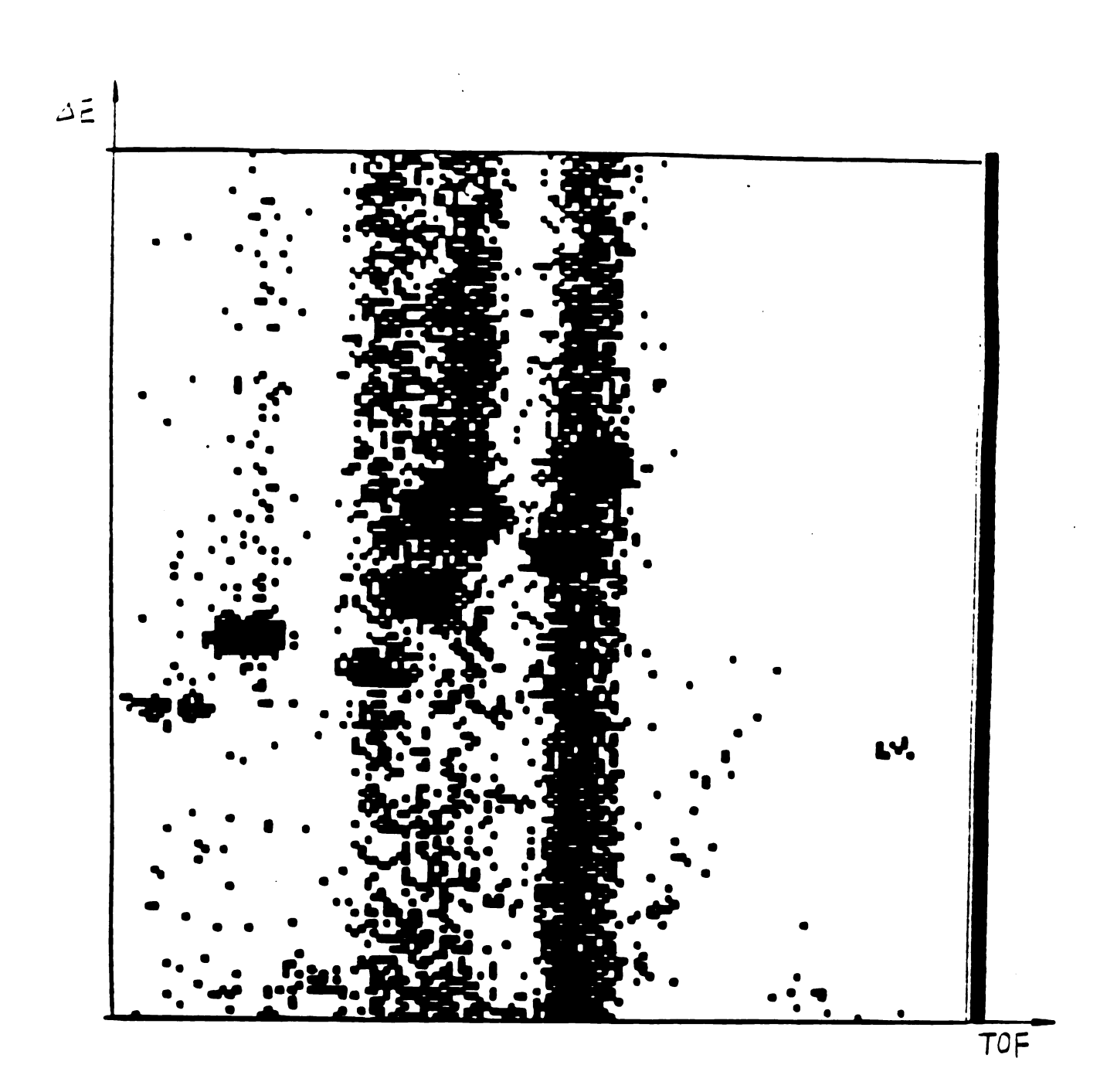


Figure 3.6: Particle identification histogram measured by the monitor detector

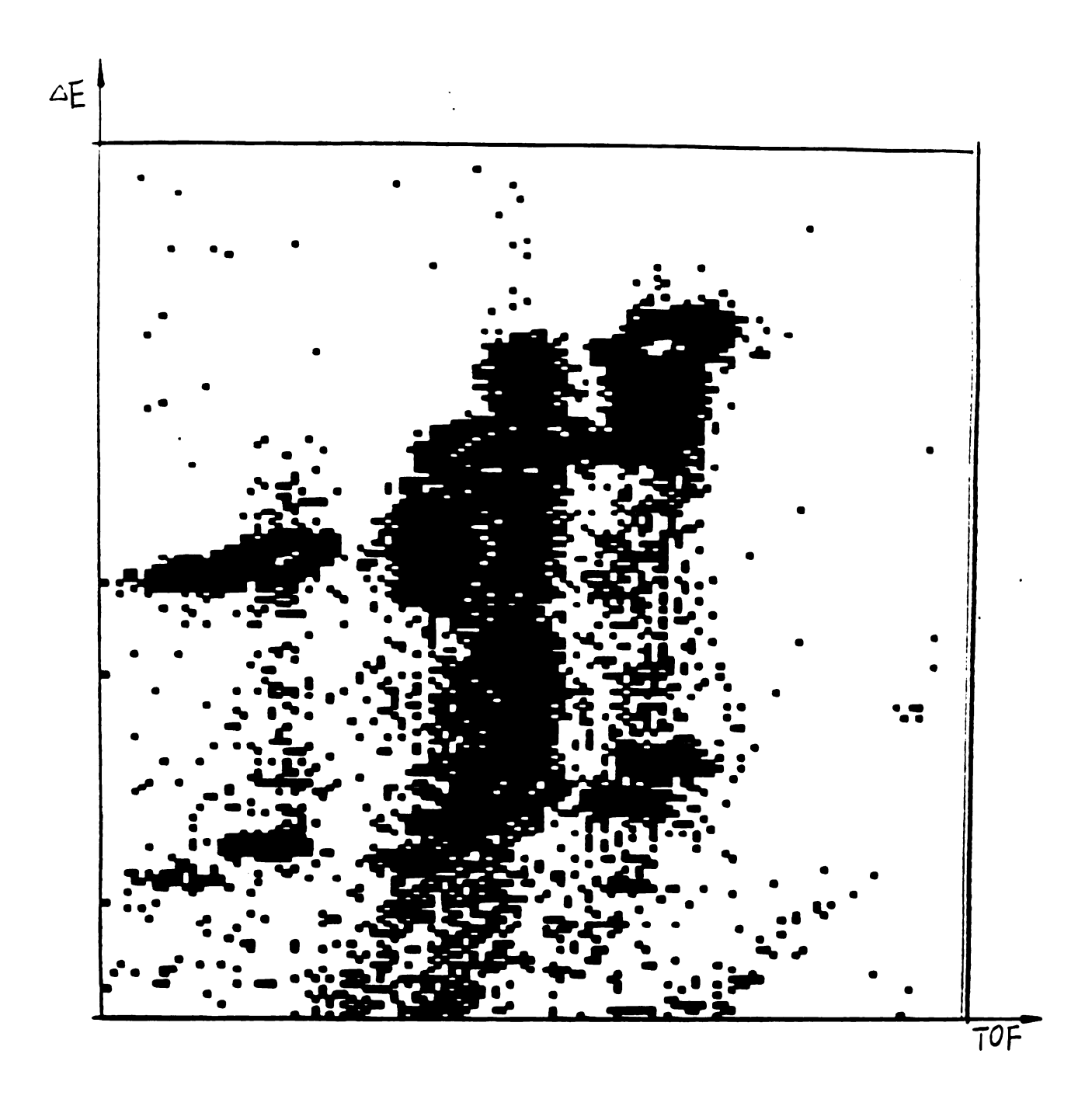


Figure 3.7: Particle identification spectrum measured by the stopping detector

uncertainty in the implantation profile and therefore would result in large errors in half-life measurement. We tried to resolve this problem, but were unable to find the cause of this discrepancy. However we were informed later that during the period of our experiment, a quadrupole was not operating properly, although there may not be any connection to the problem.

#### 3. Implantation Experiment II

The second implantation run was carried out from 8/25/91 to 8/31/91. The major difference from the first run was that during this implantation, we used 4 detectors near the target to monitor the beam intensity, and obtained the number of <sup>32</sup>Si by scaling the number of <sup>32</sup>Si nuclei measured with low beam intensity. The target monitors consisted of 4 PIN diode Si detectors positioned in the target chamber and wrapped with Al absorbers to reduce the count rate and stop electrons. They were named target monitor W, X, Y, Z, and were arranged in a configuration so that the sum of the counts in the four PIN diodes was not very sensitive to minor variations of the beam positions on target during the experiment. Therefore, the sum of count rate in those detectors in an experiment with a fixed combination of beam and target at a given energy was a measure of the beam intensity. We used this sum of counts in the monitors as a scaling factor in the place of beam current integration in this second implantation experiment.

In addition to the target monitors and standard A1200 detectors, we also had two possible apparati for the focal plane as shown in figure 3.9. One was a Si detector behind a collimator frame, the so-called 'yield monitor', which was periodically inserted at the focal plane during implantation to check the ratio of the production rate of

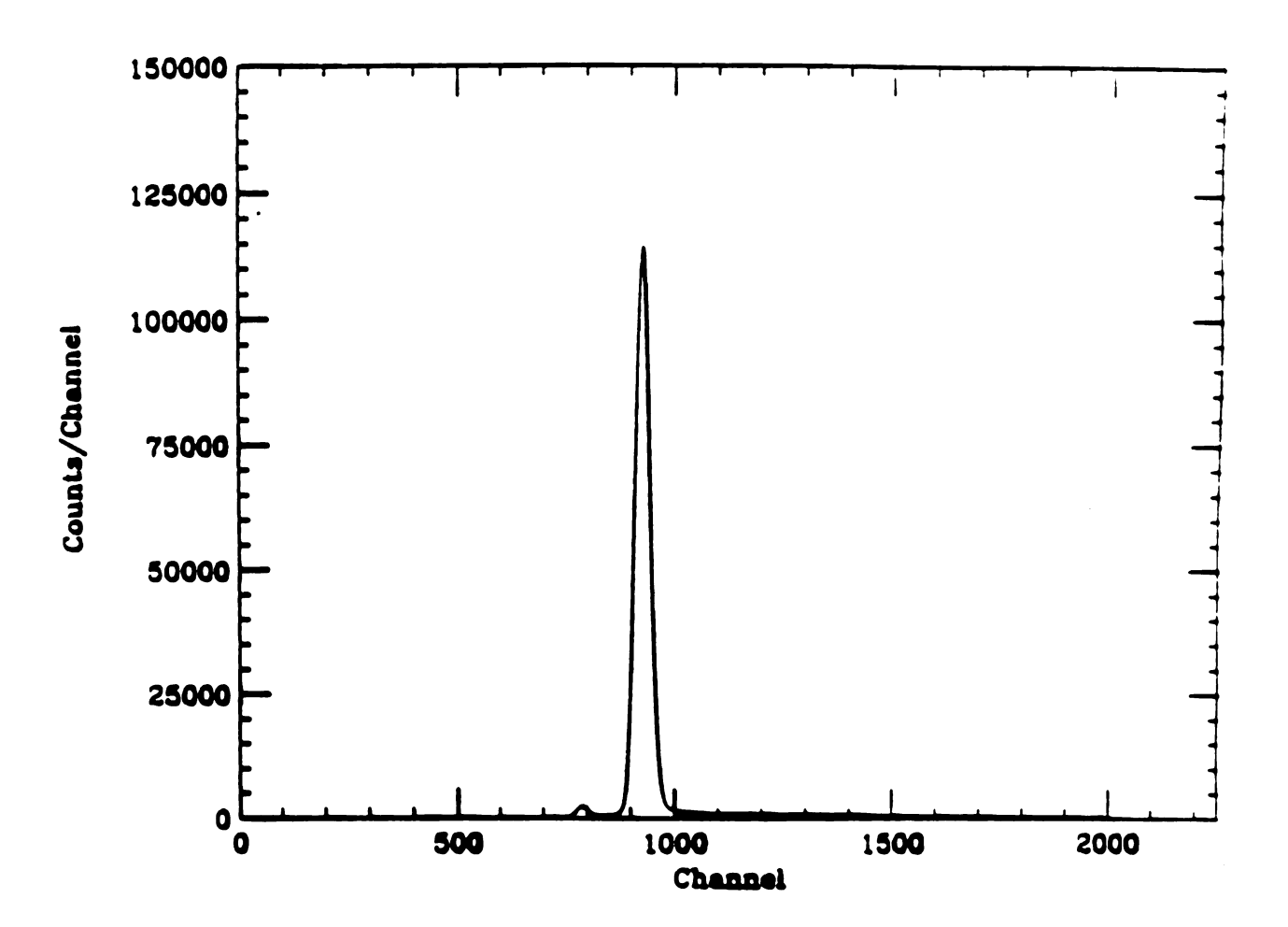


Figure 3.8: Energy loss spectrum measured by stopping detector

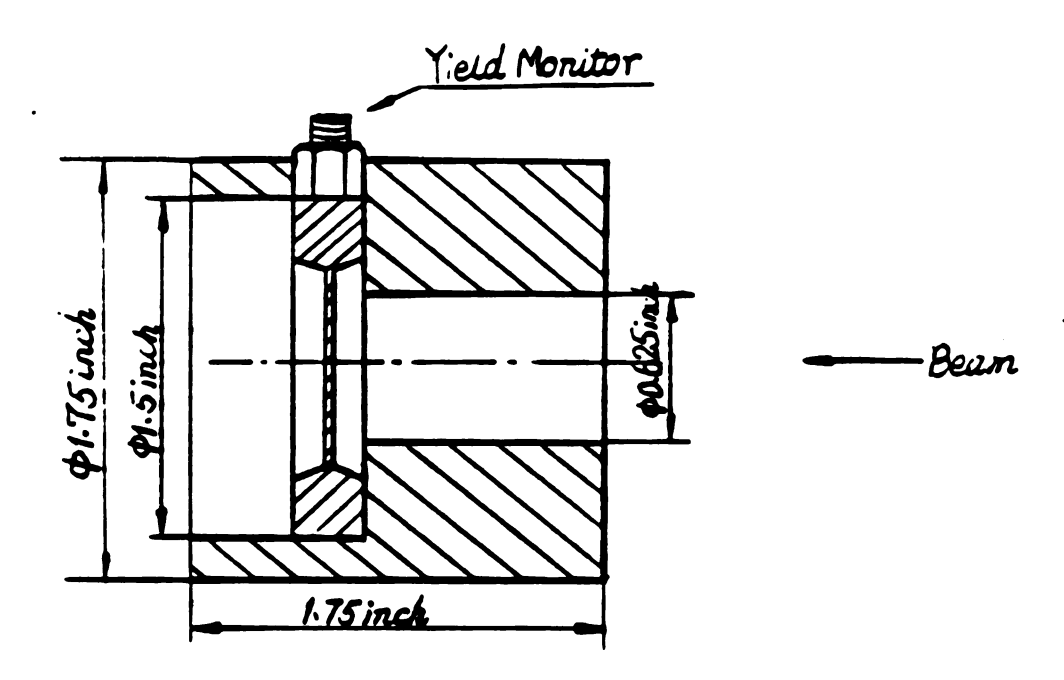


Figure 3.9: Schematic drawing of the collimator for yield monitor

 $^{32}$ Si to the count rate of the target monitors. The second consisted of a collimator frame, an absorber foil, and a stopping foil. The stopping foil was 247 mg/cm<sup>2</sup> thick for both the  $^{32}$ P implantation and the  $^{32}$ Si implantation. The absorber foil for  $^{32}$ P implantation was 108 mg/cm<sup>2</sup>, and for  $^{32}$ Si it was 260 mg/cm<sup>2</sup>. The B $\rho$  setting for both  $^{32}$ P implantation and  $^{32}$ Si were calculated before the experiment by using the programs mentioned above.

The basic setup for this experiment was not very different from that of the first one except that during the implantation, we only needed to write scalars recording the rate of the monitor detectors to tape, and only the target monitor rates were recorded online. To setup and tune the A1200 for <sup>32</sup>P and <sup>32</sup>Si, we followed the procedure of the first experiment as described above. The 2-d histogram for identifying <sup>32</sup>P is shown in figure 3.10, that for <sup>32</sup>Si is in figure 3.11. With the degrader in, the PID plots are shown in figure 3.12 and figure 3.13 for <sup>32</sup>P and <sup>32</sup>Si respectively. Once the A1200 had been setup for an isotope, we first checked whether the ratio of the yield of this isotope during a period of time to the total number of counts in the target monitors during the same period of time was a constant (within 5 %). This ratio was defined as follows.

$$R = \frac{Y_i}{C_W + C_X + C_Y + C_Z}$$

Where  $Y_i$  is the number(corrected for live time) of particles of an isotope ( $^{32}$ P or  $^{32}$ Si) that had reached the yield monitor during a run, and  $C_W$ ,  $C_X$ ,  $C_Y$ ,  $C_Z$  are the total counts in target monitor W, X, Y, Z respectively during the same run. In figure 3.14 and 3.15, the measured ratios for  $^{32}$ P and  $^{32}$ Si are plotted against beam attenuation factors. From those plots, one can see that those ratios are essentially independent of the beam intensity. We started implantation by putting the implanta-

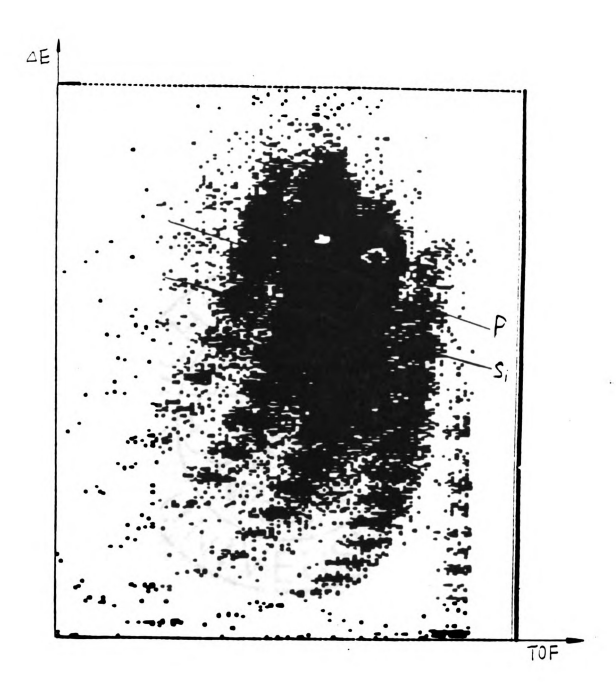


Figure 3.10: PID spectrum with magnetic field set for  $^{32}\mathrm{P}$  implantation (without degrader)

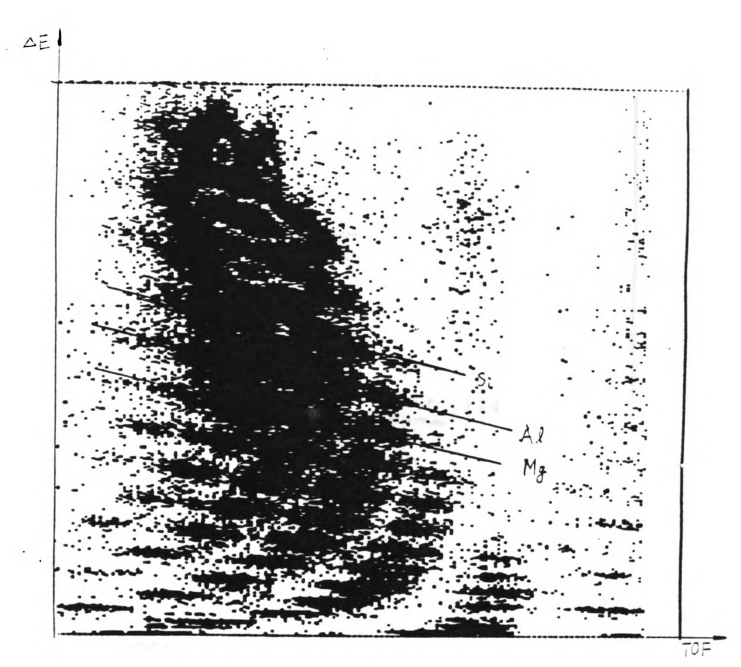


Figure 3.11: PID spectrum with magnetic field set for  $^{32}\mathrm{Si}$  implantation (without degrader)

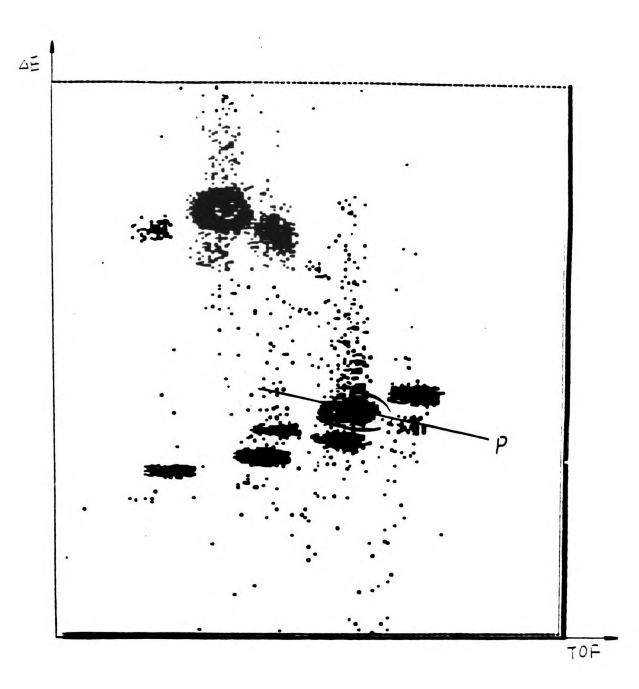


Figure 3.12: PID spectrum with magnetic field set for  $^{32}\mathrm{P}$  implantation (with degrader)

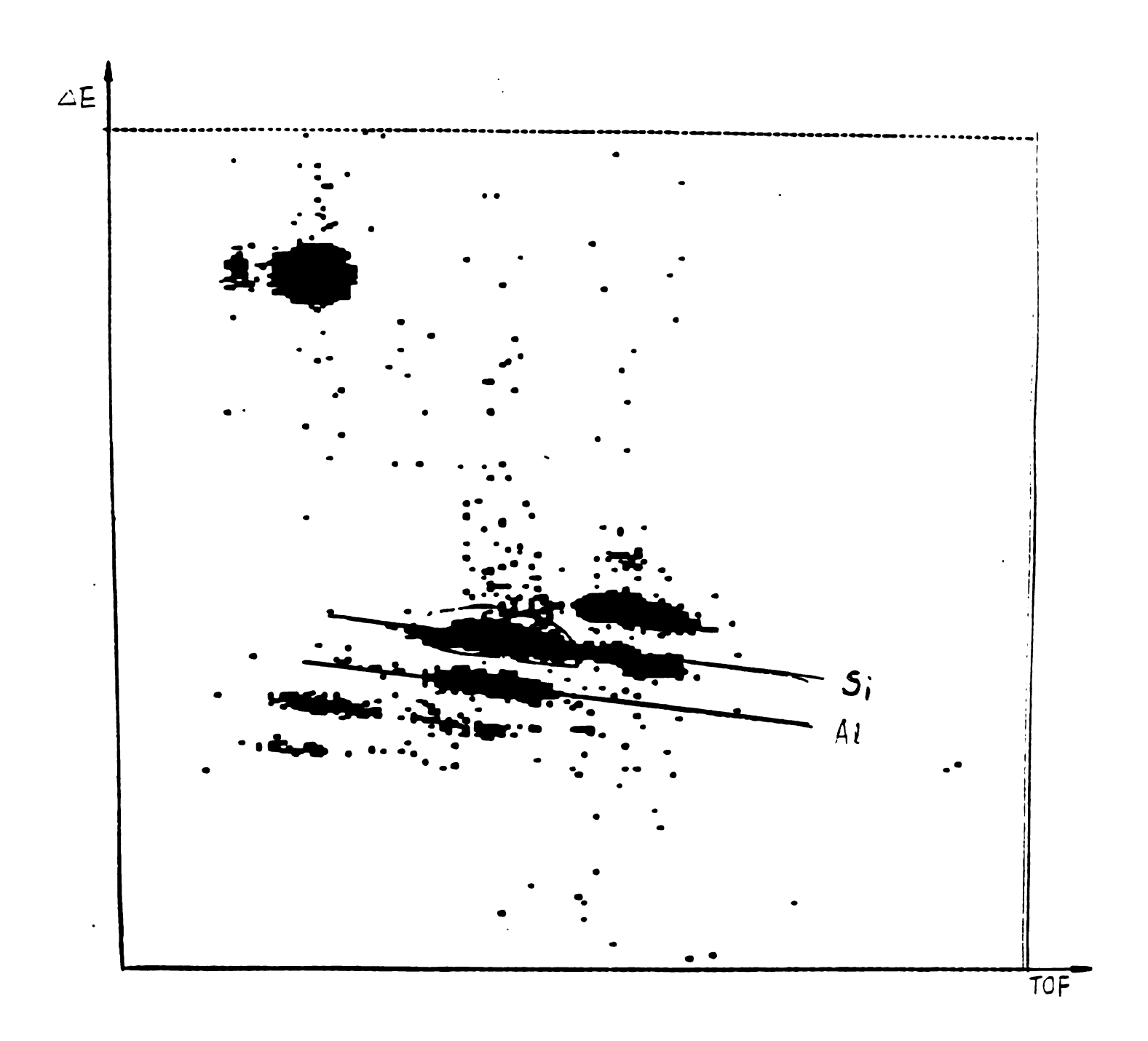


Figure 3.13: PID spectrum with magnetic field set for <sup>32</sup>Si implantation (with degrader)

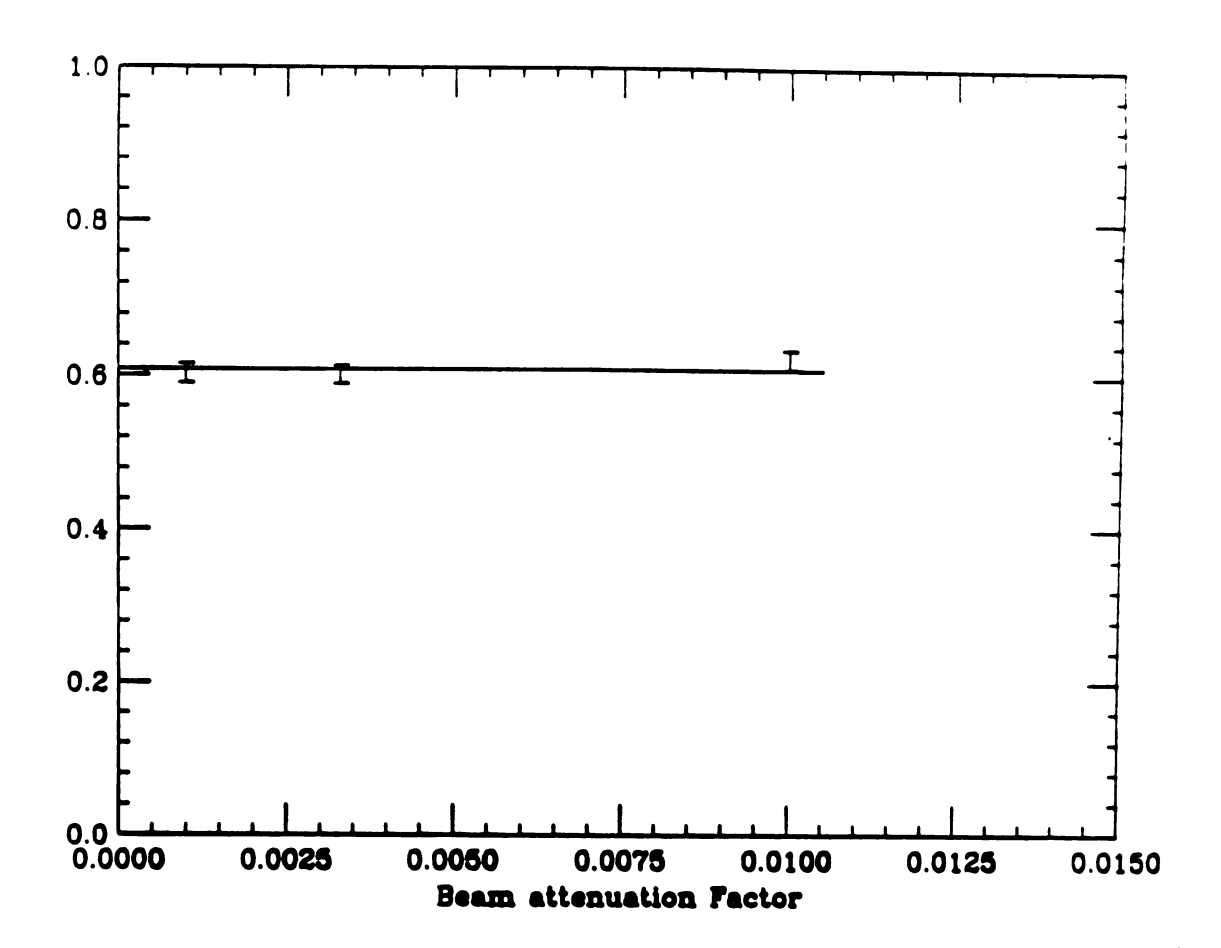


Figure 3.14: Measured ratio R(as defined in the text) as a function of beam attenuation factor before the implantation of  $^{32}P$ 

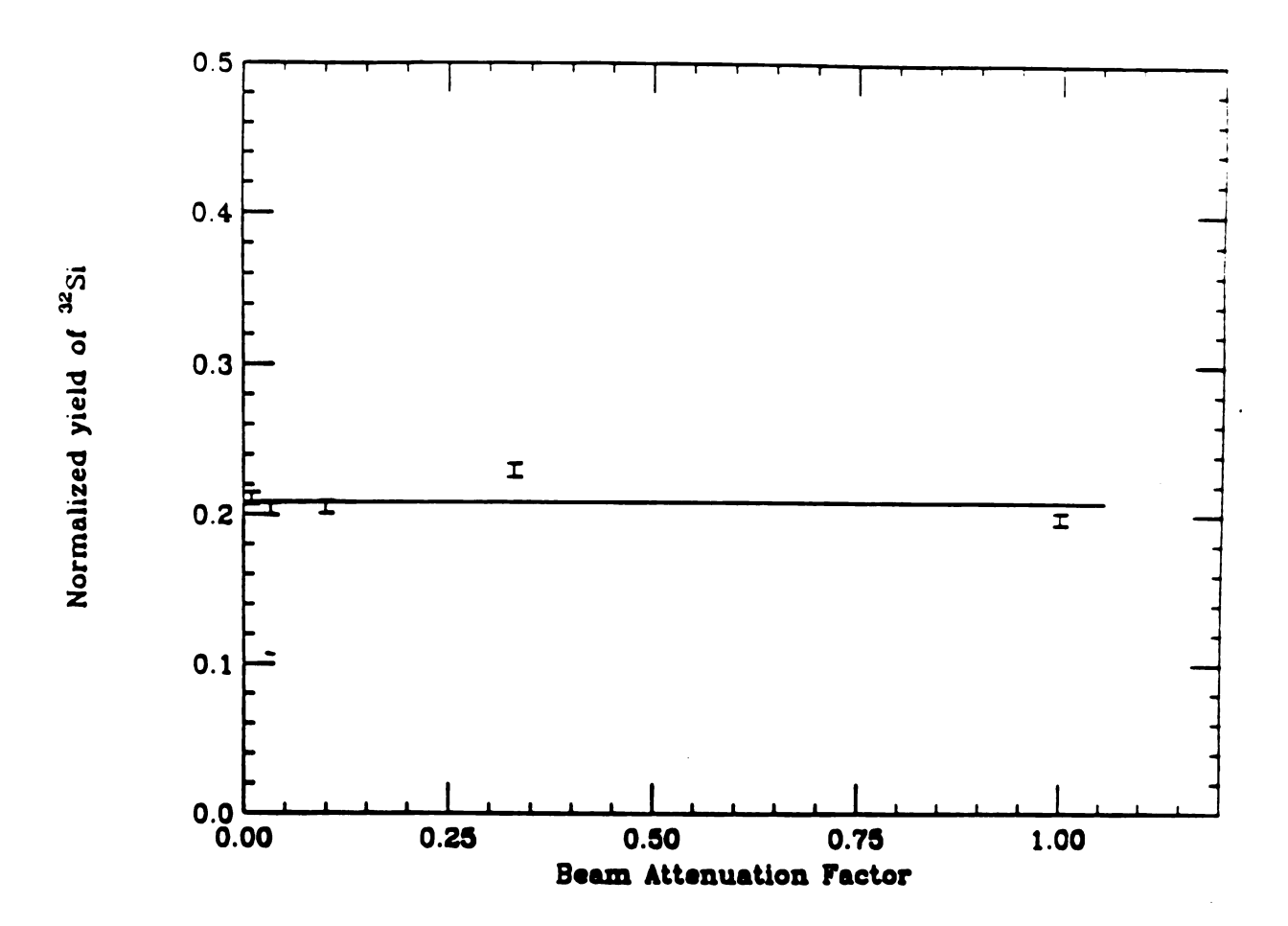


Figure 3.15: Measured ratio R(as defined in the text) as a function of beam attenuation factor before the implantation of  $^{32}$ Si

tion stack at the focal plane and turning up the beam intensity. We obtained two  $^{32}$ P samples each with about 1/2 hour of implantation and about  $6\times10^6$   $^{32}$ P nuclei. The ratio R defined above was measured before and after both of the implantation runs so that the number of  $^{32}$ P nuclei implanted could be calculated using those values of R measured immediately before and after the implantations. The implantation of  $^{32}$ Si lasted 36 hours. On the average, after every  $1\frac{1}{2}$  hours of implantation, the yield monitor stack was put at the focal plane to measure the value of R defined above so that the number of  $^{32}$ Si nuclei implanted during this period could be calculated using those values of R measured immediately before and after the period of implantation. This way the uncertainties in the number of implantations of  $^{32}$ Si nuclei could be reduced. At the end of the experiment, a sample with about  $7.74\times10^8$   $^{32}$ Si nuclei was obtained.

### II Momentum Distribution

As explained in Chapter 1, to gather some data on the momentum distribution of <sup>32</sup>Si and that of those isotopes with same A in projectile fragmentation, we did an experiment to measure the momentum distributions of the isotopes with a mass number 32 in projectile fragmentation of <sup>40</sup>Ar on <sup>9</sup>Be and <sup>181</sup>Ta at 80 MeV/A. The experiment was carried out from 6/22/91 to 6/28/91. The targets were 47 mg/cm<sup>2</sup> Be and 84 mg/cm<sup>2</sup> Ta which are roughly equivalent in stopping power. The thicknesses were chosen so that the broadening of the momentum in the target for the particles was limited to about 2 %. The measurement was done by using the first half of the A1200 as a spectrograph. The PPAC1 detector at image 2 was used to measure the position of the dispersed particles and, therefore the momenta of the particles. The particles, which were not stopped at image 2, were brought to the focal plane for the purpose of particle identification so that the momentum distribution of the nuclei of individual

isotope could be generated. The detector used were the standard PPAC1 at image 2, and PPAC2, PPAC3 at focal plane. Instead of the 325 mg/cm<sup>2</sup> PIN diode Si detector, an ion chamber was used to measure the energy loss of the particles at the focal plane. A thin scintillator start detector at image 1 was also used to improve the time resolution of the time-of-flight measurement. To make a measurement in the B $\rho$  range of interest with good statistics, we did a yield calculation using code Intensity [Win 91], (an empirical calculation based on fitting and interpolation) as shown in figure 3.16. The B $\rho$  settings that we intended to cover is indicated by a horizontal bar near the abscissa. With each field setting covering about 2 % in B $\rho$ , we needed about 20 different settings of B $\rho$  during the experiment to cover the whole range of interest.

To setup the A1200, we first sent the fully stripped beam through the spectrometer, and calibrated the ion chamber by comparing the measured energy loss of the beam to that calculated. The beam energy was obtained from the setting of the dipole field of the first half of the A1200 when the beam was centered at image 2. This gave 79.9 MeV/A for energy of the beam. The position response of the PPAC1 at image 2 was then calibrated by varying the  $B\rho$  settings of the first half of the spectrometer, and in figure 3.17, a histogram of the measured beam positions at various  $B\rho$  setting is shown. This histogram yields an effective radius calibration for particles reaching image 2, and we can then measure the momentum distributions for various isotopes. We then set the  $B\rho$  value of the A1200 for  $^{32}$ S whose yield was predicted to be highest. Its A/Z value of 2 made it especially easy to identify. The 2-d PID histogram with particles identified for this field setting is shown in figure 3.18. Following the particle identification, we began the momentum distribution measurement by setting the  $B\rho$  values of the A1200 according to those values in figure 3.16. However, some

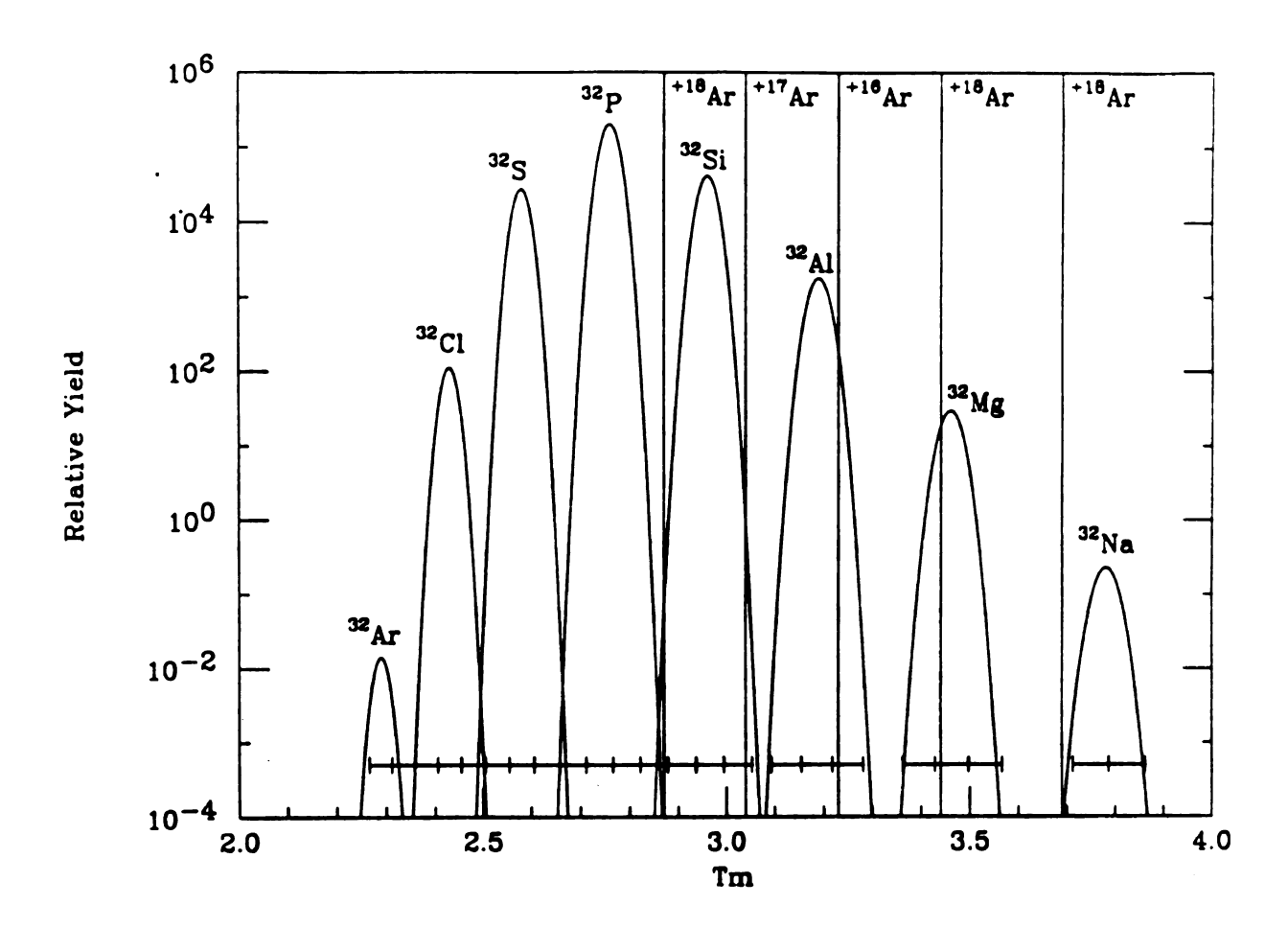


Figure 3.16: Calculated yields of A=32 isotopes(using Intensity [Win 91]) for the reaction of 85 MeV/A  $^{40}$ Ar on Be

field settings in the figure were too close to the values where the beam charge states obscured the isotope of interest. In figure 3.19, those field settings that were covered, together with the predicted relative yields, and charge state of the beam are shown, and can be compared with figure 3.16.

As shown in figure 3.18, the number of isotopes that were present and well resolved at a given field settings were quite large (30 - 60). Therefore, as a by product of the measurement of momentum distributions for mass = 32 nuclei, the momentum distributions of a large number of other isotopes were also measured.

## III Counting

We began to count the samples from the first implantation experiment immediately after the experiment and continued to count until the beginning of the second implantation experiment. During this time span of about 4 months, we alternately measured the sample and background with two 500  $\mu$ m thick, 300 mm<sup>2</sup> Si transmission detectors by using the experimental arrangement shown in figure 3.20. The detectors were calibrated with a combination of sources and pulser. In figure 3.21, spectra of <sup>57</sup>Co and <sup>131</sup>Ba measured by one of the Si detectors are shown. We then calibrated an Ortec pulser by setting the pulser to match the positions of those peaks. The calibrated pulser was later used to find the thresholds which we wished to set in the software to measure the number of counts above those thresholds.

The background was measured by counting an Al disk of the same size as the sample which had been subjected to a similar environment as the implanted sample

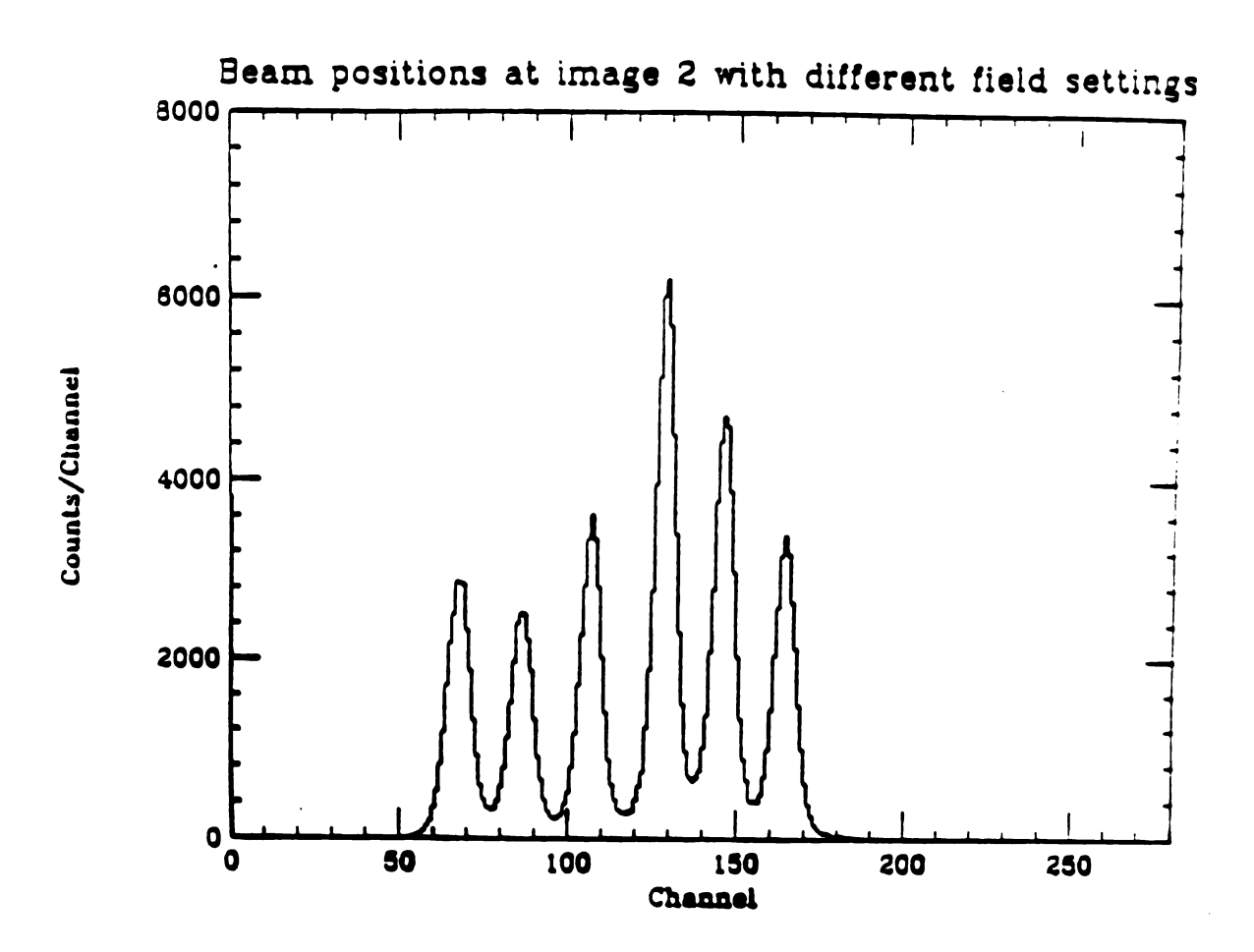


Figure 3.17: Beam positions measured by PPAC1 at image #2 with different field settings

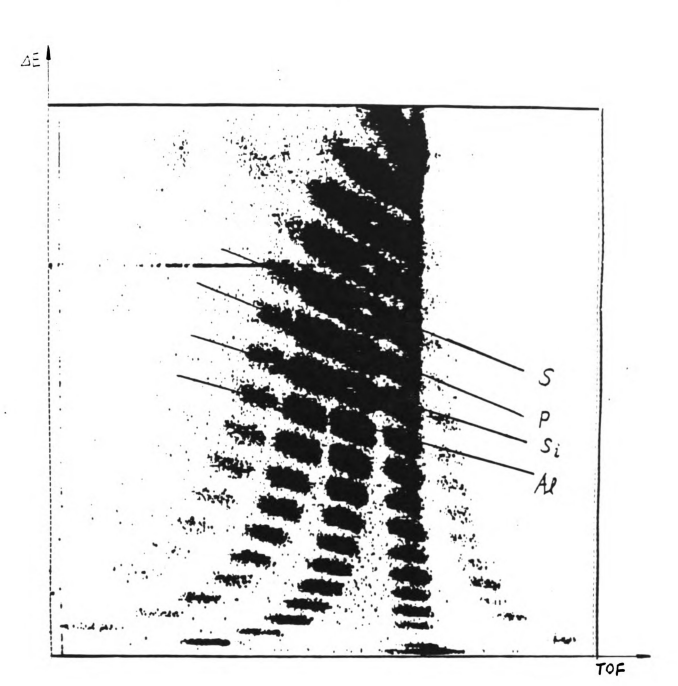


Figure 3.18: A typical PID histogram during the momentum distribution measurement

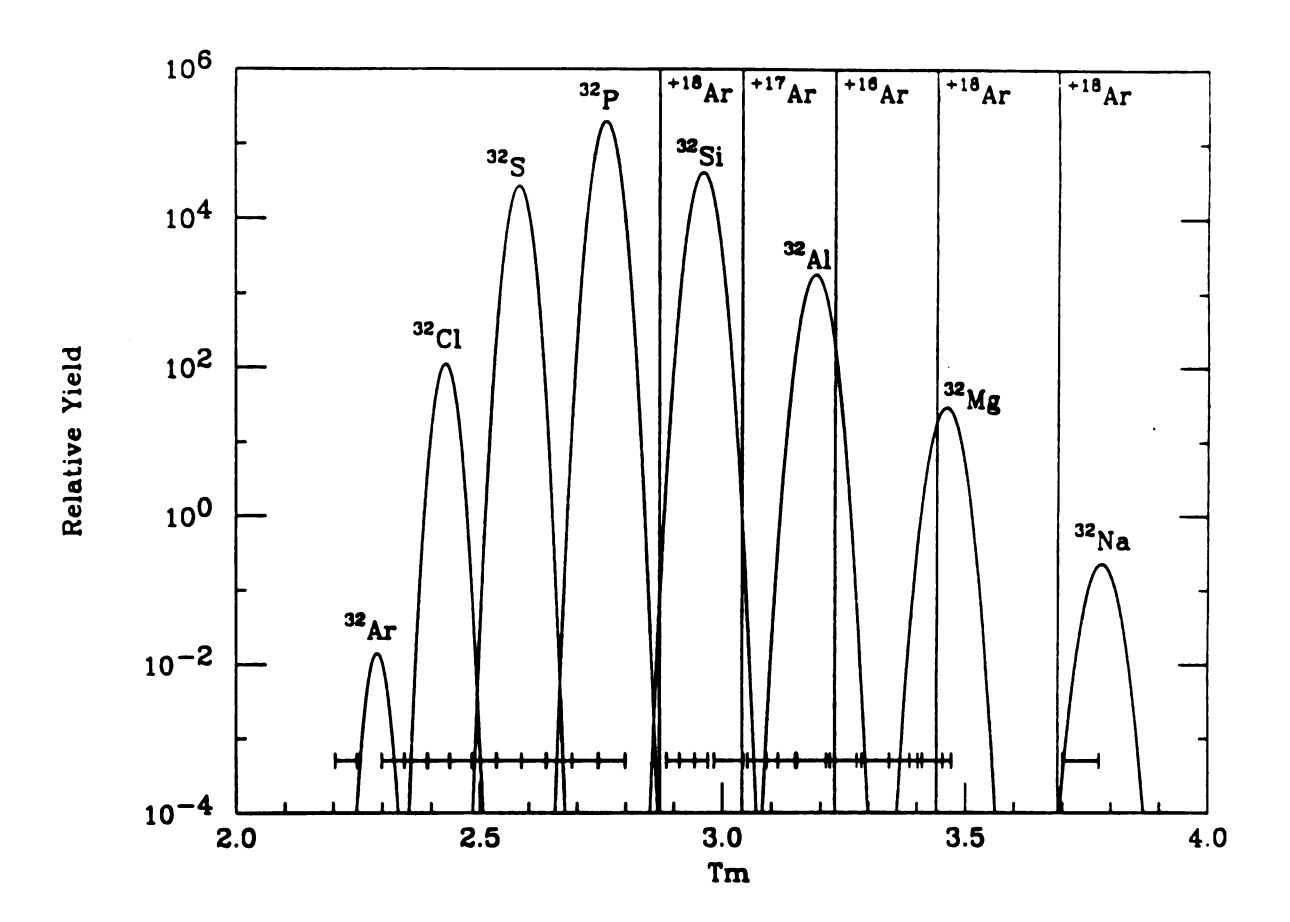


Figure 3.19: Actual field setting covered during the momentum distribution measurement

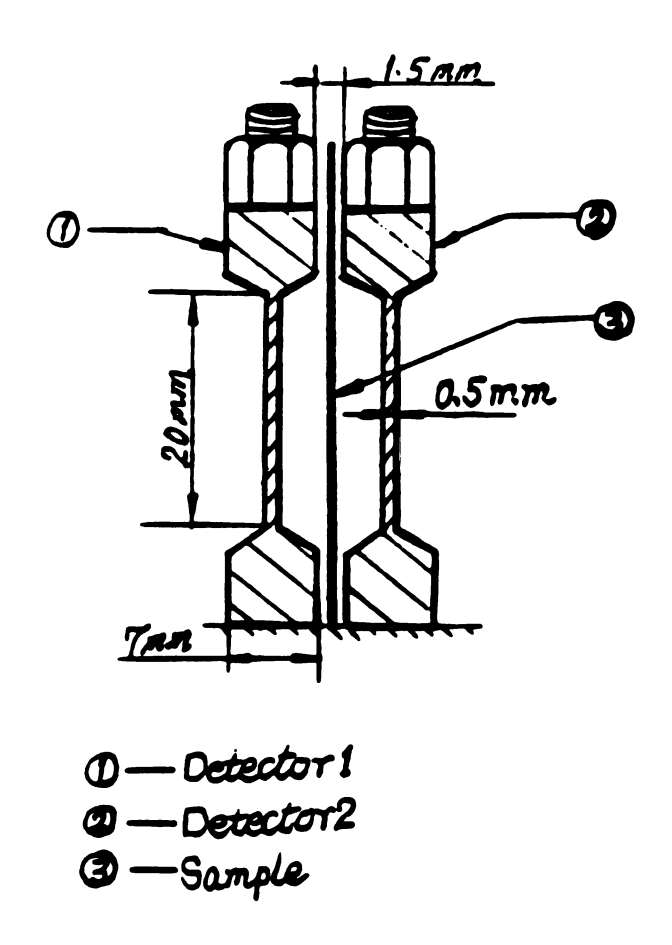


Figure 3.20: Detector arrangement for activity determination.

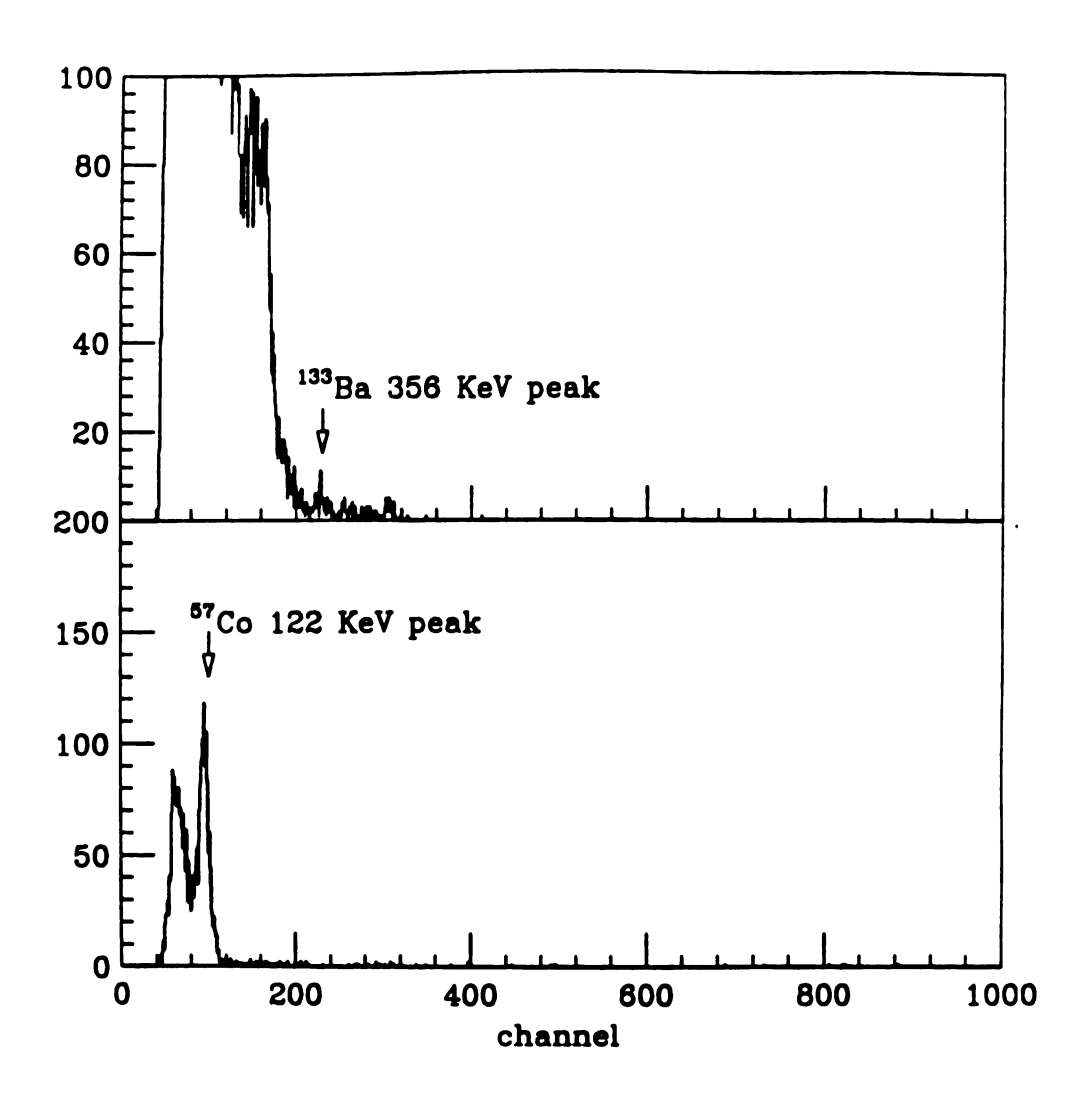


Figure 3.21: a.) 122 KeV line of the <sup>57</sup>Co measured by detector 1, b.) 356 KeV line of the <sup>133</sup>Ba source measured by the same detector

during the experiment. Between background measurements, there were a calibration test with the pulser and a sample measurement. On the average, each background measurement lasted about 3 days. The energy and time of occurrence of each event were recorded by the computer and written on the disk. Therefore, the time and energy spectra could be generated later. In figure 3.22, histograms of number of counts vs. time of those events with measured energies greater than 100 KeV from the Si detectors are shown. One can see that the background was stable over a period of a few days. The long term stability of the background could be checked from data obtained in different measurements.

The Al foil sample obtained during the first implantation experiment was measured in the same configuration as the background disk. After every sample measurement, there was a pulser test of the detector to check the calibration of the detectors. A <sup>57</sup>Co spectrum was also measured periodically to check any changes in pulser calibration. The time span of each sample measurement varied a lot from measurement to measurement. At the beginning of the measurement, there were some short lived activities from contaminants implanted during the experiment in the sample. To observe the decay of those short lived contaminants, the sample measurement lasted from 1 to 2 weeks. In figure 3.23, a histogram of counts vs. time for those events with energy deposition greater than 100 KeV in one of the Si detectors is shown. This was from the first sample measurement immediately after implantation. One can clearly see the decay. After the count rate of the sample stabilized somewhat, the sample measurements were reduced to 3 – 5 days long. A typical count v.s. time histogram during this period is shown in figure 3.24.

The samples from the second implantation experiment were counted beginning

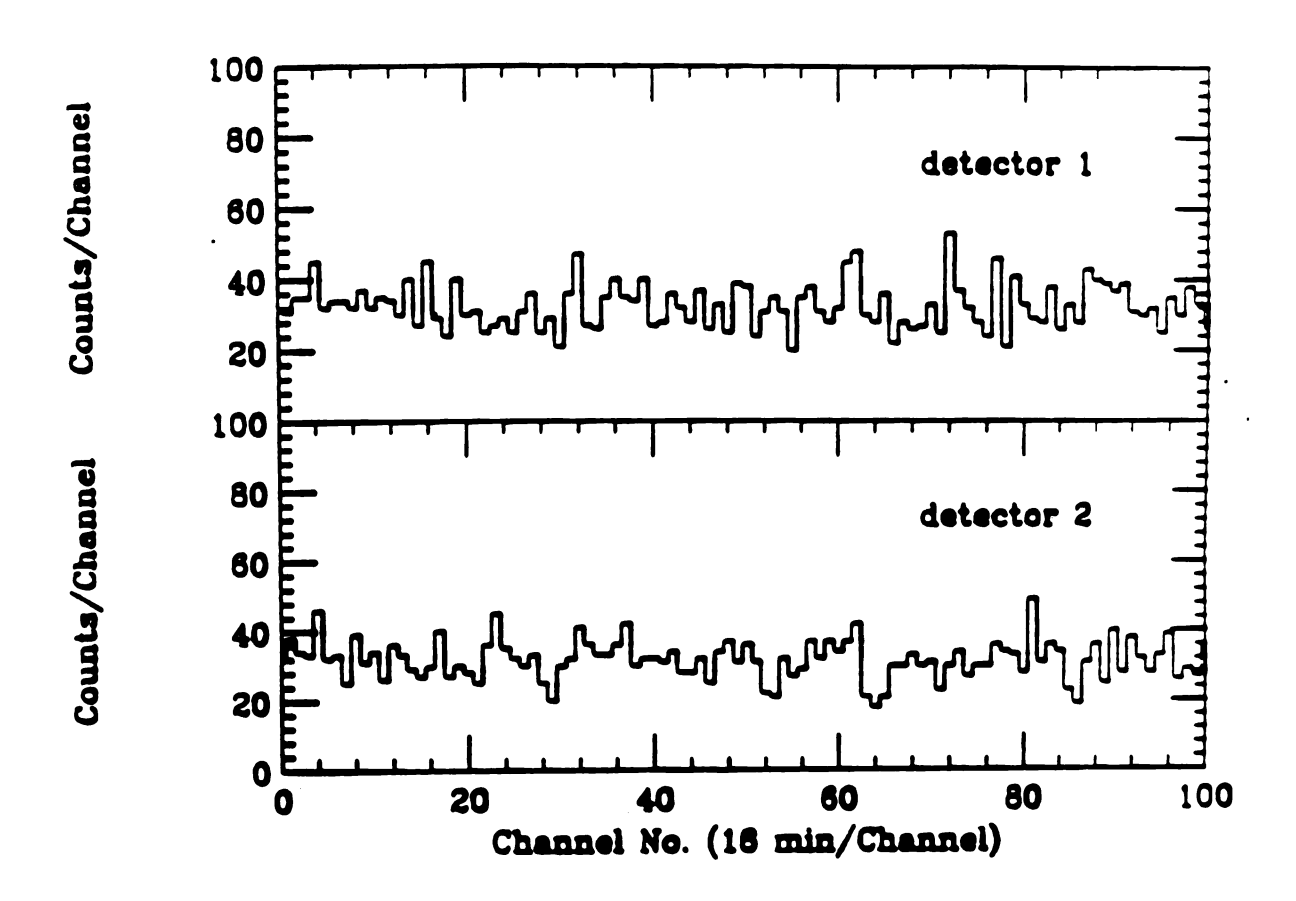


Figure 3.22: Background events with energy deposition greater than 100KeV as a function of time.

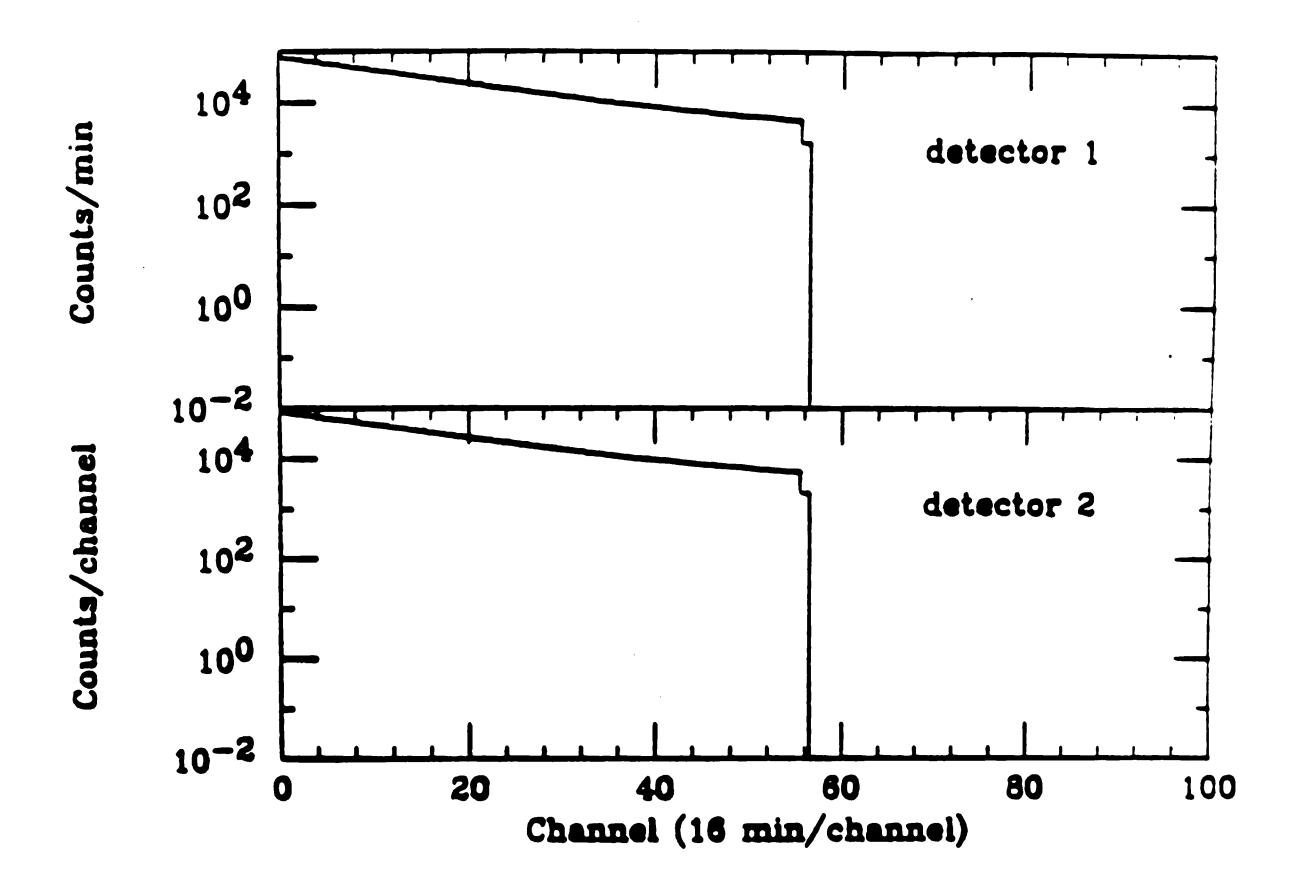


Figure 3.23: number of events measured (when the sample was between the two counters) as a function of time immediately after the first implantation

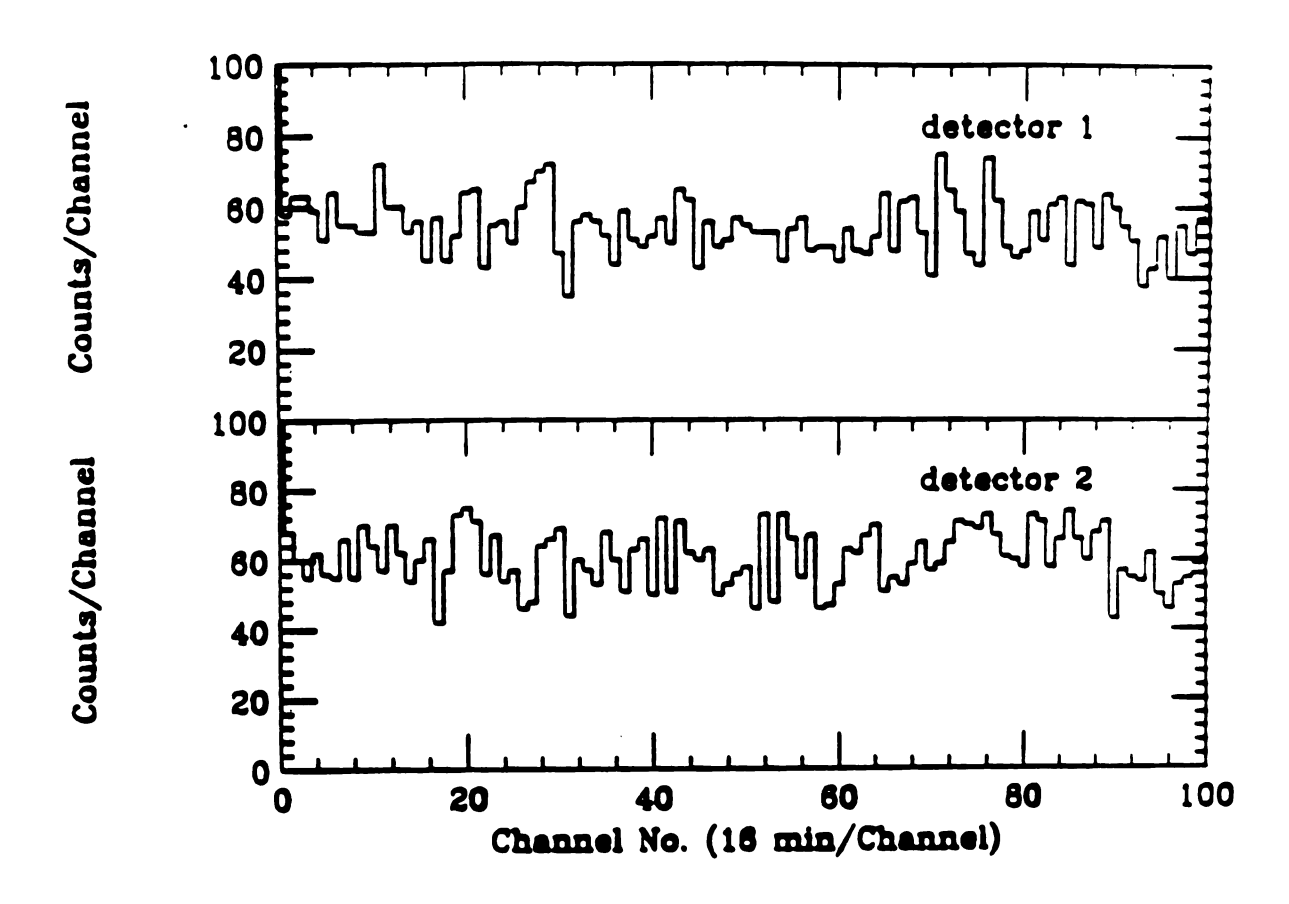


Figure 3.24: Number of events measured (when sample was between the counters) as a function of time (60 days after the implantation).

9/3/91. To make the counting environment more stable, a copper box was built to hold the detectors and the sample. Nitrogen gas was made to circulate in the box to keep the temperature constant. The counting configuration of the detectors was modified slightly to allow thicker foils to be counted, and the calibration of the detectors was checked again. The background was measured by counting an Al foil of the same size as the sample. On the average, each background measurement lasted 1 day. In figure 3.25, results from a typical background measurement are shown. The average background count rate plotted against time is shown in figure 3.26.

The two <sup>32</sup>P samples obtained during the implantation were labeled as P<sub>1</sub> and P<sub>2</sub>, the background foil was labeled as 'B', the <sup>32</sup>Si sample as 'Si'. They were counted in the sequence Si, P<sub>1</sub>, P<sub>2</sub>, B. Each sequence of counting lasted 4–6 days, after every two measurements in a sequence of counting, a pulser test of the detectors was performed, and after every sequence of counting, a <sup>57</sup>Co source test was performed to check the pulser calibration. The above sequence of counting was maintained until most of the <sup>32</sup>P nuclei in the samples had decayed, and the count rate approached to that of background. In figure 3.27 and 3.28, the results from a measurement for each sample are shown. In figure 3.29 and 3.30, the count rates of the samples in the detectors are plotted against mean measurement time. Since the half-life of <sup>32</sup>P is well known, one can obtain the efficiency of the counting system from the above results, and this will be discussed in detail in the next chapter.

The sample implanted with <sup>32</sup>Si nuclei, labeled 'Si' had some short lived contaminants. This can be seen from figure 3.31, a plot of the count rate of the sample vs. mean measurement time. The count rate stabilized after about 80 days of counting. A measurement of the 'Si' sample after the count rate stabilized is shown in figure 3.32.

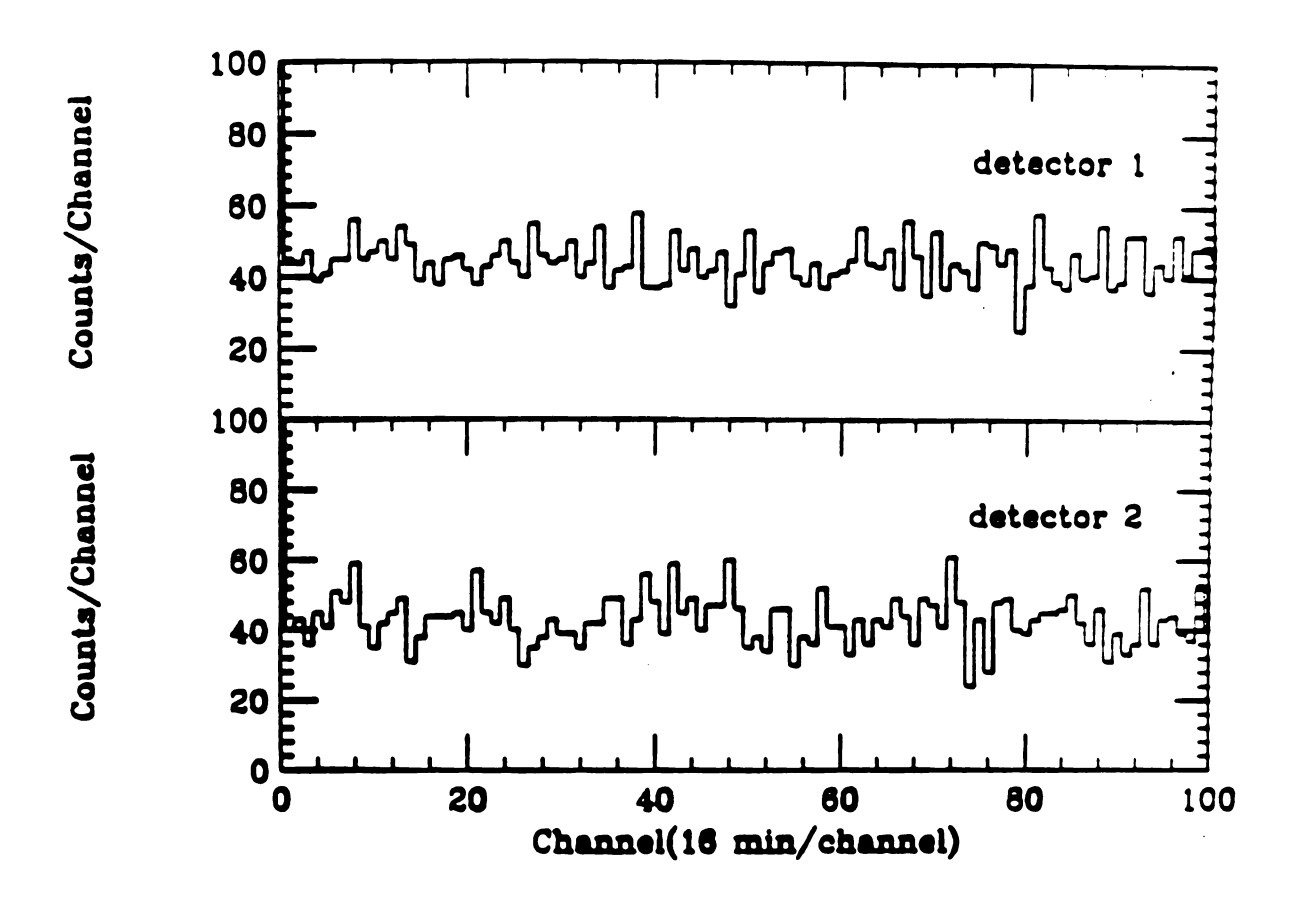


Figure 3.25: Background events as a function of time after the modification of the sample holder and shielding.

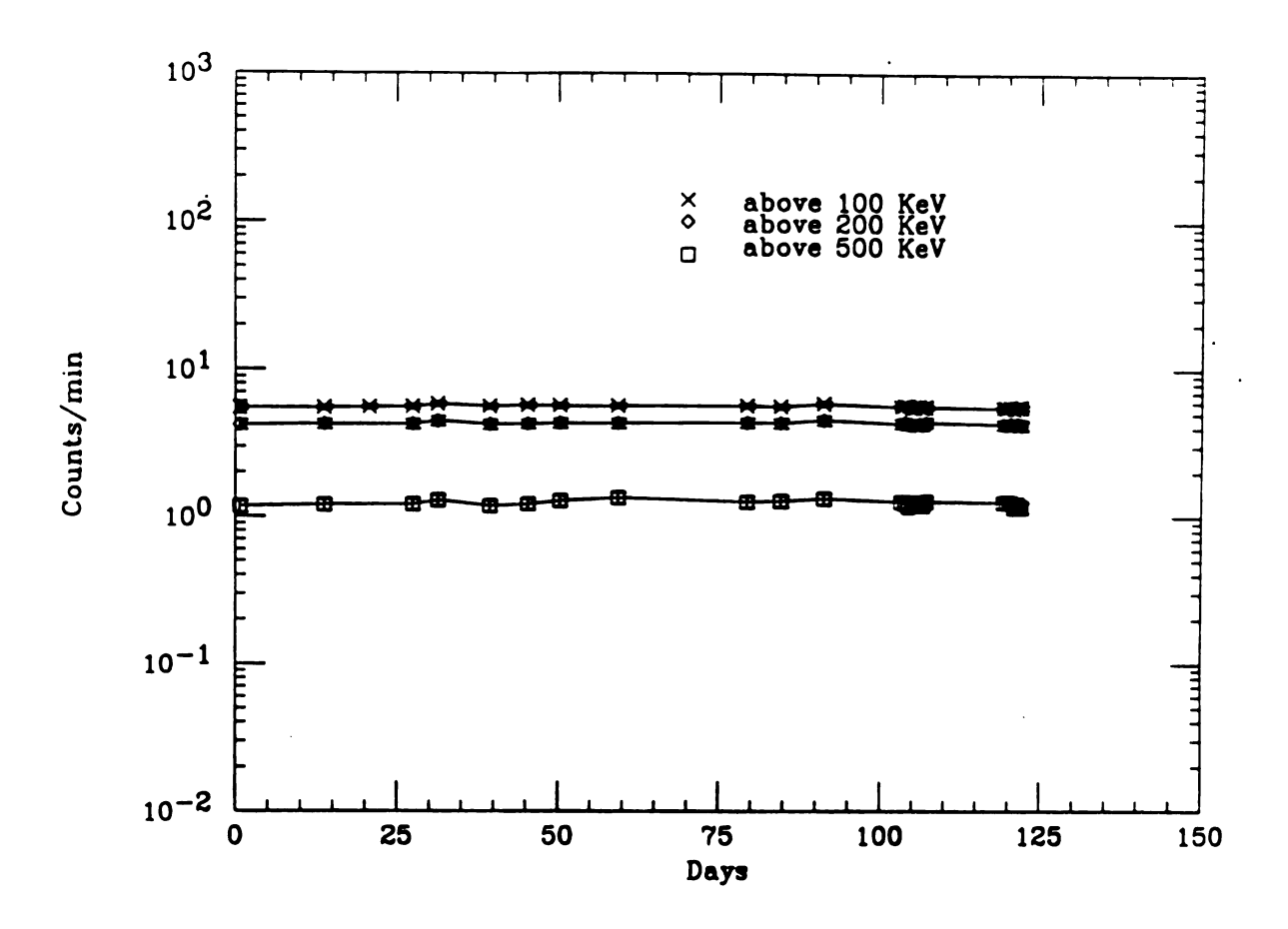


Figure 3.26: Measured average background count rates with different threshold as a function of time

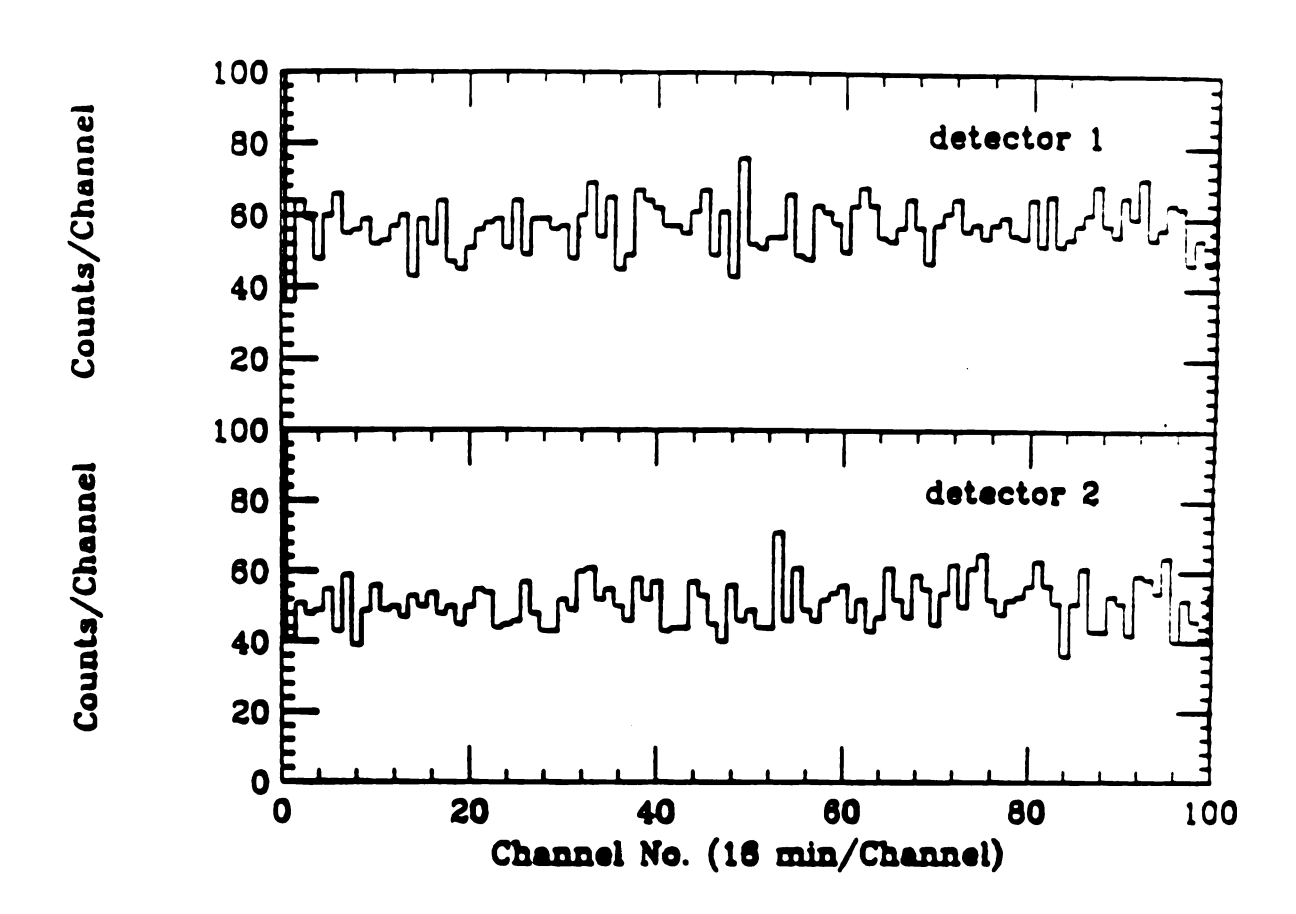


Figure 3.27: Number of events as a function of time (when sample P<sub>1</sub> was between the counters)

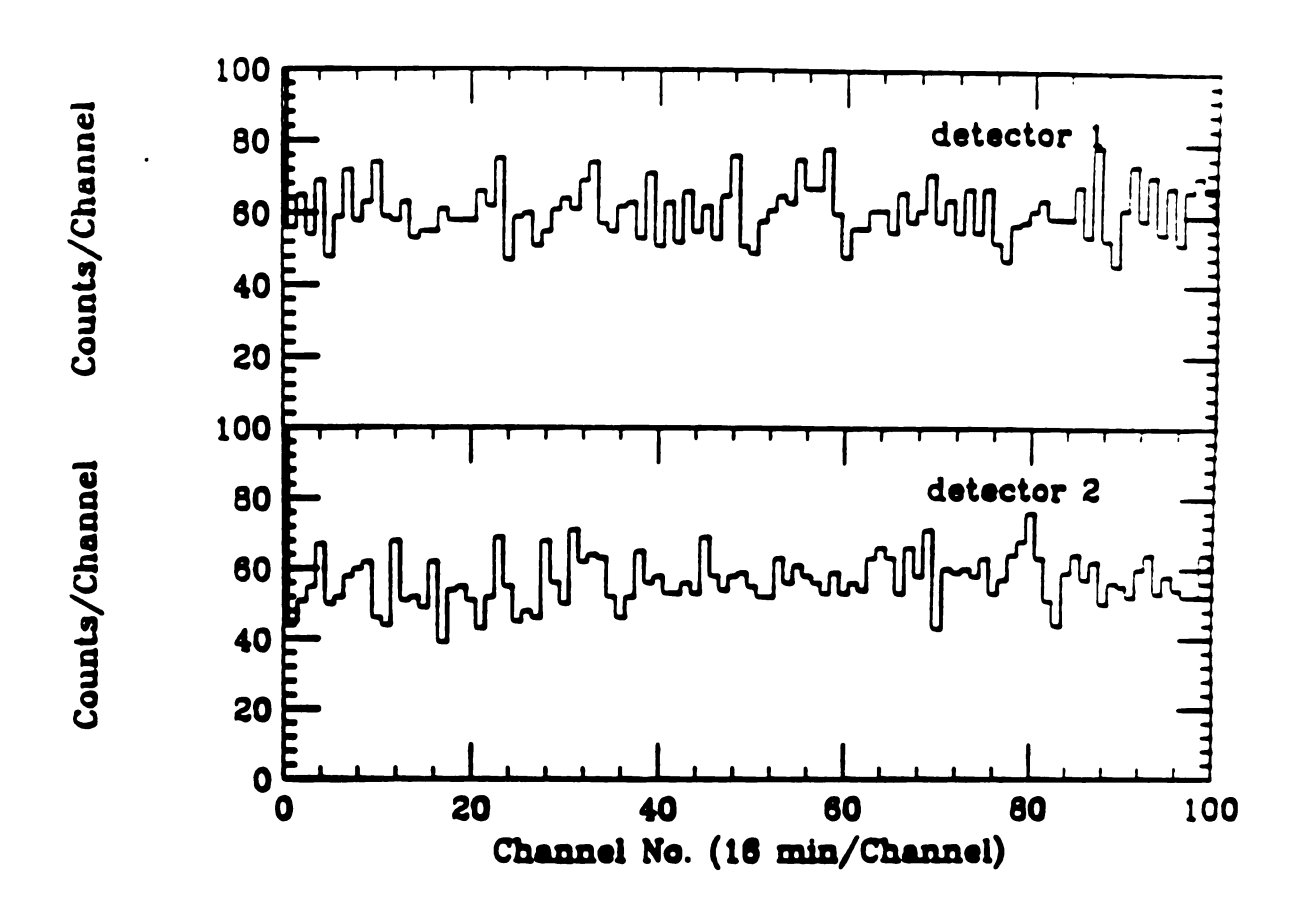


Figure 3.28: Number of events as a function of time (when sample P<sub>2</sub> was between the counters)

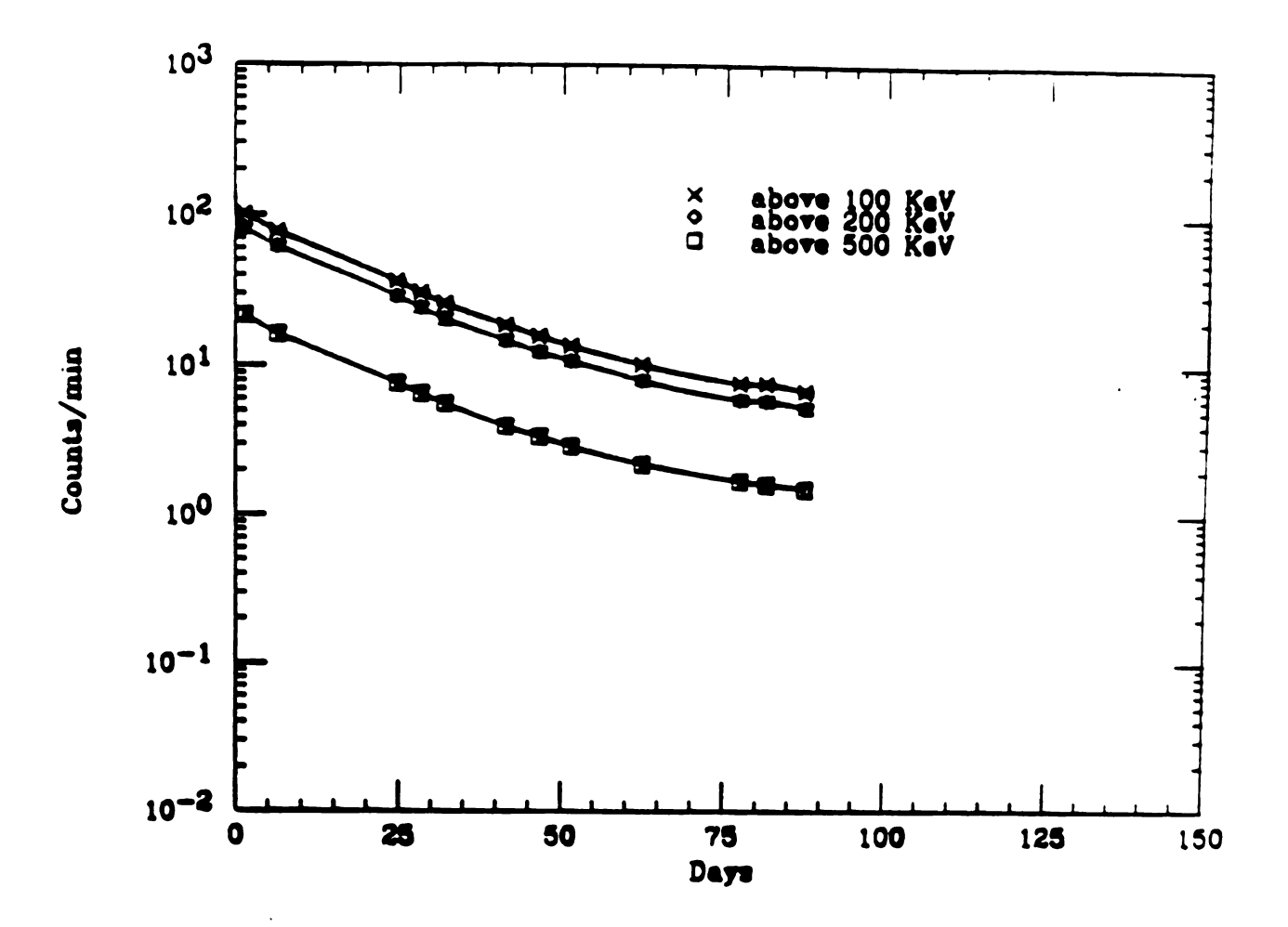


Figure 3.29: The average count rates of sample  $P_1$  with different thresholds as a function of time

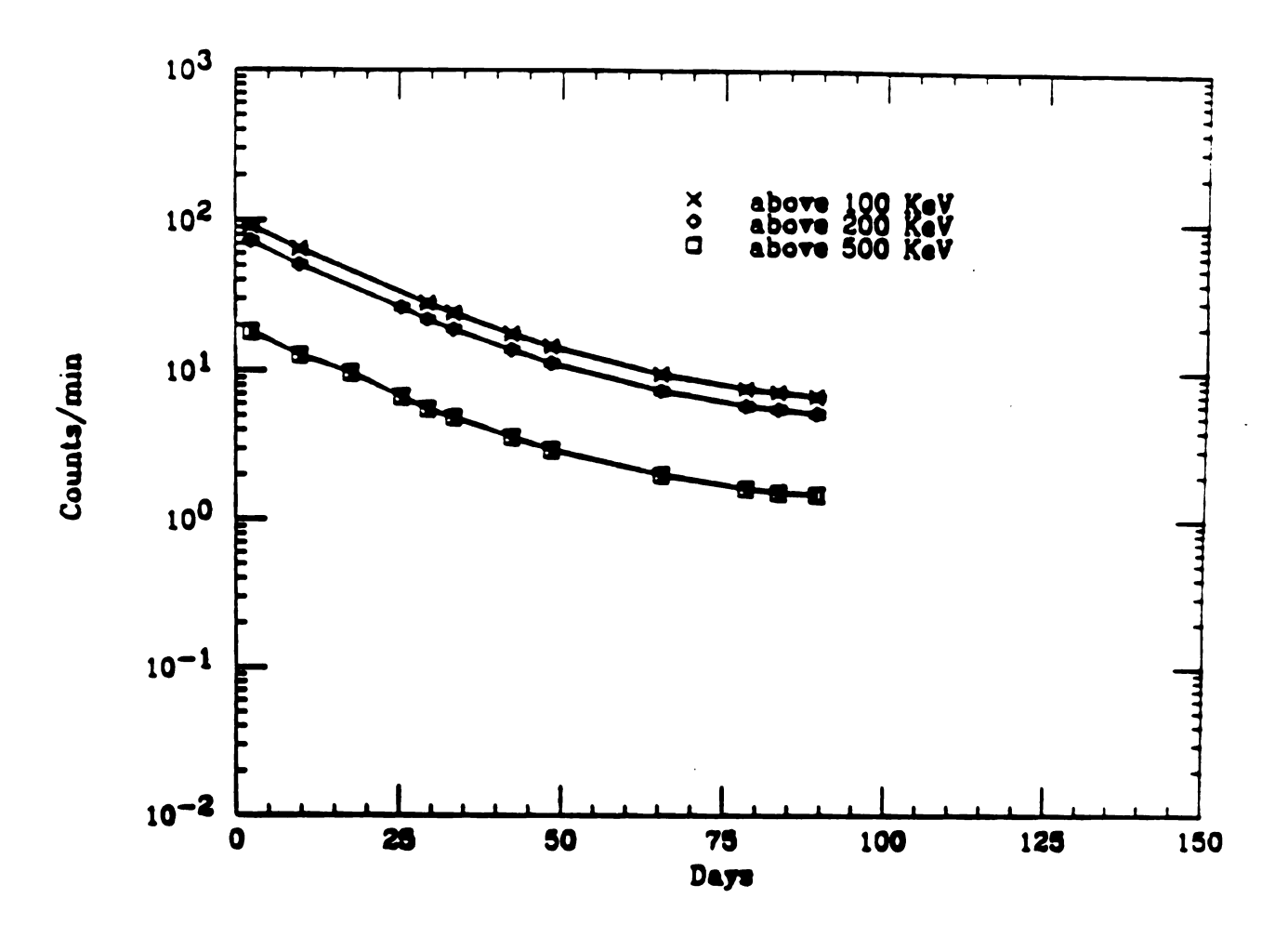


Figure 3.30: The average count rates of sample P<sub>2</sub> with different threshold as a function of time

The results from those sample measurements combined with the background measurements, and <sup>32</sup>P sample measurements were used to extract the half-life of <sup>32</sup>Si. This will be discussed in the next Chapter.

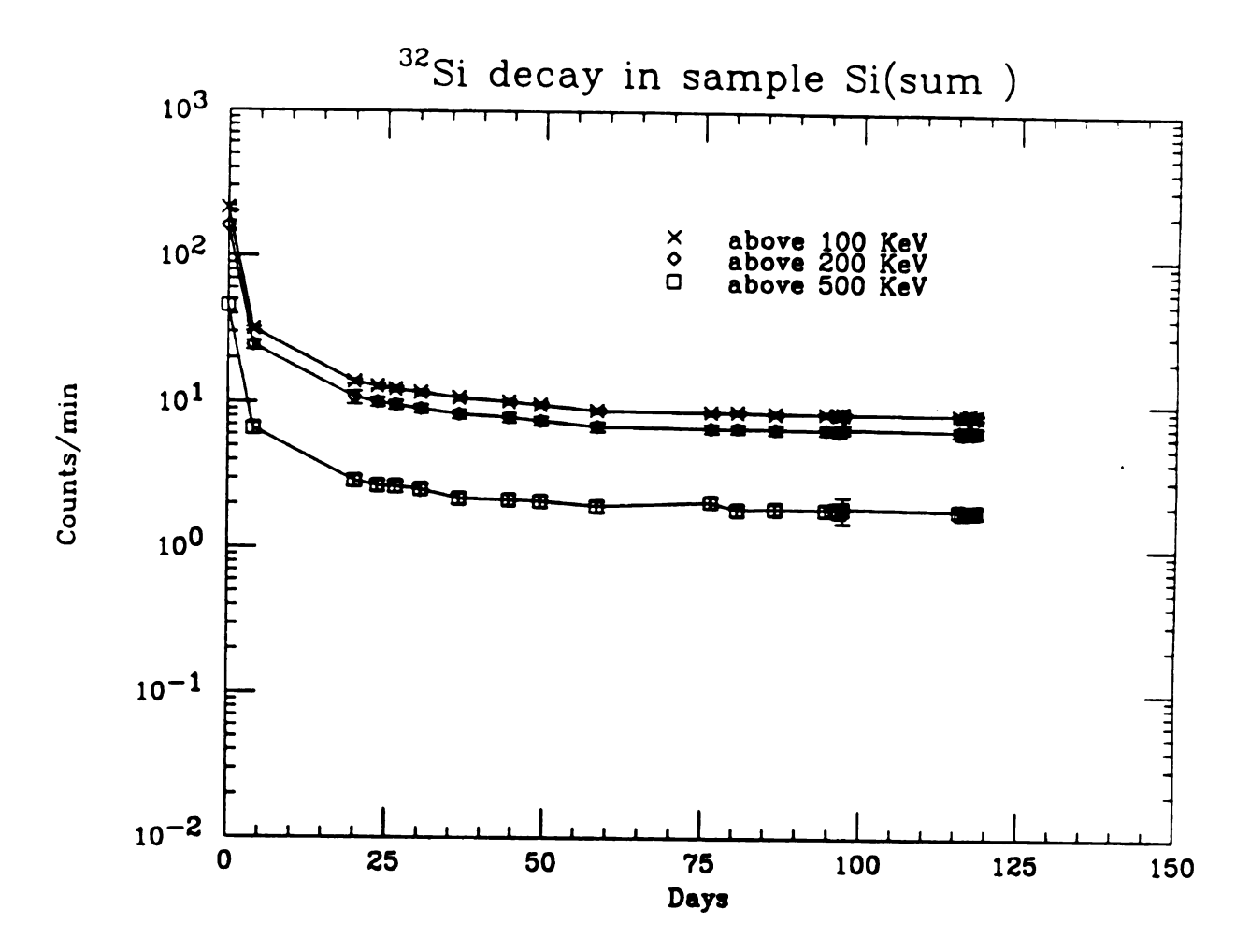


Figure 3.31: The average count rates of sample Si with different thresholds as a function of time.

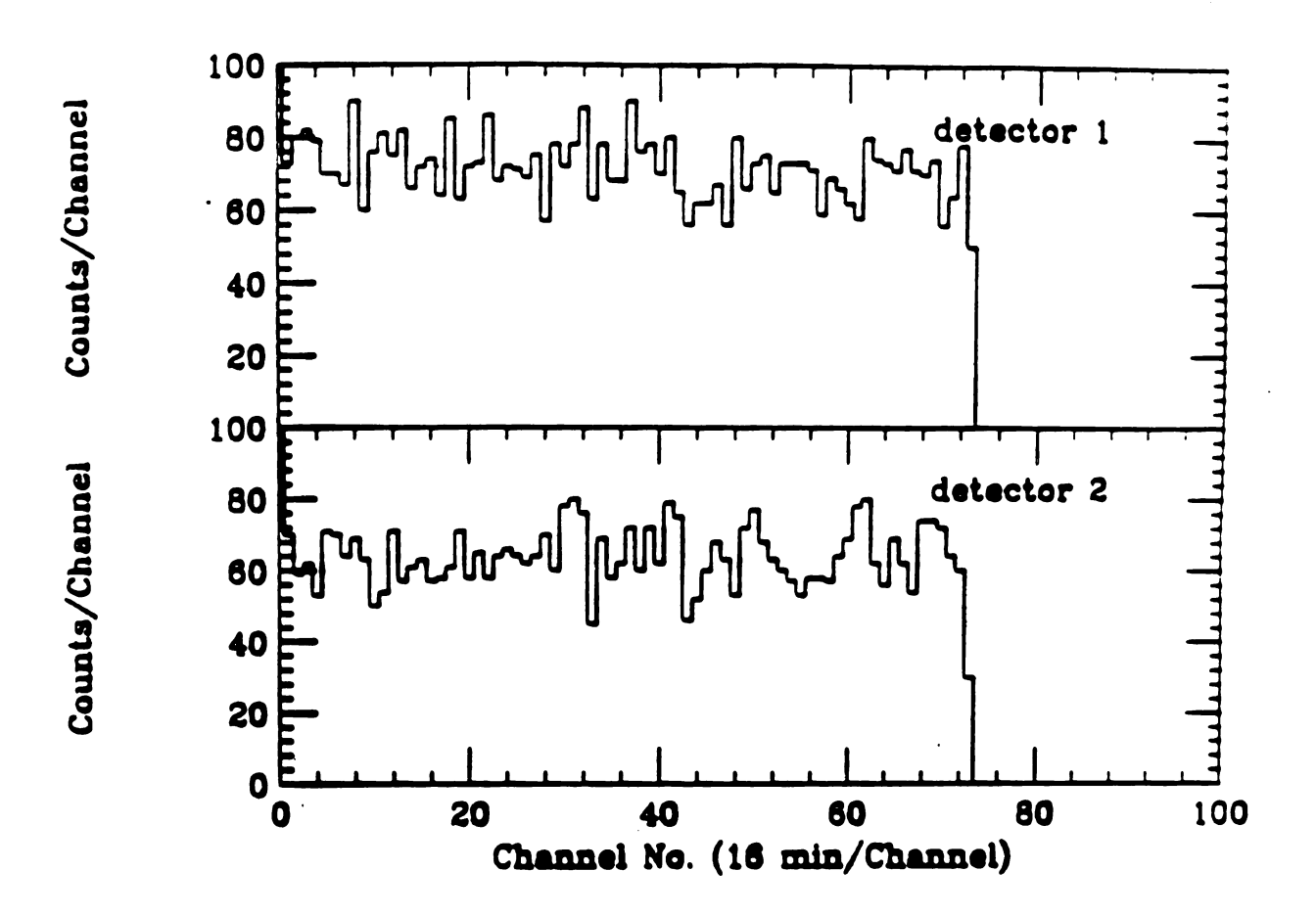


Figure 3.32: The number of events as a function of time measured the two counters (when the Si sample was between the counters. Threshold 100 KeV)

# Chapter 4

# Analysis

## I <sup>32</sup>Si half-life

#### 1. Implantation experiment 1

To determine the number of nuclei of an isotope implanted, we need to know the transmission efficiency of the mesh, and the accumulated counts of the nuclei in the monitor corrected for decay during implantation. We used the data obtained during the transmission calibration part of the experiment mentioned in chapter 2 to obtain the transmission efficiency of the mesh. In figure 4.1, the two dimensional histogram of energy deposition of particles in the 'stopping' detector vs. the time-of-flight of the particles is shown. One can see two groups of particles in the figure, those with smaller energy deposition and narrower energy spread, and those with more energy deposition in the detector and larger energy spread. The particles with smaller energy loss signals are those that passed through the holes of the mesh, and were therefore more energetic and able to go through the stopping detector without stopping. The particles with higher energy loss signals (figure 4.1) are those that passed through the bulk part of the mesh and were stopped in the stopping detector. For a given

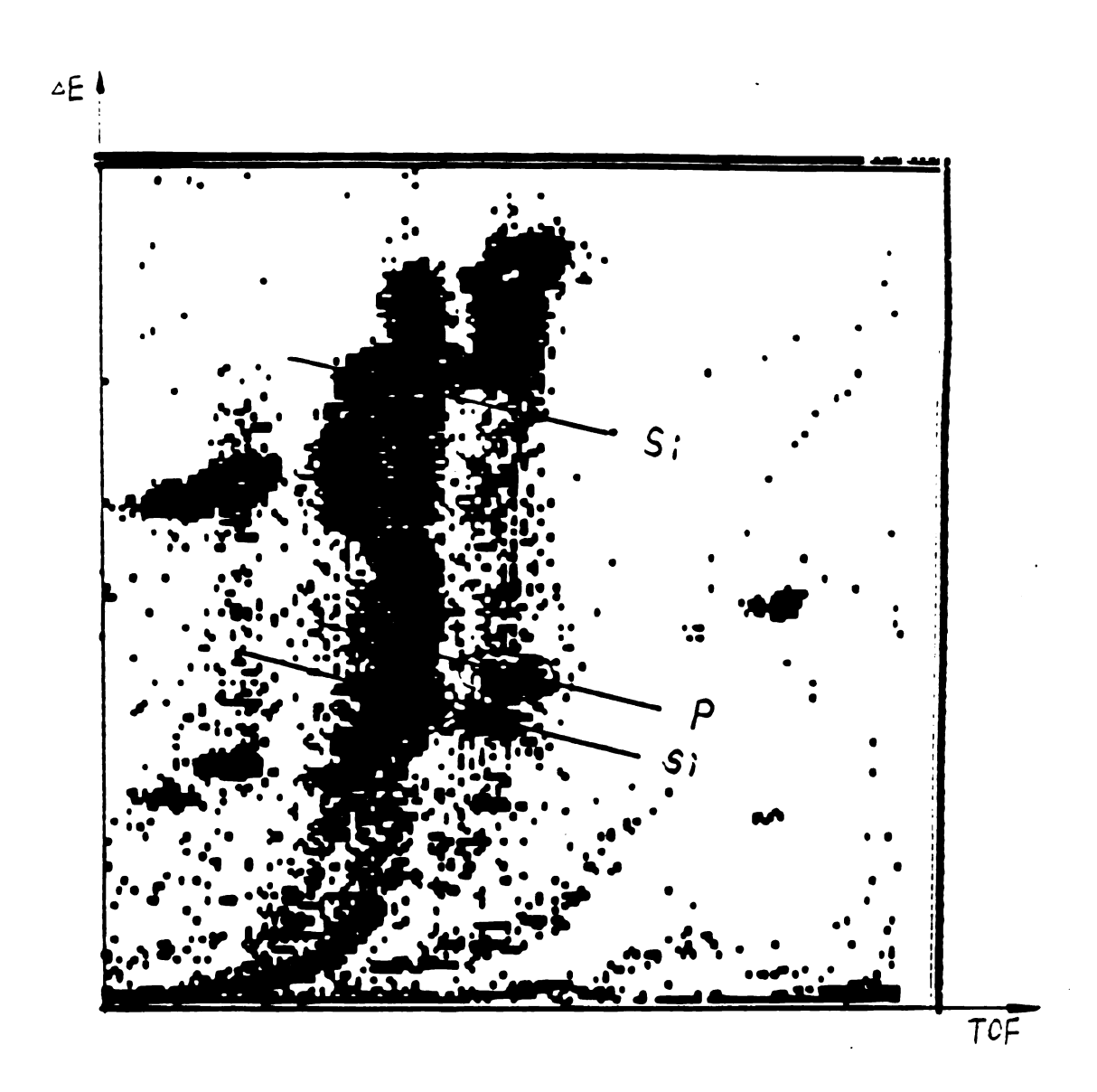


Figure 4.1: The energy deposition of particles in the stopping detector v.s. the time-of-flight of the particles. The groups with higher energy depositions are those particles that were stopped in the detector the groups with lower energies are those particles that penetrated the stopping detectors

isotope, the ratio of the number of nuclei in the low energy group to that of the high energy group, is the transmission efficiency of the mesh. The transmission efficiency obtained this way was 10  $\% \pm 1$  %. To confirm this interpretation of the data, we did a simulation of the energy loss in the detector. Using the  $B\rho$  value of the second half of the A1200, and assuming a momentum acceptance of 3 %, the simulated energy spectrum due to the energy loss of <sup>32</sup>Si is shown in figure 4.2. The corresponding energy spectrum of <sup>32</sup>Si measured in the experiment is shown in figure 4.3. Clearly, there are some major differences between the simulated spectrum and the measured one. First the energy spread of the <sup>32</sup>Si nuclei stopped in the stopping detector in the simulation is much wider than the measured width, and second the transmission efficiency of the mesh from simulation is about 8 % instead of 10 % obtained in the experiment. As mentioned in chapter 3, the momentum acceptance of the A1200 was set at 3 %. The energy loss in the mesh and the absorber foil slow down the nuclei and increases the energy spread. The relative width of the total energy should therefore increase after the mesh and absorber, so that the measured 6 % energy spread is too small. At first, we assumed the measured 6 % energy width was correct, and that the 3 % momentum acceptance was not accurate. A calculation was made to see what kind of momentum spread initially would give that result, and that gave an initial momentum spread of 0.3 % instead of 3 %. It is also possible that, since the optimal  $B\rho$  setting of the A1200 for <sup>32</sup>Si was very close to a charge state (+17Ar) of the beam, and that due to the count rate limit of the monitor, we had to change the B $\rho$  setting by 2 % from the optimal setting. This reduced the momentum width <sup>32</sup>Si nuclei collected, and also required the absorber foil to be changed to insure the implantation in the stopping foil would be centered. Both of these effects seem unlikely sources of the discrepancy in the energy spectrum. The energy loss spectrum of the <sup>32</sup>Si measured at the focal plane using a PIN diode Si detector is given in figure 4.4, and shows a 6 %

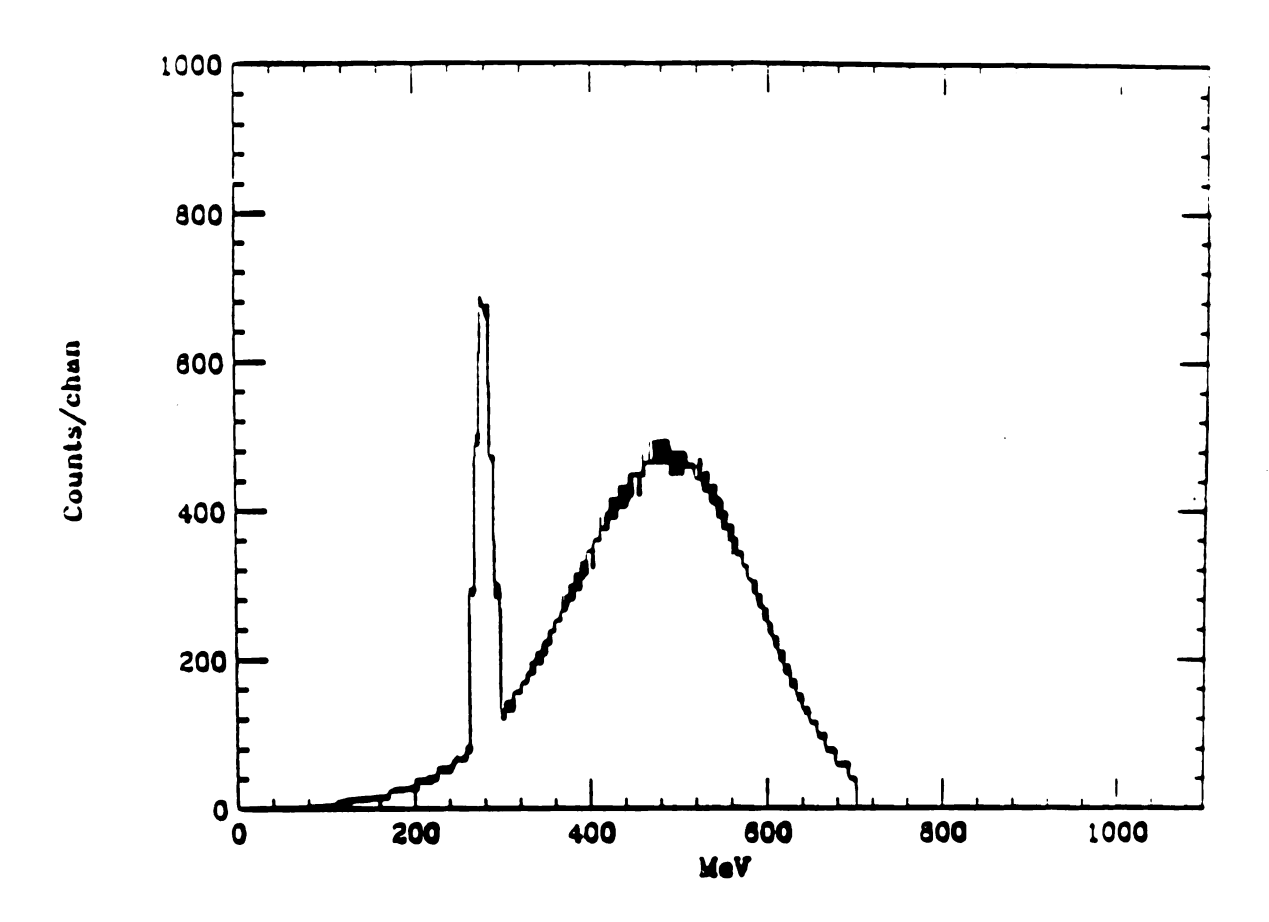


Figure 4.2: Simulated energy deposition of <sup>32</sup>Si nuclei in the stopping detector

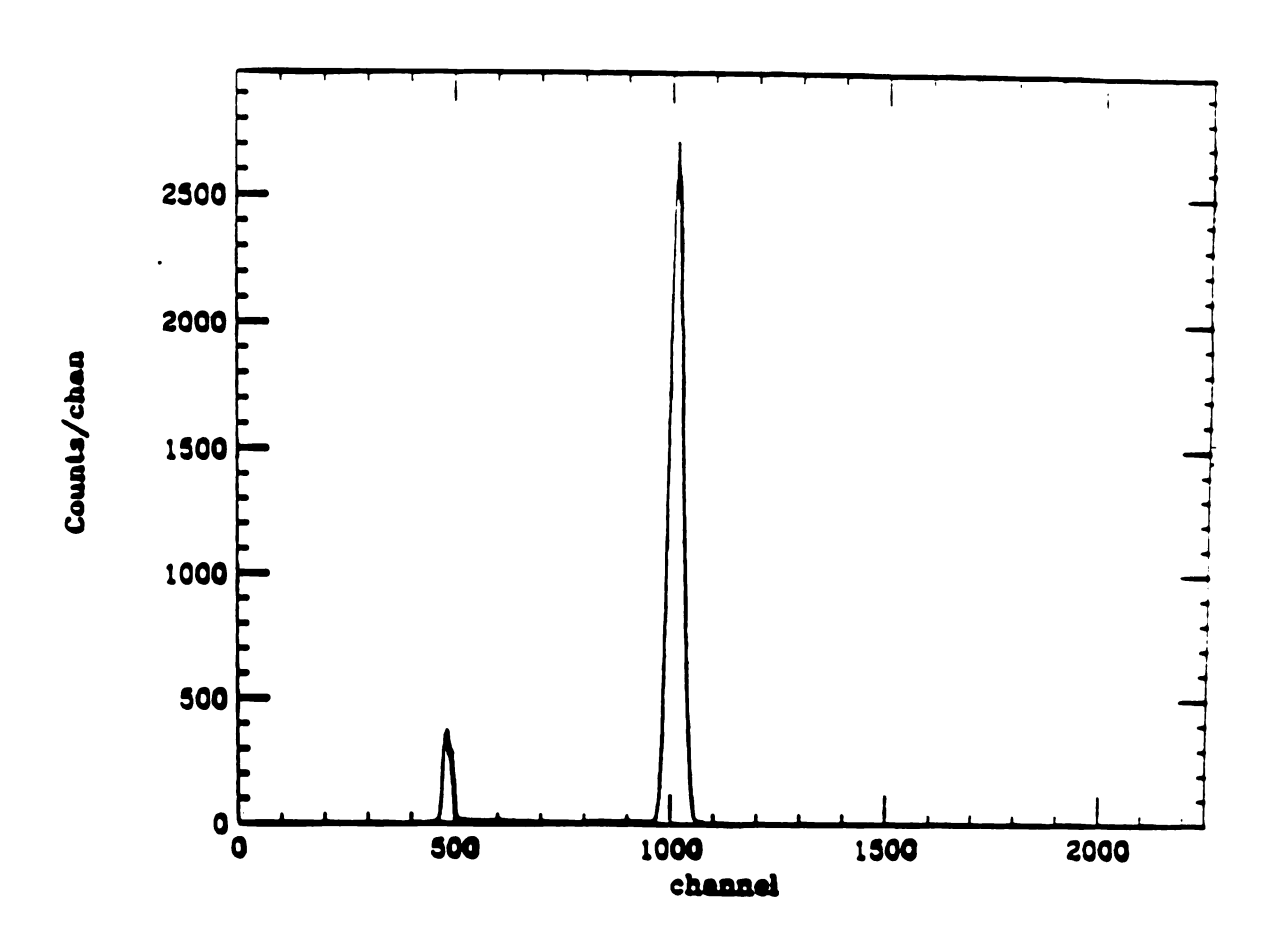


Figure 4.3: measured energy deposition of <sup>32</sup>Si nuclei in the stopping detector

spread of energy loss of <sup>32</sup>Si nuclei in agreement with the 3 % momentum acceptance of the A1200. The most likely possibility is that of electronic saturation, although some unknown problems of the A1200 during the implantation can not be ruled out. The difference between the calculated and measured transmission efficiency may be due to the small size of the holes in the mesh. Due to the limited count rate at which the monitor is able to function properly, the transmission efficiency of the mesh had to be made small. To slow down the particles enough for them to be stopped in the stopping detector and foil dictates the thickness of the mesh. Also to guarantee the uniformity of the mesh, the number of the holes must be large. Since the thickness of the mesh ends up being comparable to the diameter of the holes, the tunneling effect of the particles due to non-normal incidence of the particles on the mesh can smear the distinction between those passing through the holes and those which do not and thus introduce some uncertainty.

It was most likely that we had some electronic saturation in the monitor electronics. With this assumption, the number of nuclei of various isotopes implanted could be calculated from the 10 % transmission efficiency measured. To estimate the number of nuclei of an isotope implanted, we also needed the accumulated counts of the nuclei in the monitor during the whole implantation period. If the nuclei were short lived, that total counts had to be corrected for their decay during that period. To correct the decay of the nuclei during the implantation, we set a condition in the PID histogram for each isotope. Then, the number of the nuclei of an isotope detected in the monitor was binned by the arrival time of the particle. In this way, the histograms of counts vs. time for the nuclei of each isotope were generated. Using this histogram, the number of nuclei implanted were then summed and corrected for the decay of the nuclei during implantation. In table 4.1, the calculated number of nuclei

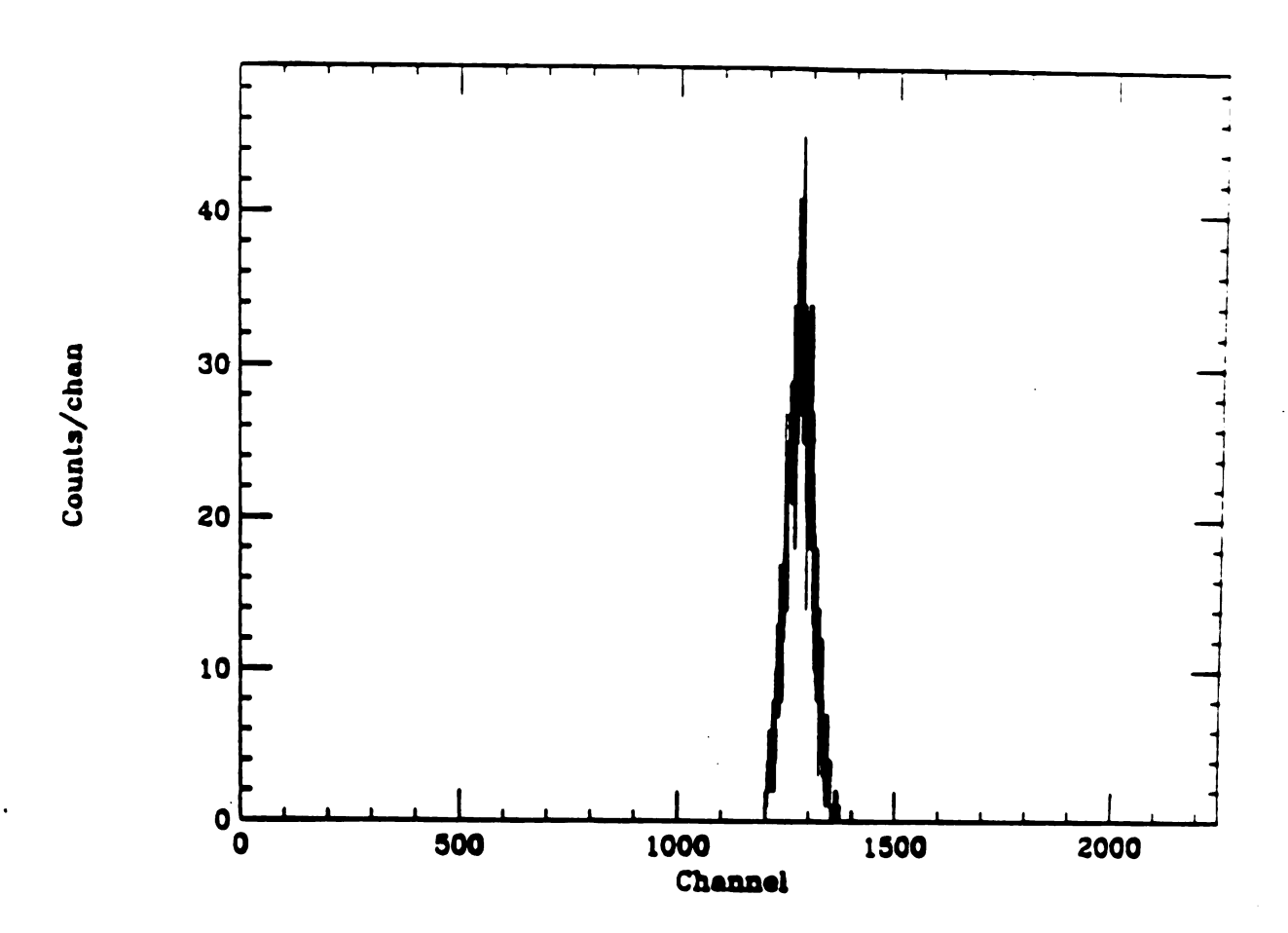


Figure 4.4: Energy loss spectrum of <sup>32</sup>Si nuclei measured by the PIN diode detector

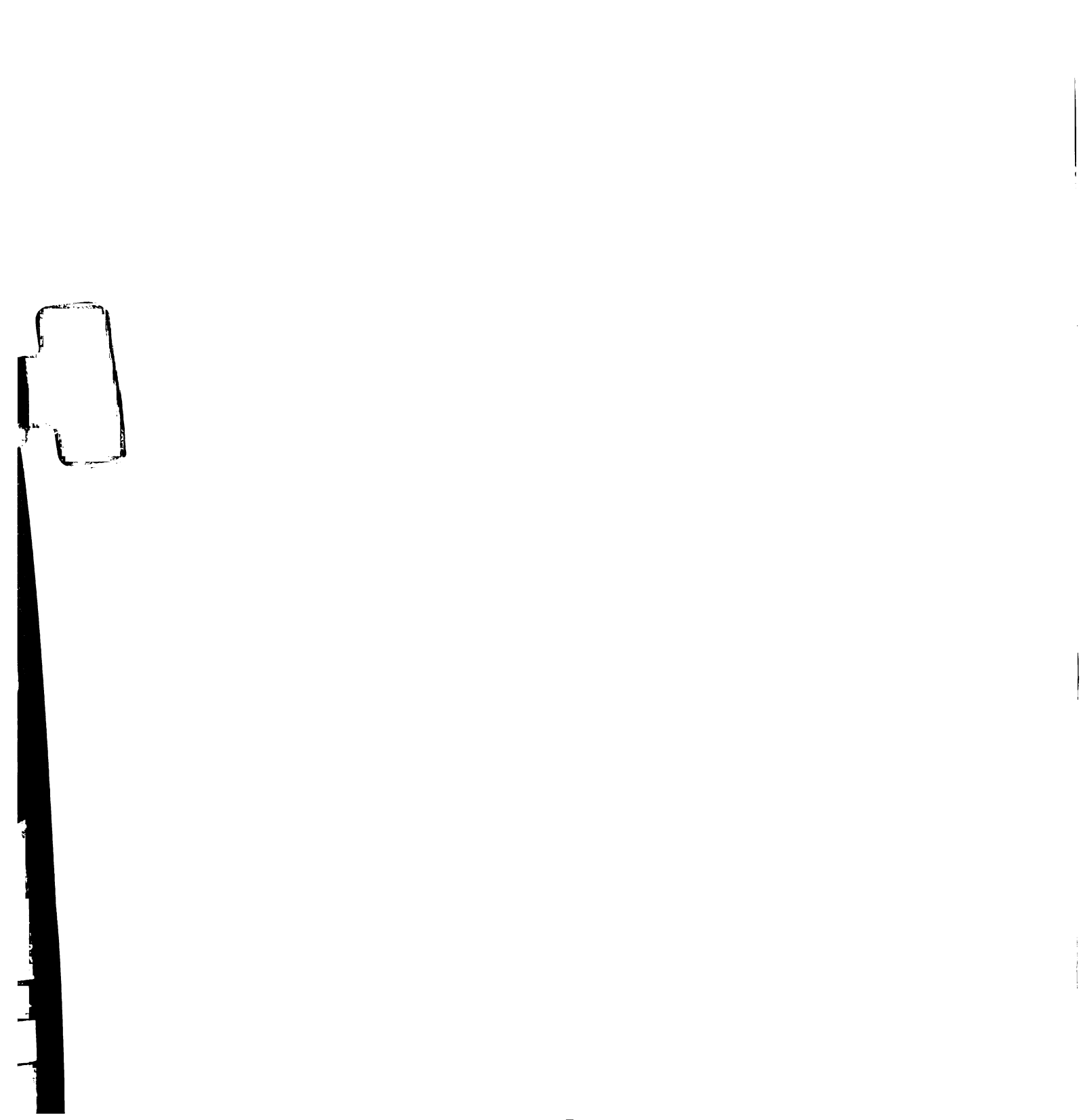
Table 4.1: Number of radioactive nuclei in the sample as 7PM 2/26/91

Nuclei	Number	Uncertainty	Depth L	Depth H	half-life
			$mg/cm^2$	$mg/cm^2$	
<sup>33</sup> P	$5.973 \times 10^7$	7x10 <sup>6</sup>	64.2	138.0	25.3 d
<sup>32</sup> P	$5.80 \times 10^5$	6x10 <sup>6</sup>	64.2	138.0	14.282 d
<sup>31</sup> Si	$4.237 \times 10^6$	6x10 <sup>5</sup>	80.0	157.7	2.62 h
<sup>28</sup> Mg	$3.63 \times 10^{5}$	3.x10 <sup>4</sup>	86.3	165.7	20.90 h
<sup>32</sup> Si	$6.655 \times 10^8$	$6.6 \times 10^7$	55.8	122.7	?

of various isotopes at the start of the activity measurements are summarized. One can see from the table that several short lived isotopes were present in the sample. This is consistent with the measured activity of the sample immediately after the experiment. To determine the efficiency of the counting system, we used the number of nuclei of <sup>31</sup>Si in table 4.1 and the count rate of the sample in the first few hours of the counting.

The center of implantation depth for  $^{31}$ Si nuclei was slightly different from that of the  $^{32}$ Si. To correct for this, the efficiency was obtained from the sum of counting rate of the activity detectors rather than of a single detector (which as will be seen later, corrects the effect). The efficiency of the counting system with a threshold of 100 KeV was determined to be  $0.48 \pm 0.05$ . The reason that  $^{31}$ Si was chosen among those short lived isotopes in table 4.1 was that, 1.) the Q-value of  $^{31}$ Si is 1.48 MeV which is close to the Q-value of  $^{32}$ P, and 2.) due to its short half-life(2.6 hours) and relatively large numbers at the beginning of the counting, its decay accounted for 90 % of all the activity of the sample in the first hour of counting.

In figure 4.5, the calculated number of the nuclei of various isotopes is plotted against time, and in figure 4.6, the predicted decay rates of those nuclei vs. time are

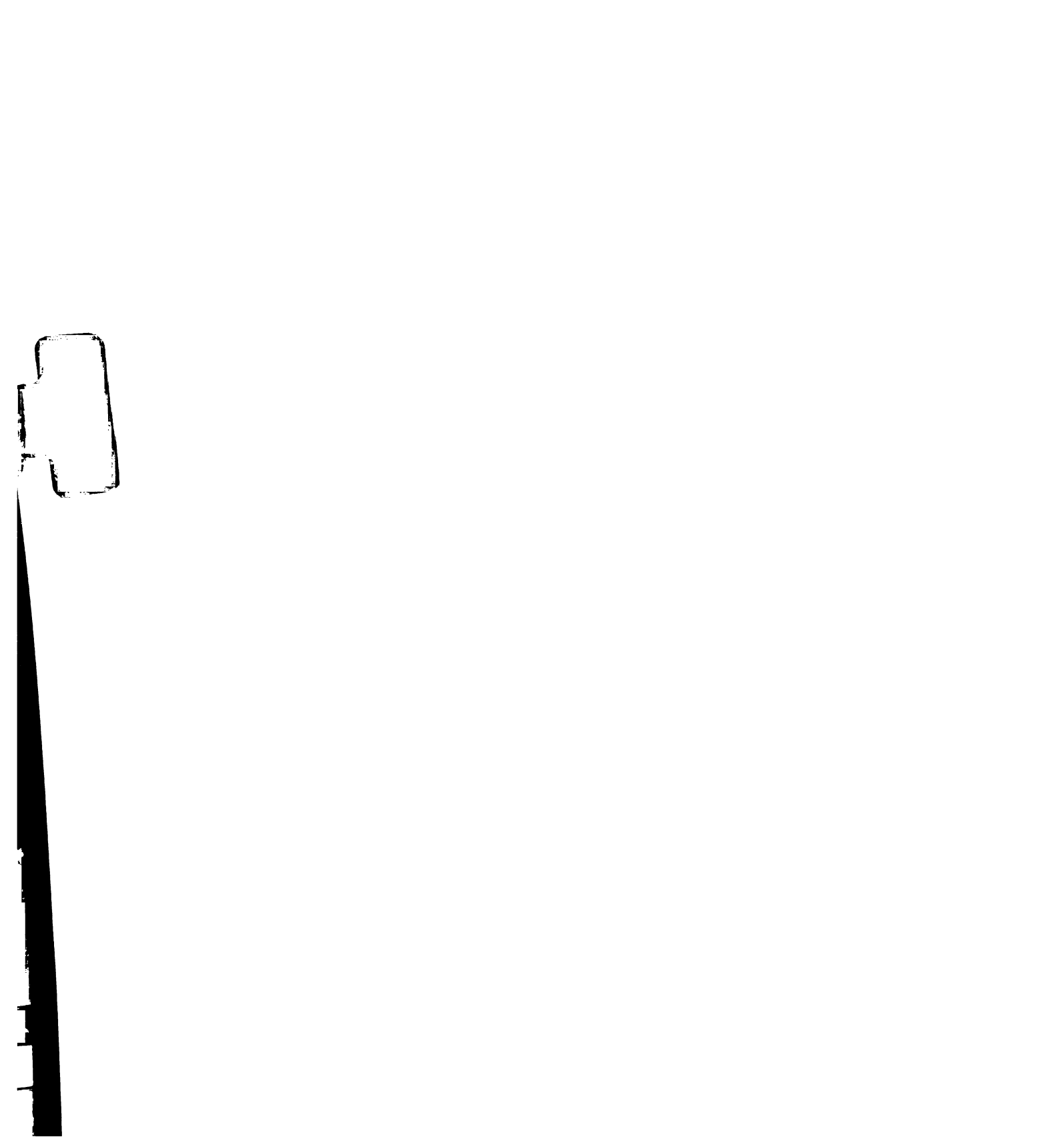


shown. In an attempt to obtain a more reliable estimate of the efficiency of the system, a simulation of energy deposited by electrons in the detectors was made. The resulting energy spectrum of the electrons is shown in figure 4.7. It can be compared with the measured spectrum shown in figure 4.8, While the position of the peak of the spectrum is in good agreement, one can see a considerable discrepancy at higher energies in the spectrum. Thus the empirical evaluation of the efficiency using <sup>31</sup>Si decay was used.

From figure 4.5 and 4.6, we can see that most of the short lived nuclei decayed down to insignificant level 60 days after the experiment. However the decay chain of  $^{32}\text{Si} \rightarrow ^{32}\text{P} \rightarrow ^{32}\text{S}$  does not reach equilibrium(98 %) until about 80 days after the experiment. From counting measurements after 80 days, we obtained the count rate from the decay of  $^{32}\text{Si}$ , with the setting of the threshold above 100 KeV and the background subtracted. From the number of  $^{32}\text{Si}$  nuclei implanted (table 4.1), the efficiency of the counting system, and the measured decay rate of the sample, the half-life of  $^{32}\text{Si}$  was determined to be  $128 \pm 19$  years. The uncertainty of about 15 % is mostly due to the uncertainty in the transmission efficiency of the mesh.

#### 2. Implantation experiment 2

To improve the measurement above, we did second implantation experiment. This time, we tried to eliminate the problems of the mesh and monitor system by using a new feature of the A1200, ie, the target monitor counters described in the last chapter. They monitor the beam intensity during the experiment by counting scattered particles inside the target chamber. The number of <sup>32</sup>Si nuclei produced and implanted in the stack for a fixed A1200 setting during a period of experiment is proportional to the integrated beam current, which in turn is proportional to the total



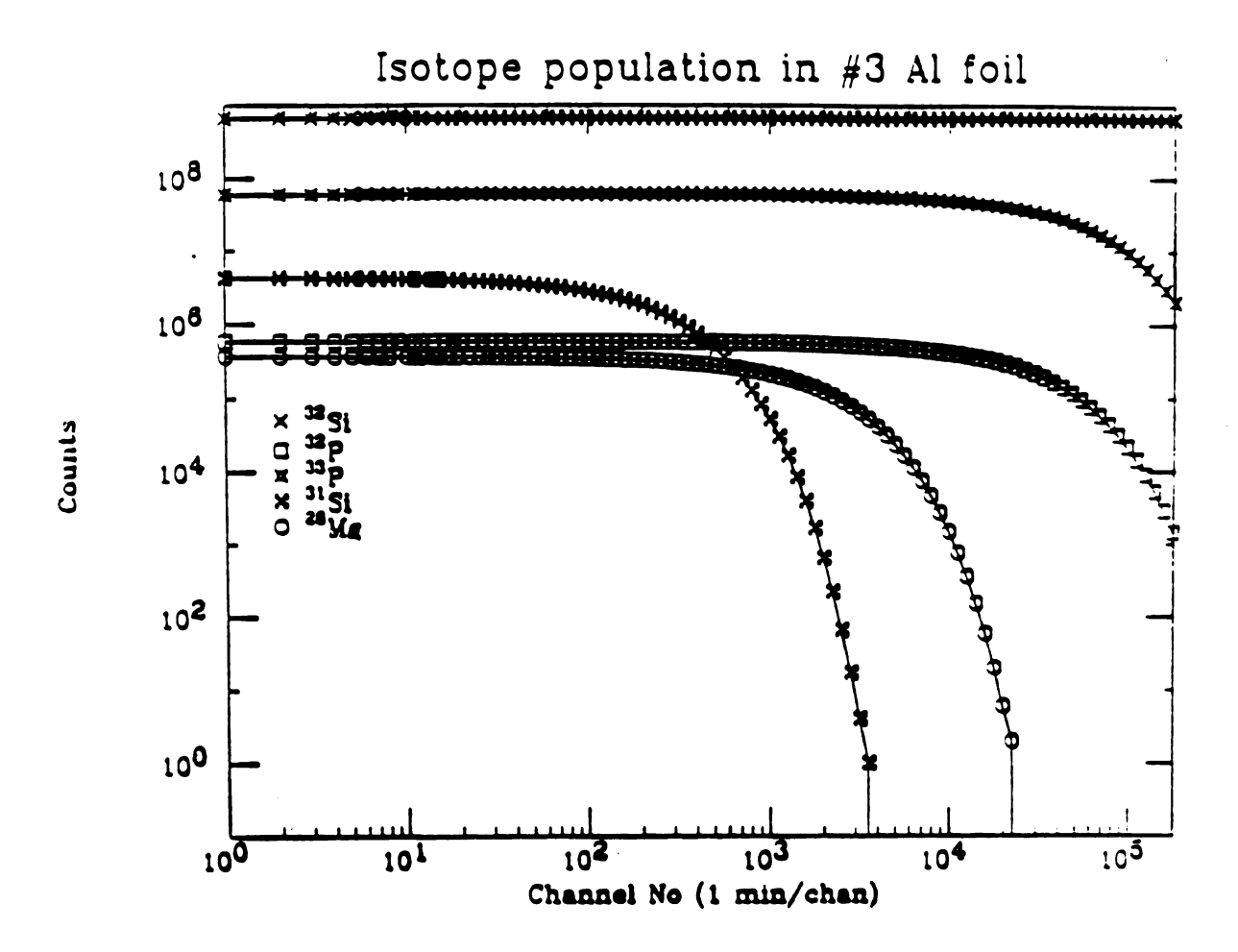


Figure 4.5: Number of the nuclei of various isotopes in the sample as a function of time (calculated according to the number in table 4.1)

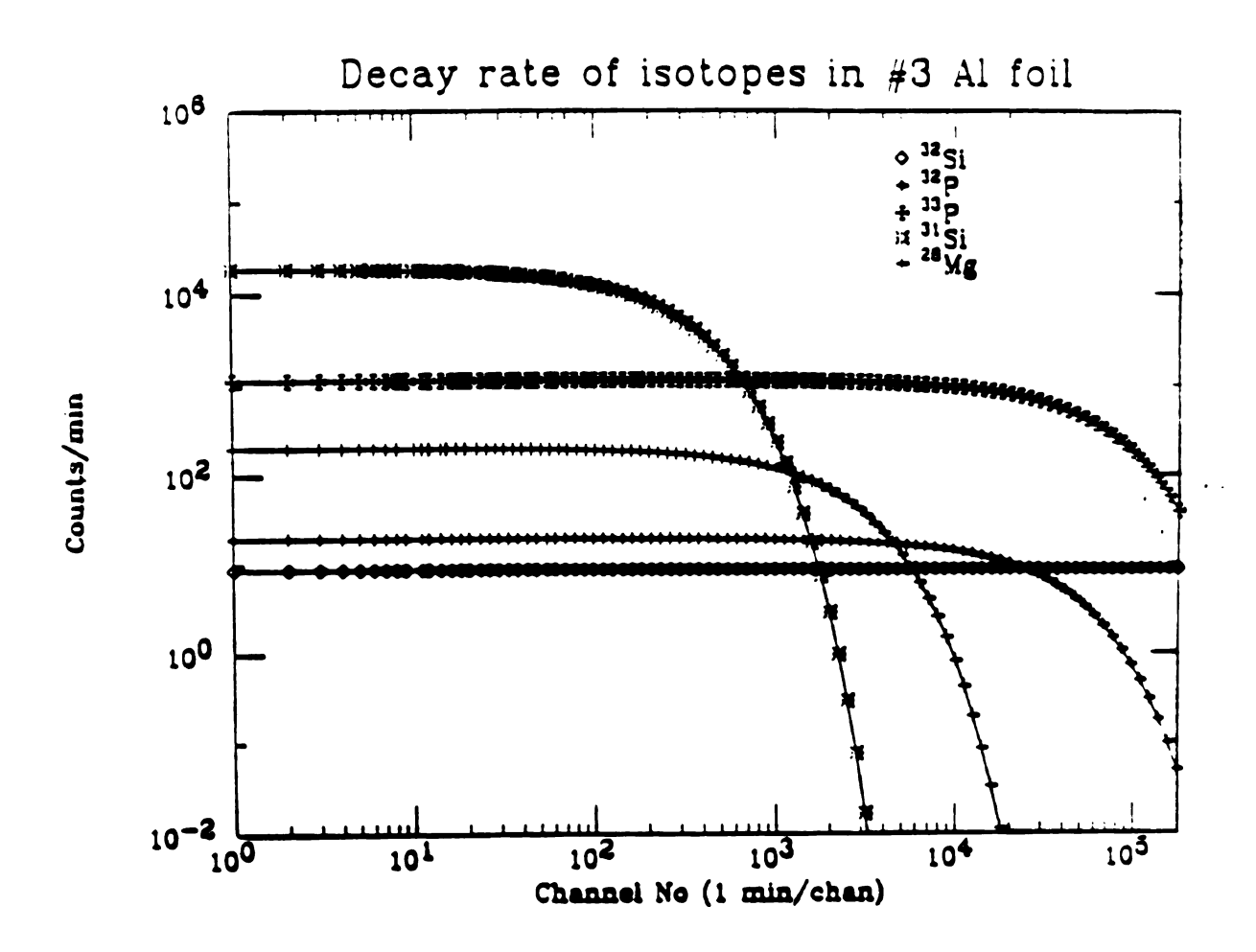


Figure 4.6: Decay rate of the nuclei of various isotopes in the sample as a function of time. (calculated according to the number in table 4.1.)

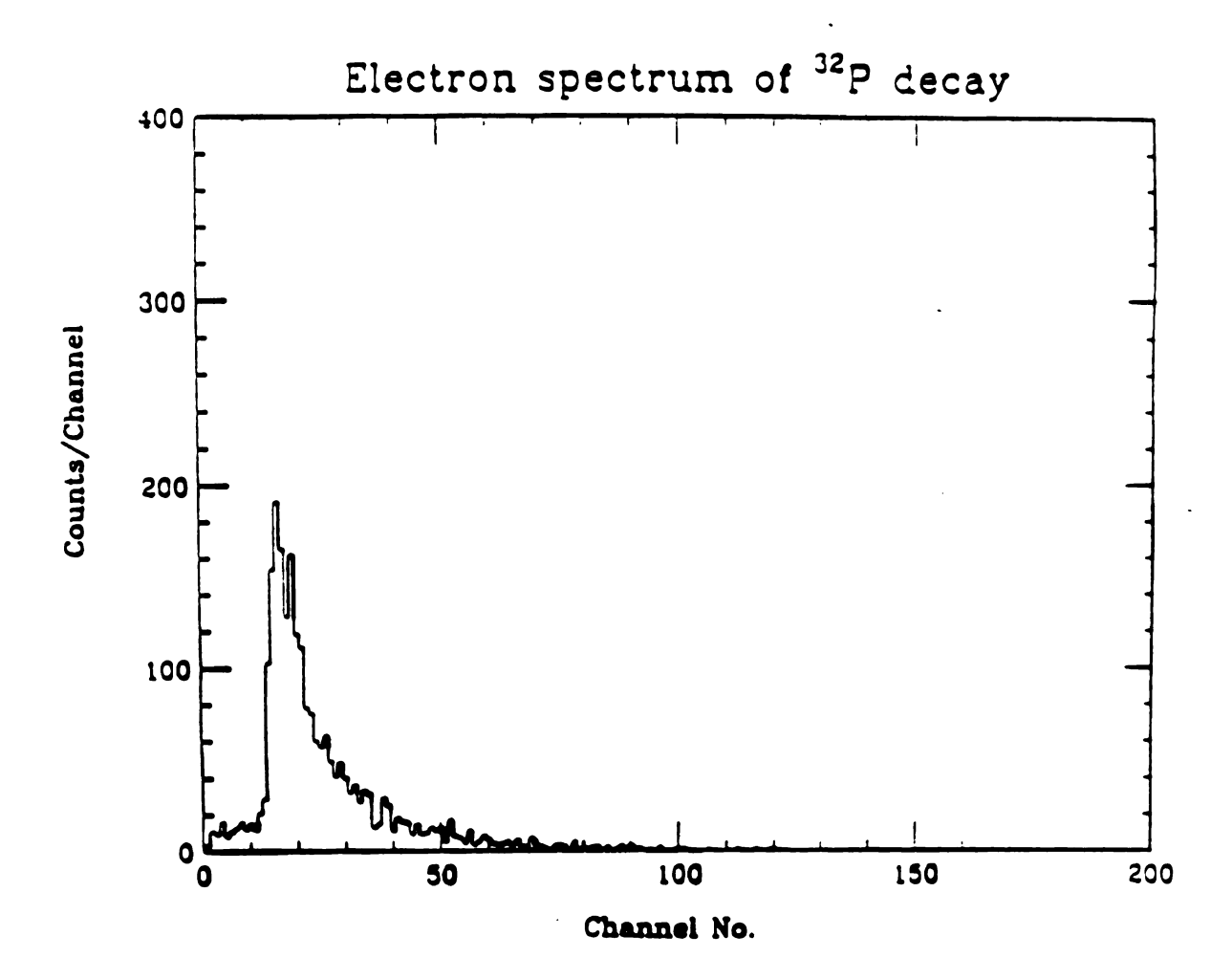


Figure 4.7: Simulated energy loss (in the activity counter) spectrum of electrons from the decay of <sup>32</sup>P.

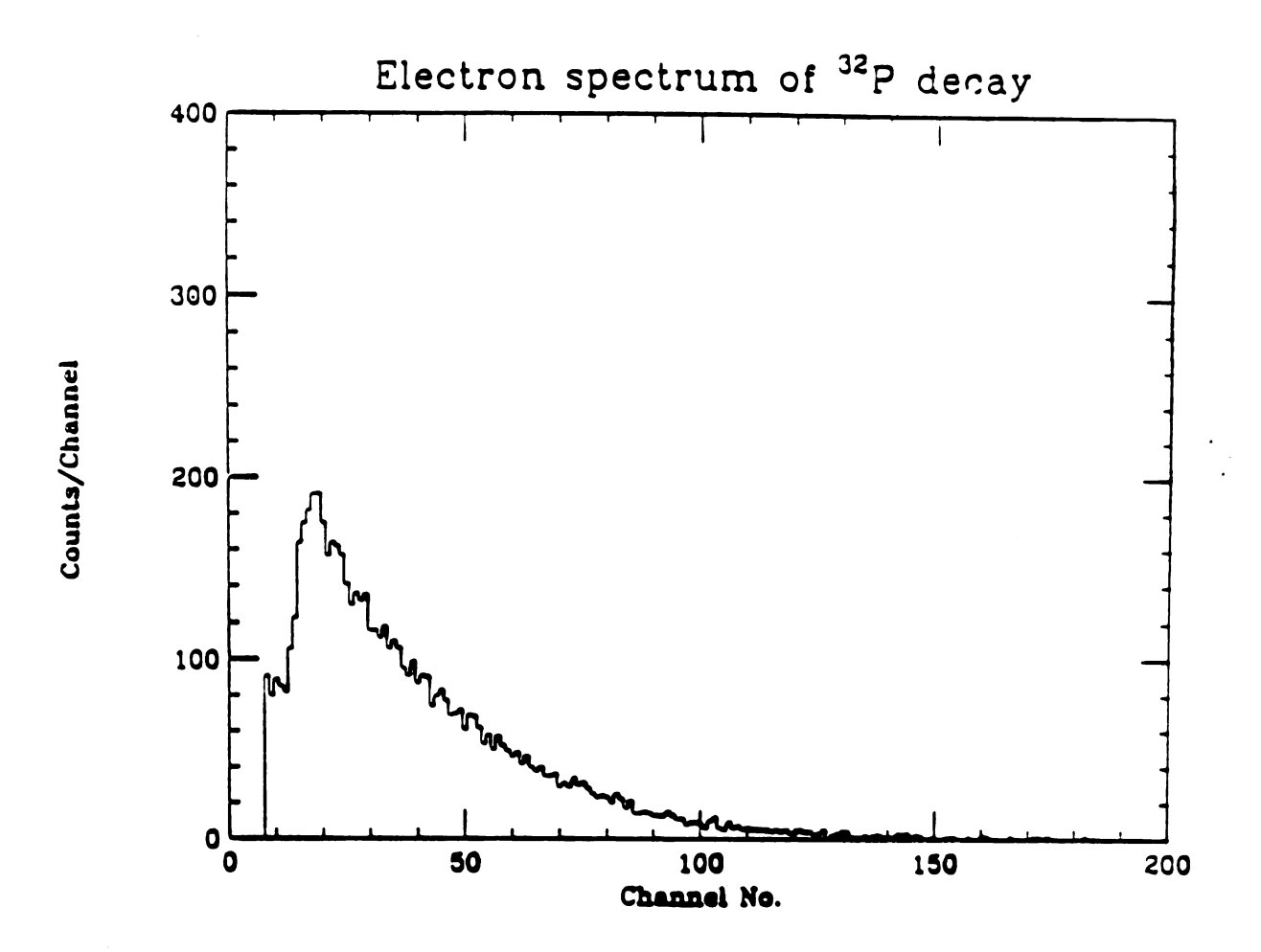
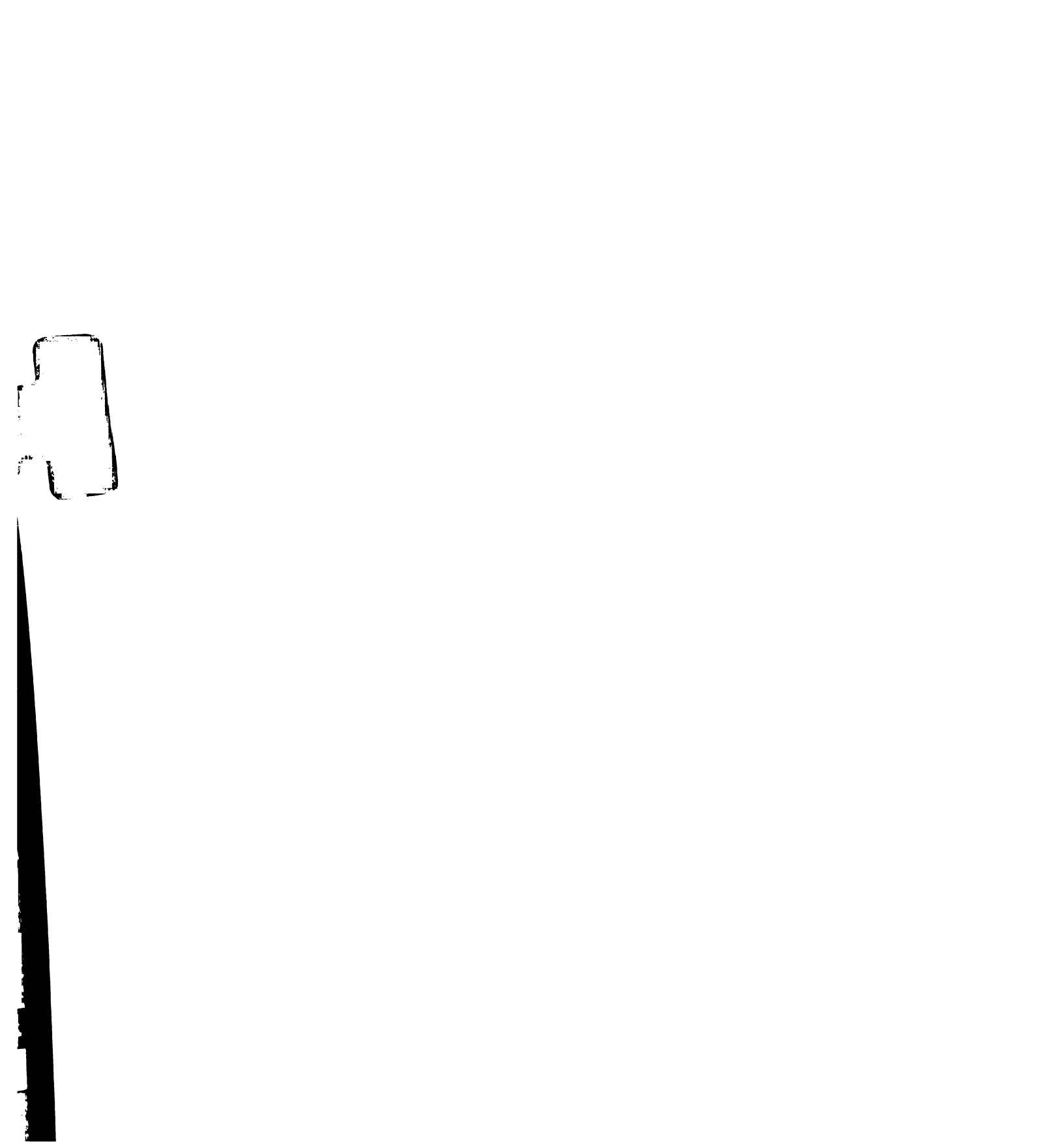


Figure 4.8: measured energy loss (by detector 1) spectrum of electrons from the decay of <sup>32</sup>P source (subtract background)



number of counts registered by the target monitor counters during the same period. By operating with a reduced beam intensity, and by replacing the implantation foil at the focal plane with a Si detector, we could measure the ratio of the number of <sup>32</sup>Si nuclei produced during a period of time to the sum of total counts from all the monitor counters in the same period of time. This ratio, multiplied by the sum of total counts in all four monitors during an implantation run at higher beam intensity, gives the number of <sup>32</sup>Si nuclei implanted during that run. To ensure that the ratio defined above does not change with time, the implantation of <sup>32</sup>Si nuclei was done as a series of 14 short runs, each lasting 1-2 hours. And as described in chapter 3, immediately before and after each implantation, the Si detector stack was put at the focal plane to measure the ratio again. The average of the two ratios measured before and after each run was used to calculate the number of <sup>32</sup>Si nuclei implanted, and the uncertainties due to the variation of this ratio from measurement to measurement were also evaluated in the same process. In table 4.2, the number of nuclei of various isotopes implanted and their uncertainties are summarized.

Once the number of  $^{32}$ Si nuclei implanted is determined, the other part of the procedures to get the half-life of the  $^{32}$ Si which differs from the first experiment lies in the efficiency of the counting system. Since the sample thickness was changed from last time, the previous counting efficiency could not be used. To obtain the efficiency of the counting system, we monitored the activity of the two  $^{32}$ P samples until their count rate approached that of the background. One problem in using the  $^{32}$ P samples for efficiency calibration was that the  $^{32}$ P nuclei were implanted closer to one surface of the sample(about 30 mg/cm<sup>2</sup> off the center). This was largely due to the fact that the calculated optimal B $\rho$  settings were not the same as the experimental ones, and the real B $\rho$  settings for implantation were adjusted and fine tuned during

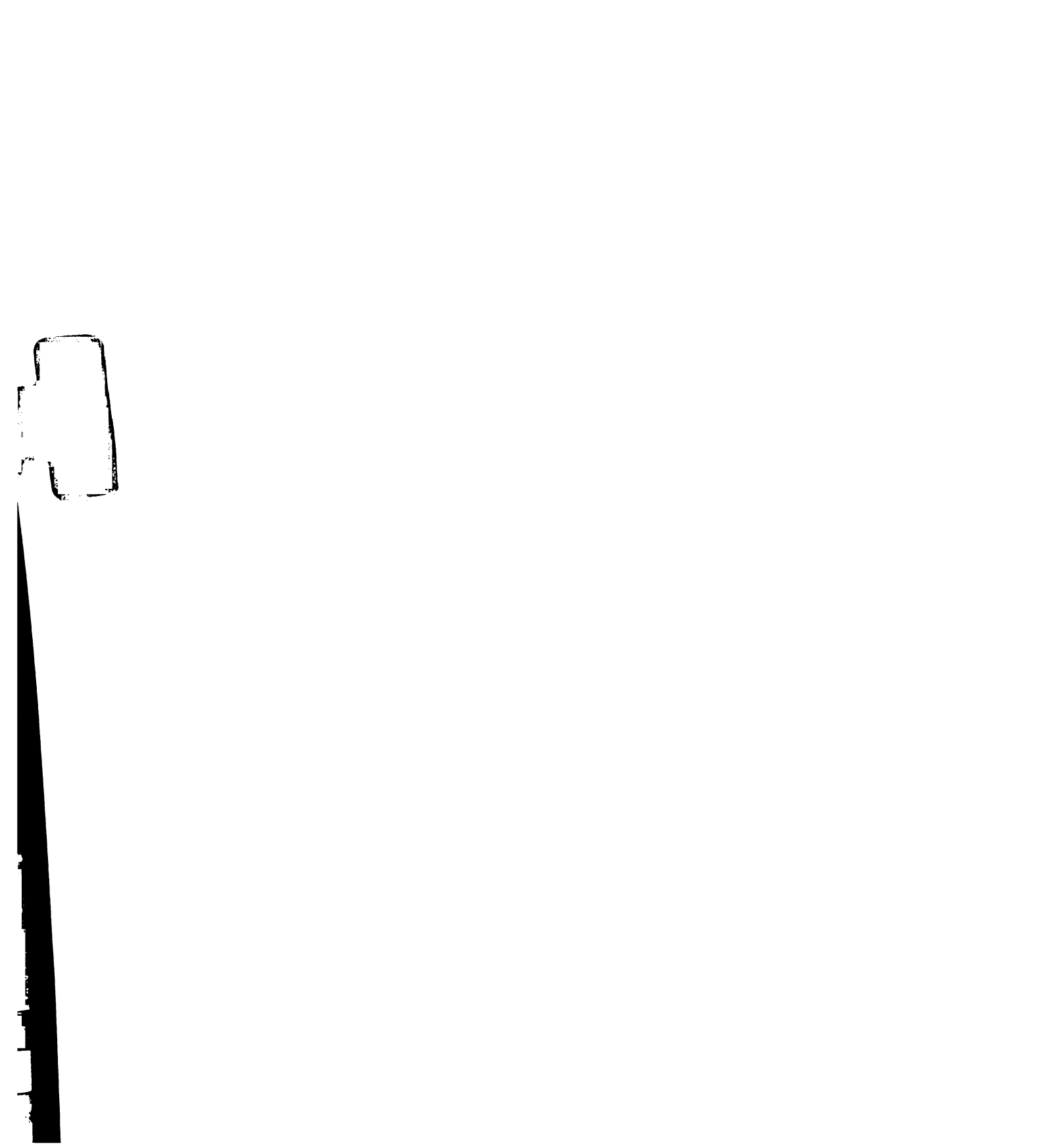


Table 4.2: Number of nuclei of various isotopes implanted in the samples.

## a.) Number of nuclei of various isotopes implanted sample P1

Nuclei	Number	Uncertainty	Depth L mg/cm <sup>2</sup>	Depth H mg/cm <sup>2</sup>	halflife
<sup>33</sup> S	$8.93 \times 10^{5}$	4.3x10 <sup>4</sup>	163.4	182.6	Stable
<sup>31</sup> Si	$1.686 \times 10^{5}$	$8.8 \times 10^3$	129.3	145.7	2.622 h
<sup>30</sup> Si	$3.57 \times 10^{5}$	1.3x10 <sup>4</sup>	147.7	165.7	Stable
<sup>29</sup> Al	1.563×10 <sup>6</sup>	7.3x10 <sup>4</sup>	141.0	158.5	6.6 m
<sup>28</sup> Mg	1.858×10 <sup>5</sup>	$8.2 \times 10^3$	133.2	141.6	20.90 h
<sup>32</sup> P	8.82x10 <sup>6</sup>	4.1x10 <sup>5</sup>	135.3	152.1	14.282 d

## b.) Number of nuclei of various isotopes implanted sample P2

Nuclei	Number	Uncertainty	Depth L	Depth H	halflife
			$mg/cm^2$	$mg/cm^2$	
33S	1.0613x10 <sup>6</sup>	5.6x10 <sup>4</sup>	153.9	192.2	Stable
<sup>31</sup> Si	$1.3089 \times 10^{5}$	$7.4 \times 10^3$	121.2	154.1	2.622 h
<sup>30</sup> Si	$1.009 \times 10^{6}$	5.8x10 <sup>4</sup>	139.1	174.9	Stable
<sup>29</sup> Al	1.942x10 <sup>6</sup>	$1.1 \times 10^{5}$	132.7	167.3	6.6 m
<sup>28</sup> Mg	1.68×10 <sup>5</sup>	1.8x10 <sup>4</sup>	125.0	157.5	20.90 h
<sup>32</sup> P	$8.95 \times 10^{6}$	3.8×10 <sup>5</sup>	127.1	160.9	14.282 d

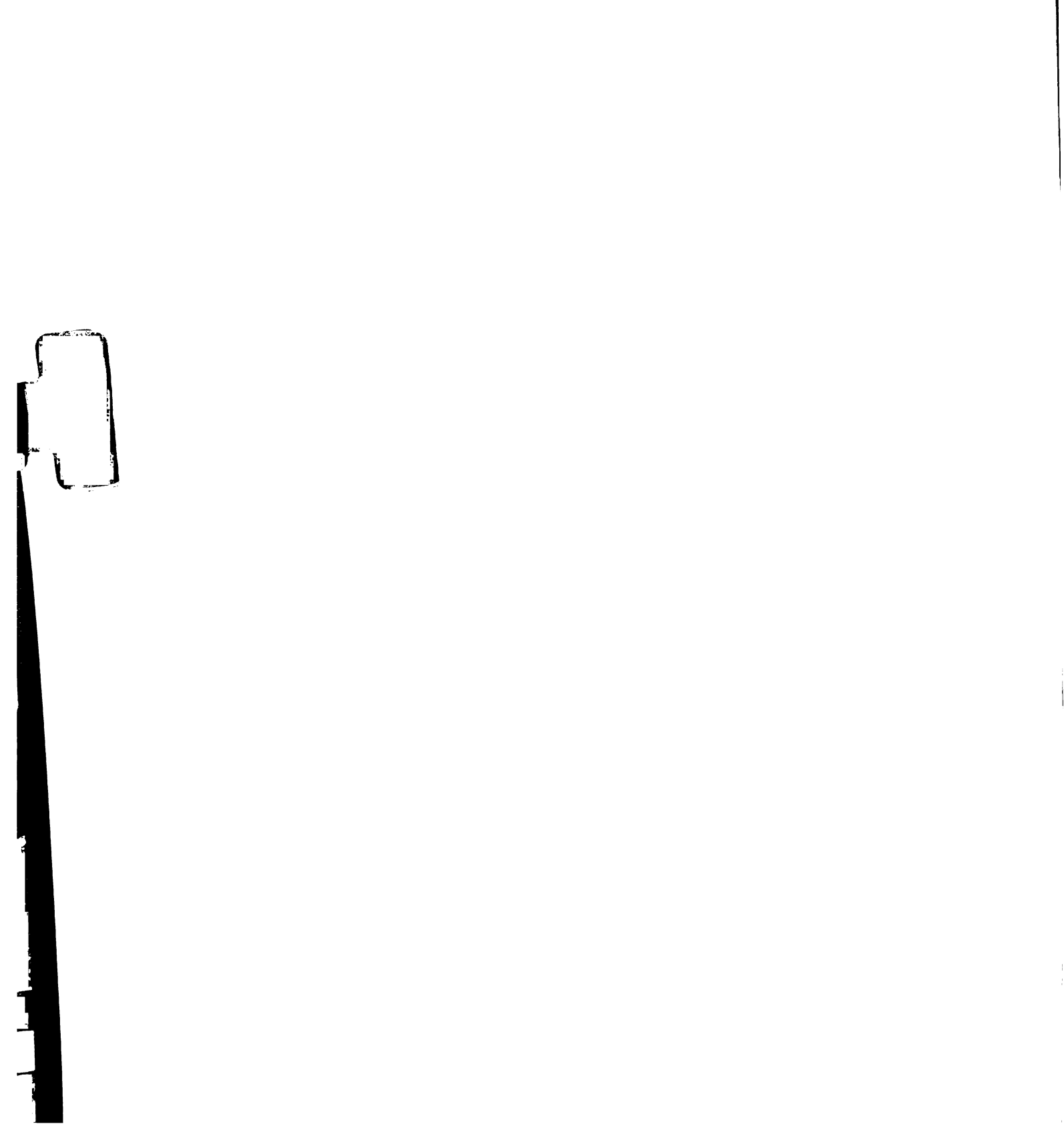
## c.) Number of nuclei of various isotopes implanted sample Si

Nuclei	Number	Uncertainty	Depth L mg/cm <sup>2</sup>	Depth H mg/cm <sup>2</sup>	halflife
33P	5.466×10 <sup>8</sup>	2.7x10 <sup>7</sup>	64.2	138.0	25.3 d
31Si	1.095×10 <sup>8</sup>	6.1x10 <sup>7</sup>	80.0	157.7	2.62 h
<sup>30</sup> Al	2.759x10 <sup>8</sup>	1.7x10 <sup>7</sup>	70.3	145.8	3.68 s
28 Mg	1.68×10 <sup>7</sup>	3.8x10 <sup>6</sup>	86.3	165.7	20.90 h
<sup>29</sup> Mg	2.37×10 <sup>7</sup>	3.6x10 <sup>6</sup>	59.0	131.6	1.1 s
<sup>27</sup> Na	5.51x10 <sup>6</sup>	$3.5 \times 10^{5}$	72.9	149.2	304 ms
<sup>32</sup> Si	7.371x10 <sup>8</sup>	3.3x10 <sup>7</sup>	55.8	122.7	?

the experiment. This asymmetry in the depth of implantation caused a count rate difference in the two Si detector in the counting system. In figure 4.9 and 4.10, the count rates of both detectors with various threshold settings for sample P<sub>1</sub> and P<sub>2</sub> are shown. The efficiency of a detector measuring the activity of a sample could be easily calculated by dividing the measured count rate with that of the predicted decay rate of the sample. These decay rates at different times were calculated with the data in table 4.2 and are plotted against time in figure 4.9 and 4.10. However, due to the asymmetry in the depths of the implantation, the efficiencies for a single detector can't be useful for the <sup>32</sup>Si sample.

In figure 4.11, the count rate of <sup>32</sup>Si decay measured by both detectors are plotted against time. One can see that the difference between the count rates measured by two detectors is not as severe as those shown in figure 4.9. This confirms that the center of implantation depth is closer to the middle of the sample than was the case for the <sup>32</sup>P samples.

To resolve this problem of asymmetric implantation, we made several tests. We added some Al foils between sample P<sub>1</sub> and the detector with higher count rate to equalize the count rate of the detectors. The results for 66 mg/cm<sup>2</sup> added Al foil plotted in figure 4.12. We obtained 33 mg/cm<sup>2</sup> (half of what is needed to equalize the count rate) for the error in the implantation depth of <sup>32</sup>P from the center. To obtain additional information about the effects of foil thickness on the count rate, we conducted several tests with a <sup>32</sup>P source. The <sup>32</sup>P source was made of <sup>32</sup>P waste used in biology experiments here on campus, sandwiched between two piece of Al foils each 41 mg/cm<sup>2</sup> thick. The Al foils were cut to have the same shape as the sample, and the <sup>32</sup>P was put at the center of foil with a radius matching the size of the collimator



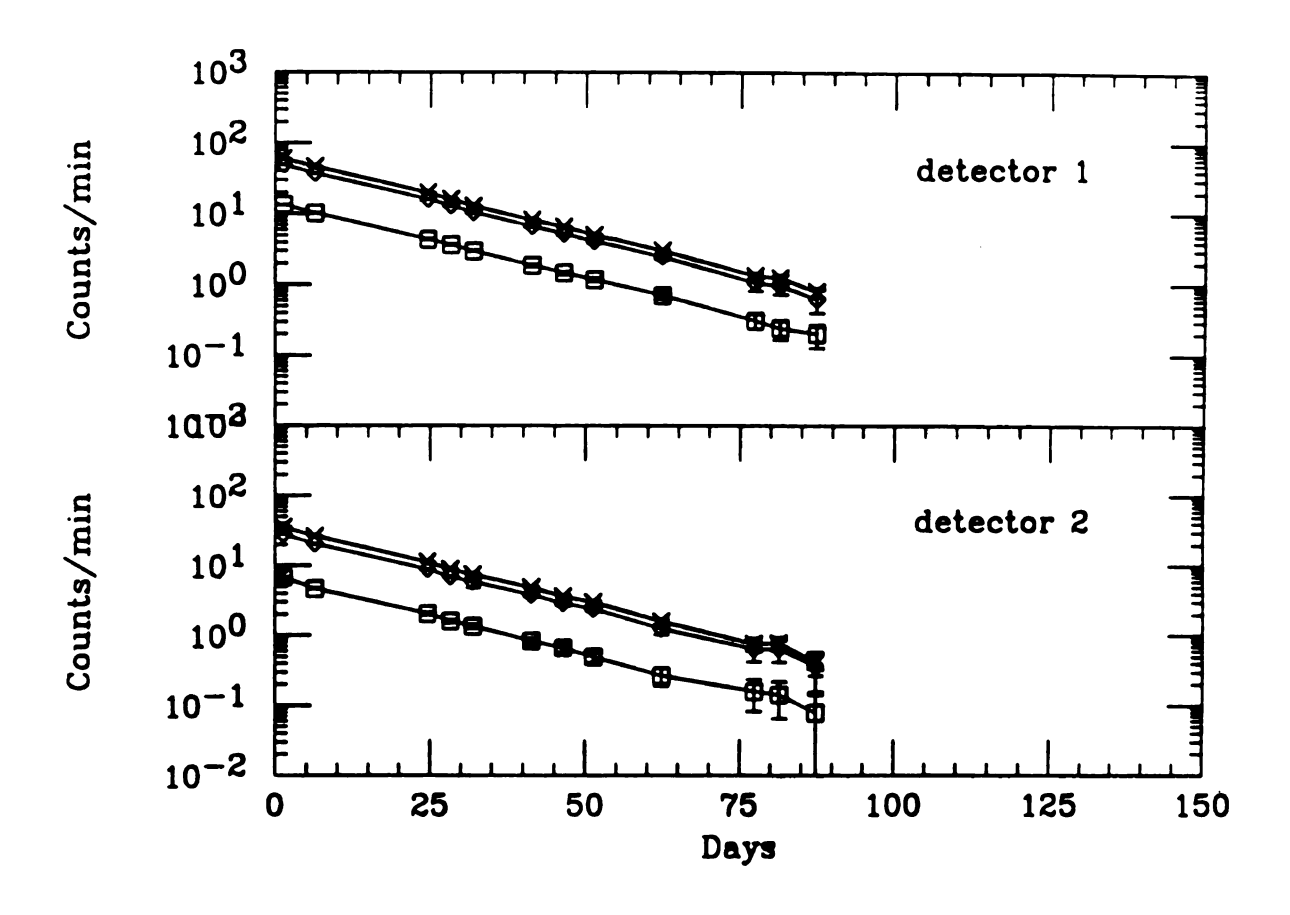


Figure 4.9: The decay rate of <sup>32</sup>P(count rate - background rate) in sample P<sub>1</sub>

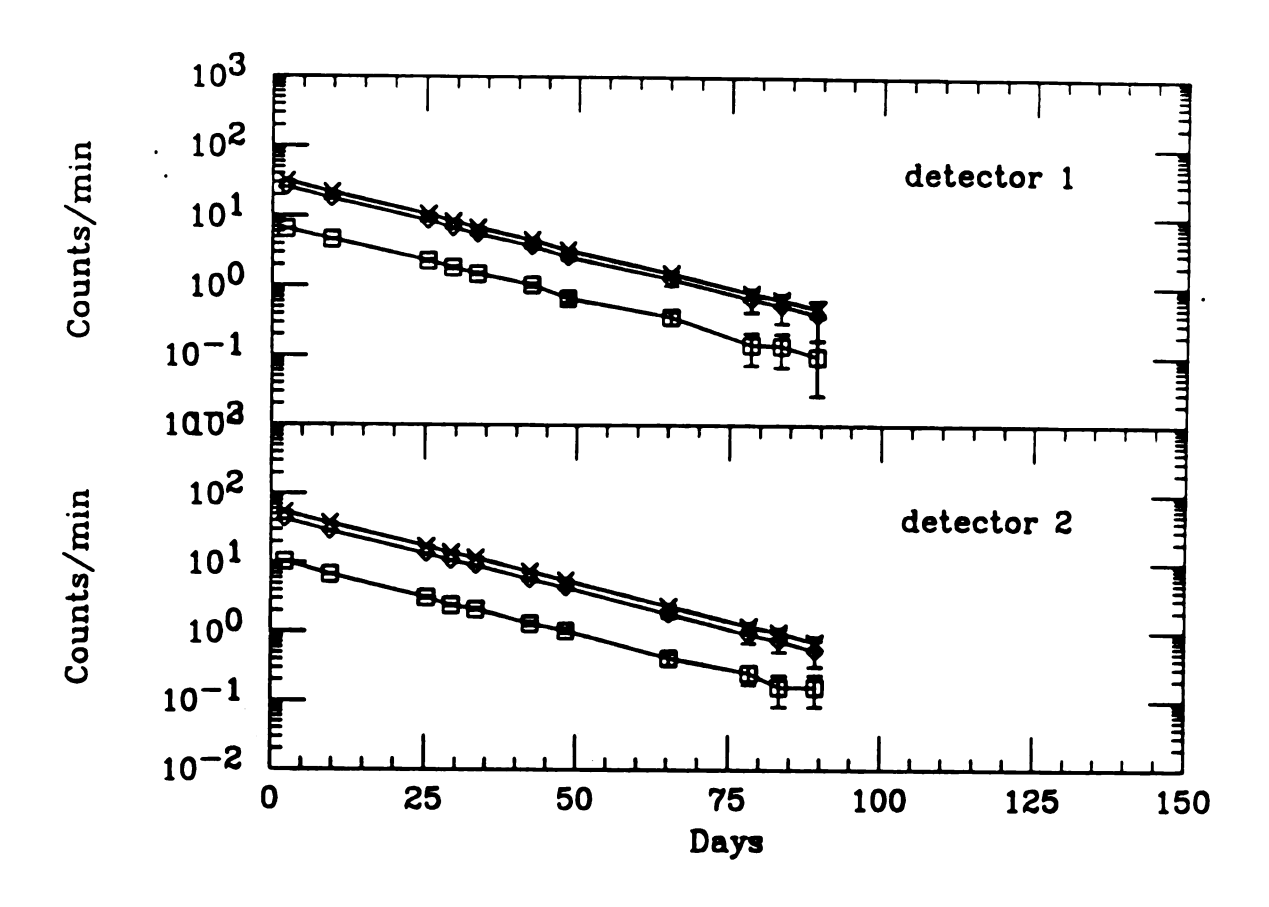


Figure 4.10: The decay rate of <sup>32</sup>P(count rate - background rate) in sample P<sub>2</sub>

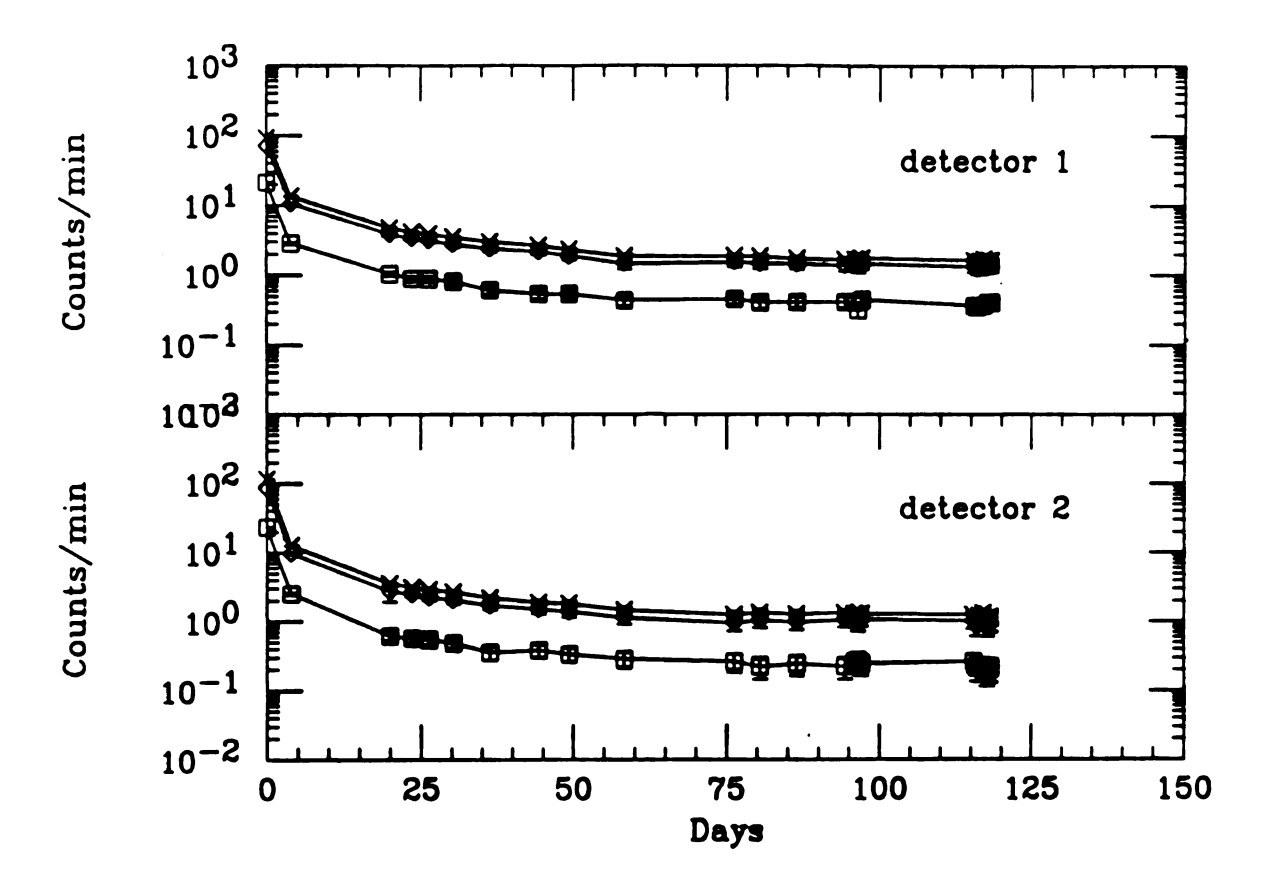


Figure 4.11: The decay rate (count rate - background rate) of sample Si

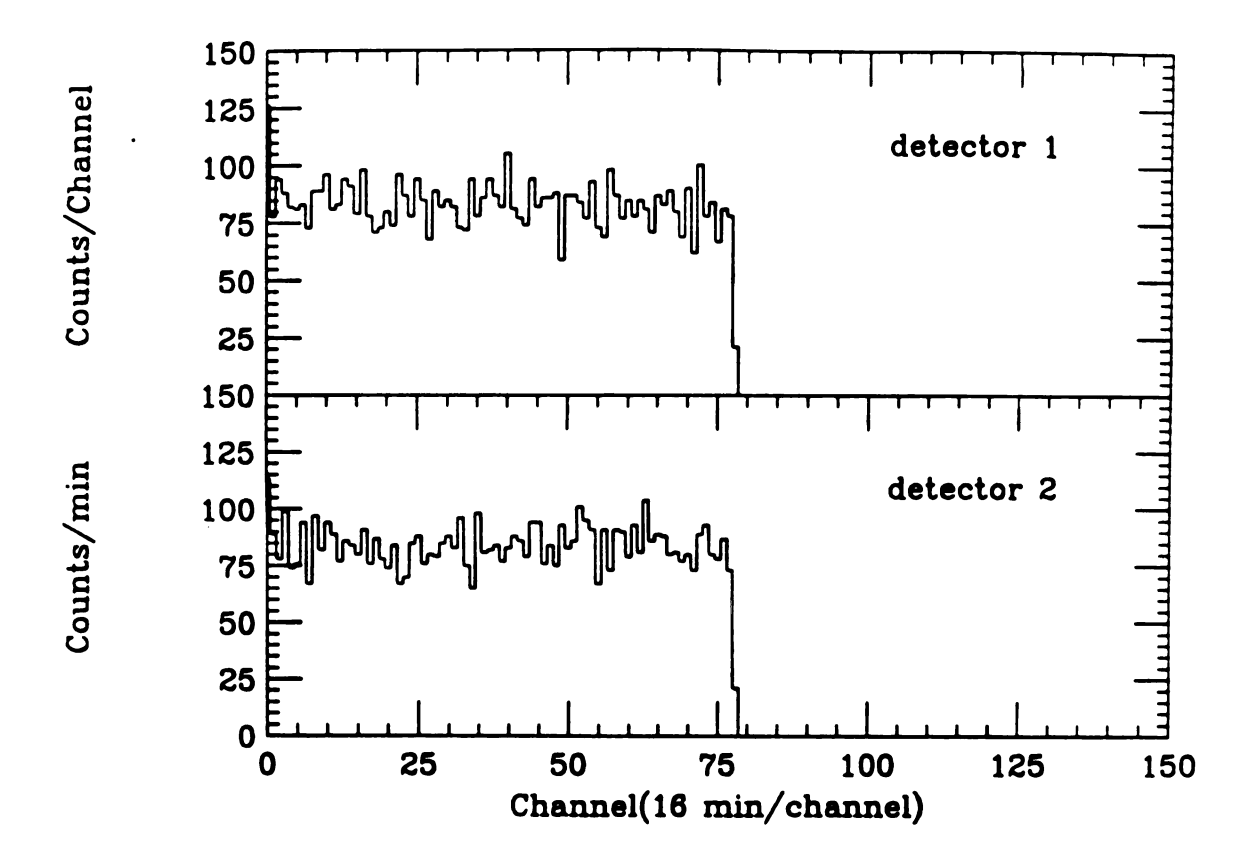


Figure 4.12: The number of events measured by the two counters as a function of time(after Al foils were added to equalize the count rates of the sample P<sub>1</sub> measured by the two detectors)

Table 4.3: The measured count rate of <sup>32</sup>P source

Detector	Above 100 KeV	Above 200 KeV	Above 500 KeV
detector 1	$5.30 \pm 0.08$	4.20±0.07	1.1±0.04
detector 2	$5.32 \pm 0.08$	4.06±0.07	1.0±0.04

placed in front of the stack during implantation. This source was then counted, and the data is summarized in table 4.3.

One can see that the count rates in both detectors are the same within uncertainties. Which justified our assumption that the count rate difference between the two detectors facing different sides of the sample was due to the asymmetry in the implantation depth of <sup>32</sup>P nuclei. More measurements were made with this <sup>32</sup>P source by adding Al foils symmetrically, and asymmetrically, and trying to simulate the experimental structure of the <sup>32</sup>P, and <sup>32</sup>Si samples exactly. The relative efficiency of activity counter for the <sup>32</sup>P source was defined to be the following ratio

$$E_r = \frac{C(t + 41mg/cm^2)}{C(41mg/cm^2)}$$

Where the C(x) is the count rate measured by a detector when Al foils of thickness x mg/cm<sup>2</sup> are added to the bare <sup>32</sup>P source. The numbers used in the above formula are corrected for <sup>32</sup>P decay. In figure 4.13, the value  $E_r$  are plotted against the thickness of the Al foils between the <sup>32</sup>P nuclei and the detectors. One can see that the relative efficiency  $E_r$  decreases almost linearly as the thickness of the Al increases. This indicates that the sum of the count rate of  $\beta$ s in the two detectors is relatively independent of the imprecision in the depth of the implantation.

To confirm this idea, we decided to do a simulation of one of the implanted 32P

Table 4.4: The measured decay rates of the <sup>32</sup>P source with different conditions at different time

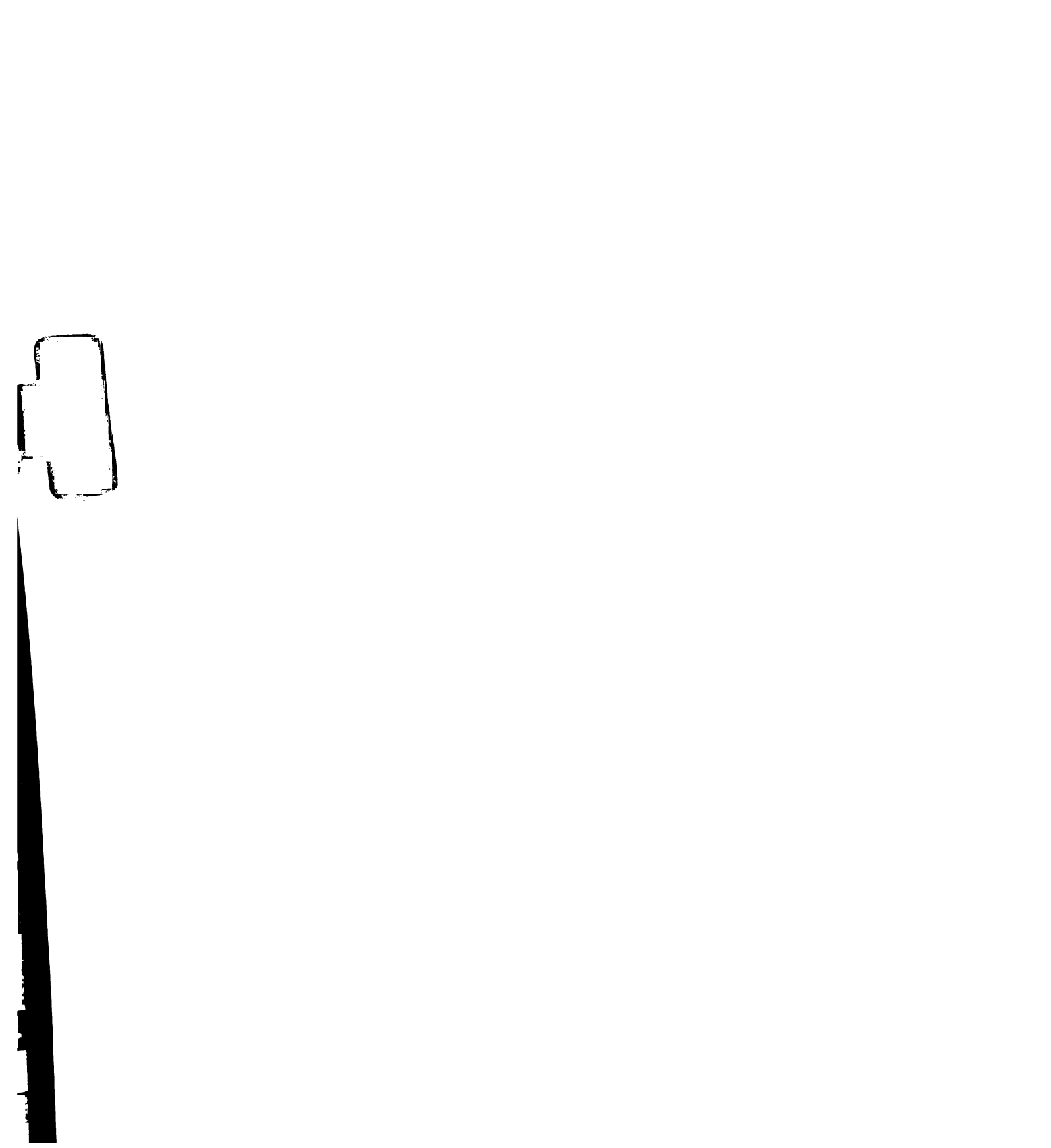
Asymmetry(mg/cm <sup>2</sup> )	Above 100 KeV	Above 200 KeV	Above 500 KeV
0	10.6±0.4	8.6±0.8	2.2±0.3
40	11.1±0.4	9.3±0.8 ·	2.4±0.3
109	10.9±0.4	8.8±0.8	2.3±0.3
-109	11.1±0.4	9.2±0.8	2.4±0.4
-40	11.1±0.4	9.0±0.8	2.3±0.3

samples using Al foils and the source. We first added Al foils symmetrically to both side of the source so that the total thickness of the resulting source was the same as the thickness of the implanted <sup>32</sup>P sample. We call this configuration of the source the 'symmetric' configuration. This source was then counted, and the sum of count rate in the two detectors corrected for the decay of <sup>32</sup>P are given in table 4.4. Other 'asymmetric' configurations were made by adding Al foils asymmetrically to the source but with the same total thickness as that of the <sup>32</sup>P sample, and were also counted. The count rate of the two detectors are also presented in table 4.4.

Again, a relative efficiency E, was used, but the definition was modified as follows.

$$E_s = \frac{S_{asymmetric}}{S_{symmetric}}$$

Where  $S_{asymmetric}$  and  $S_{symmetric}$  are the sum of the count rates measured by both detectors, are given in table 4.4. As before  $S_{asymmetric}$ ,  $S_{symmetric}$  are corrected for  $^{32}$ P decay during the measurement. From the table, the values of  $E_s$  under various conditions are calculated. The resulting relative efficiency defined above is close to a constant showing little or no dependence on the degree of asymmetry in source position. This supported our assumption that the sum of the count rates in two detectors was relatively independent of the asymmetry in depth of the implantation for small symmetries. However because the sum of the count rate measured by the



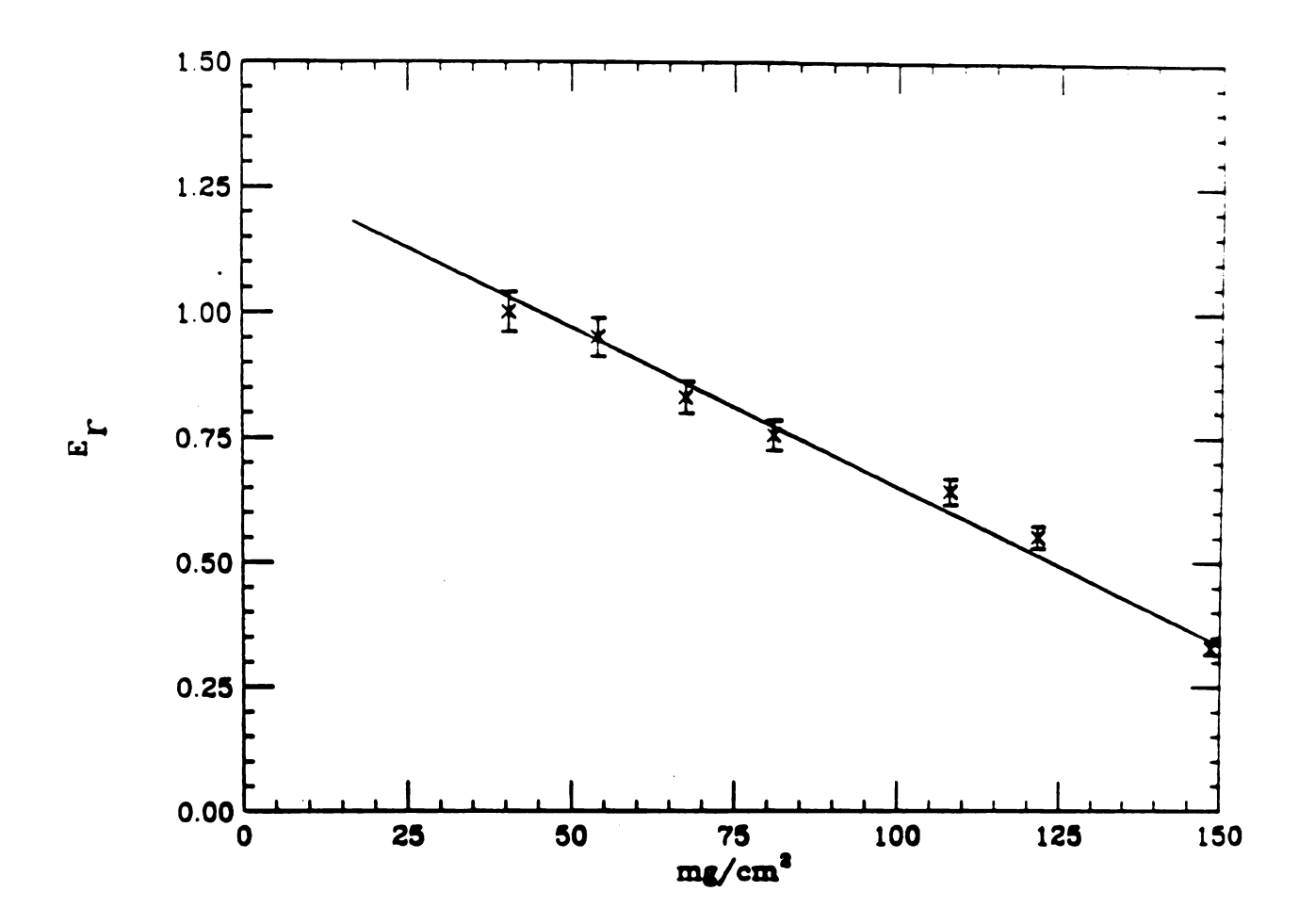


Figure 4.13: The relative efficiency  $E_r$  defined in the text as a function of the thickness of Al foils that separate the  $^{32}P$  nuclei from the detector

two detectors is not totally independent of the implantation depth of the sample, we used the data of figure 4.13 and table 4.4 to apply a small correction, typically 5 % or less to the measured activities of the  $^{32}$ P and  $^{32}$ Si sample. As determined by the measurement mentioned above, the  $^{32}$ P nuclei were implanted about 33 mg/cm<sup>2</sup> off the center. The asymmetry of  $^{32}$ Si nuclei was determined to be about 14 mg/cm<sup>2</sup> off the middle of the sample. Based upon count rates of the  $^{32}$ P samples measured, the total detection efficiency of the counting system for  $^{32}$ Si activity was determined to be  $E_t = 0.401 \pm 0.036$  for an energy threshold of 100 KeV.

The next step is to calculate the half-life of <sup>32</sup>Si. As explained in Chapter 2, the decay probability of <sup>32</sup>Si could be obtained from the following formula.

$$\lambda = \frac{-\frac{dN(t)}{dt}}{N(t)}$$

Where  $\lambda$  is the decay probability,  $-\frac{dN(t)}{dt}$  is the activity of the <sup>32</sup>Si sample at a time t, and N(t) is the number of <sup>32</sup>Si nuclei at time t. However, since the half-life of <sup>32</sup>Si is expected to be greater than 100 years, and the measurements of the decay rate of the sample were made a few months after the implantation, N(t) was replaced with the number of <sup>32</sup>Si implanted. The half-life of <sup>32</sup>Si was then obtained from  $\lambda$  using.

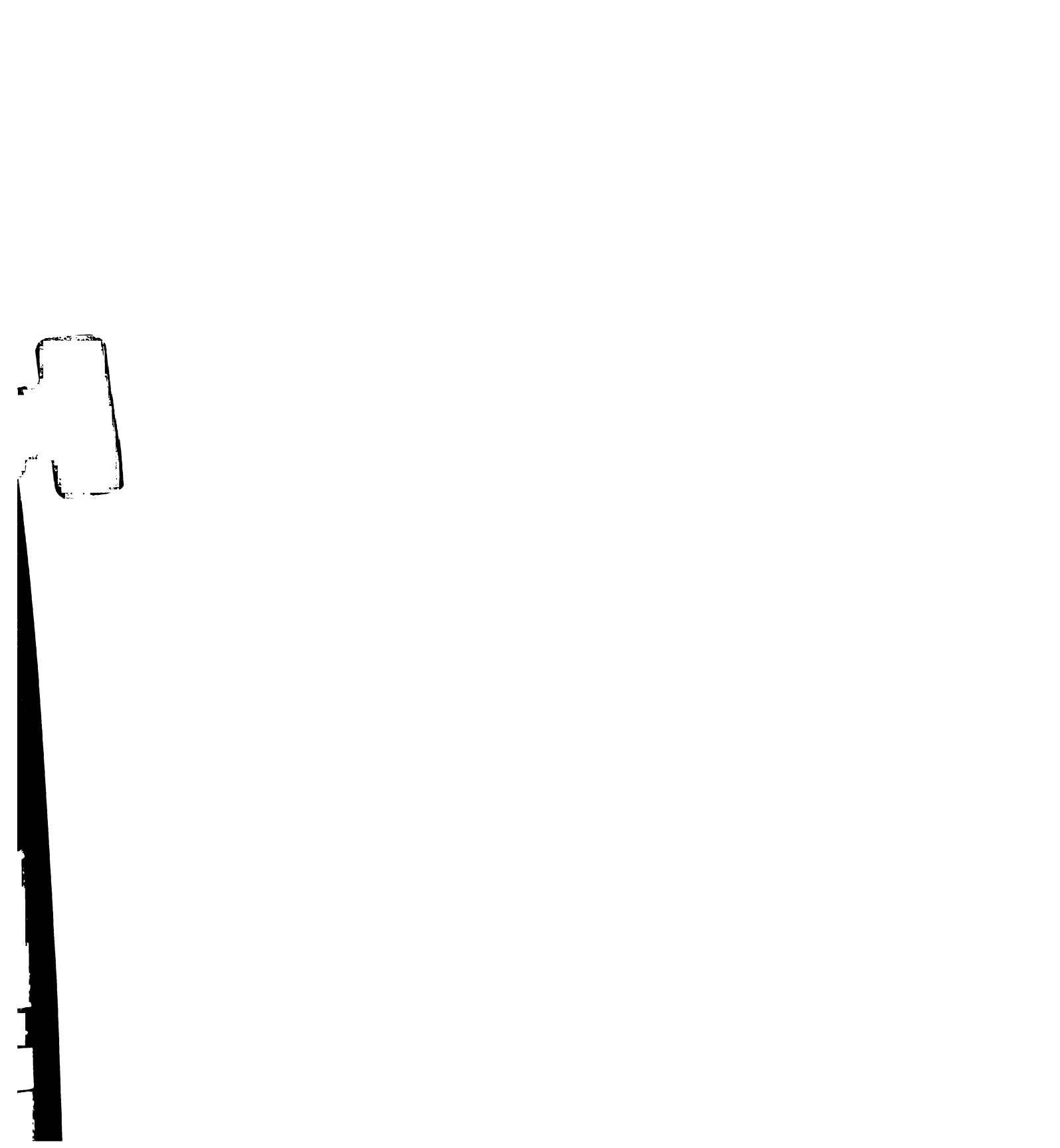
$$t_{\frac{1}{2}} = \frac{\ln 2}{\lambda}$$

The decay rate of the sample was obtained by correcting the decay rate measured by the detectors with the total detection efficiency as  $\frac{dN}{dt} = \frac{R_1 + R_2}{E_t}$  where all symbols are the same as defined previously. The decay rate of the <sup>32</sup>Si sample was calculated from the measured decay rate of the sample divided by the efficiency of the counting

Table 4.5: Uncertainties in half-life determination (from different sources)

							126 - C 216 · Y								
		00 07 32 10 <sup>3</sup> +3 61					Deca.	y Rote 10.3571	Deter (Avera	ge of	ion 11 Mea	S LITE FIL	nt)		
33	nederalis	Y	11			Octection Efficiency 0.404±0041			Decay Rice 3 eo 20 26 1 from a 3 naje measureme.				ment)		
		Equilibres 2%			32P Sample 1 32P Sample 2 0.39310030			Court Rute 3.6%		Æ	3 2%				
		<u> </u>			Agyanetig Correction		Number of 4P	Corrected	Decay Rote	Thereised Setting	Fool Pesition	Taketicu Hereniy	Threat Setting	Fred Partier	Sizzariaza Vez rene
				4.6%	5%	3%	4.2%	5%	4%	3.5 <b>%</b>	1%	0.1%	3%	1,8	پېد ز

system( $E_t$ ). The half-life of <sup>32</sup>Si was then determined to be 134  $\pm$  16. years. Table 4.5 list the various contribution to the uncertainty of <sup>32</sup>Si half-life measured in the second experiment, and one can see that the error is mainly due to the efficiency determination in the activity measurements.



## II Momentum distributions

To generate the momentum distributions of reaction fragments, a two dimensional contour gate was selected for each isotope in the particle identification spectra of TOF vs.  $\Delta E$  as shown in figure 4.15. Those gates were then used to sort the data. The position of the particle at image 2 of the A1200 was binned for particles identified by the various contour gates to form a spectrum. In this way, the position spectra of the nuclei of each isotope were generated. In figure 4.16, a typical position spectrum obtained this way is shown. The positions of the particles were measured at image 2 by a parallel plate avalanche counter (detector PPAC 1). The efficiency of detection across the detector was not uniform. This non-uniformity was corrected by making the momentum distribution taken at various neighbouring field settings smooth, and resulted in a correction curve valid for all isotopes. Figure 4.14 shows the relative efficiency as a function of channel number, with channel 256 corresponding to low radius of curvature of the fragments. Once all the position spectra for the nuclei of an isotope were extracted from the data, the next step was to convert the position distribution of the nuclei into momentum distribution. As mentioned in Chapter 3, the positions at image 2 of fully stripped beam with different  $B\rho$  were measured. Since the beam energy and the radius of the A1200 are known (E = 79.9 MeV/A,  $\rho = 3.095$  m), the radii of various trajectories of the beam for different B $\rho$  settings were calculated. We can then get the radius as a function of the measured position at image 2. In table 4.6, the calculated radii, measured positions at image 2, and fitting parameter are shown. With the relation between radius of particle trajectory and particle position at image 2 established, the momentum of a particle is easily calculated using the formula  $P = qB\rho$ , where P is the momentum of a particle, q is the charge of the particle, B is the field setting during a particular measurement,  $\rho$ 

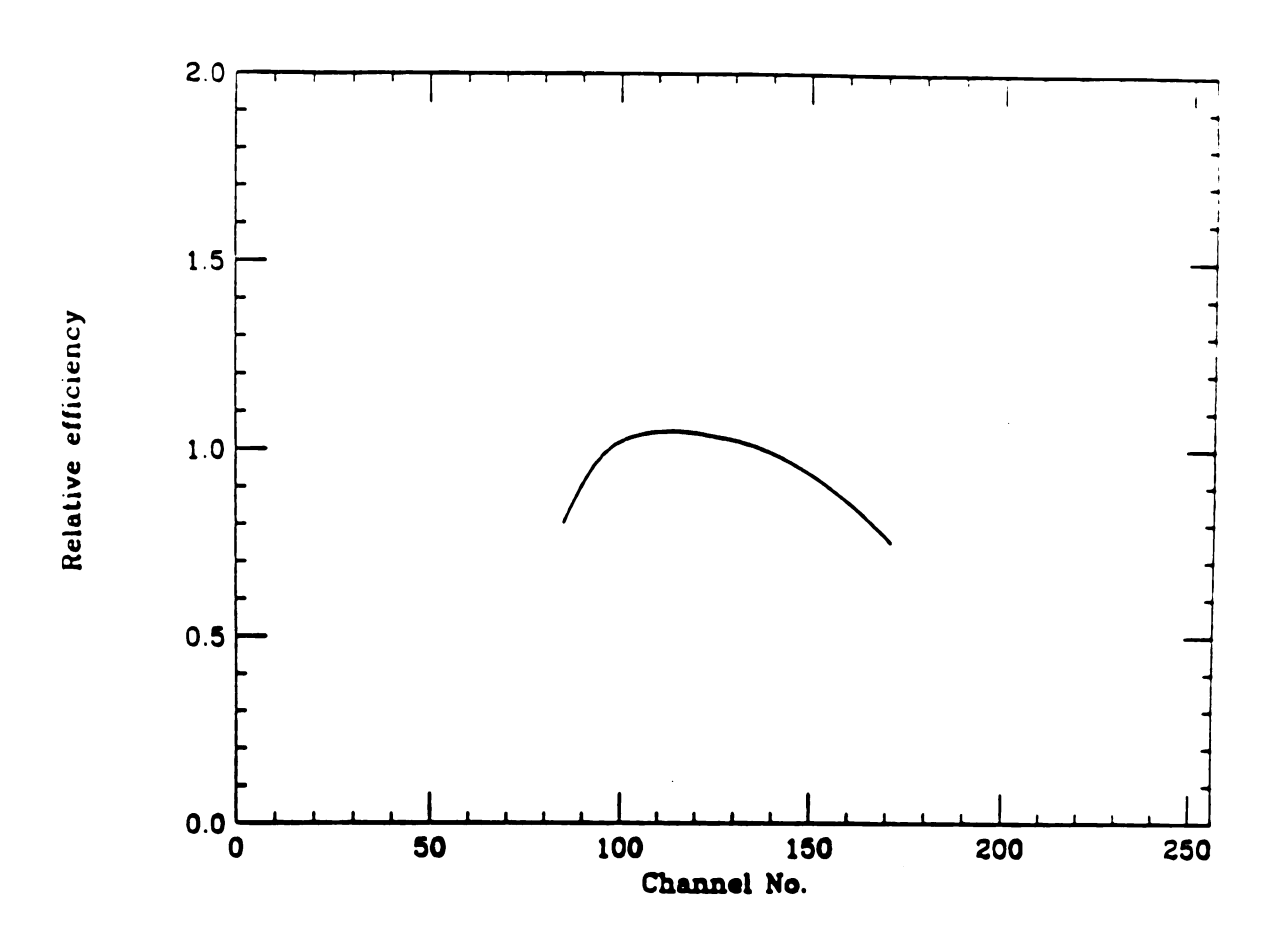


Figure 4.14: The relative efficiency of the PPAC 1 as a function of channel number

Table 4.6: Calibration parameters for positions measured by PPAC 2

Radii (m)	3.050	3.064	3.079	3.096	3.109	3.123
Beam position	68.67	87.28	107.80	129.76	147.02	165.02
centroid in channel No.						
Fitting result		ρ(1	m) = 2.9	98+ 0.00	07569×c	han

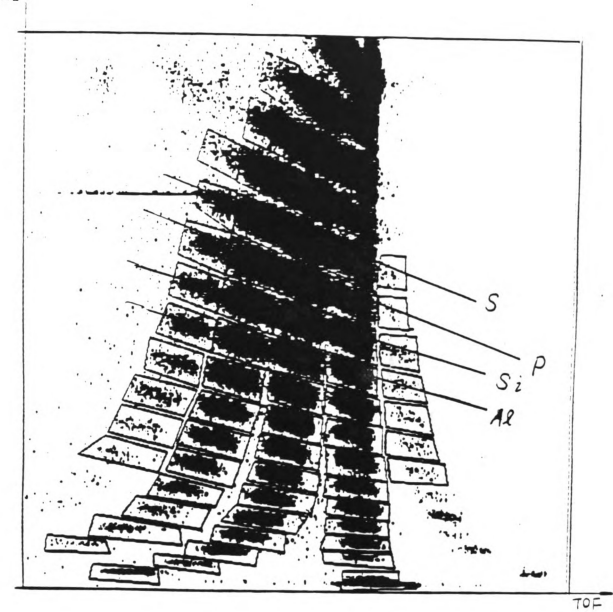
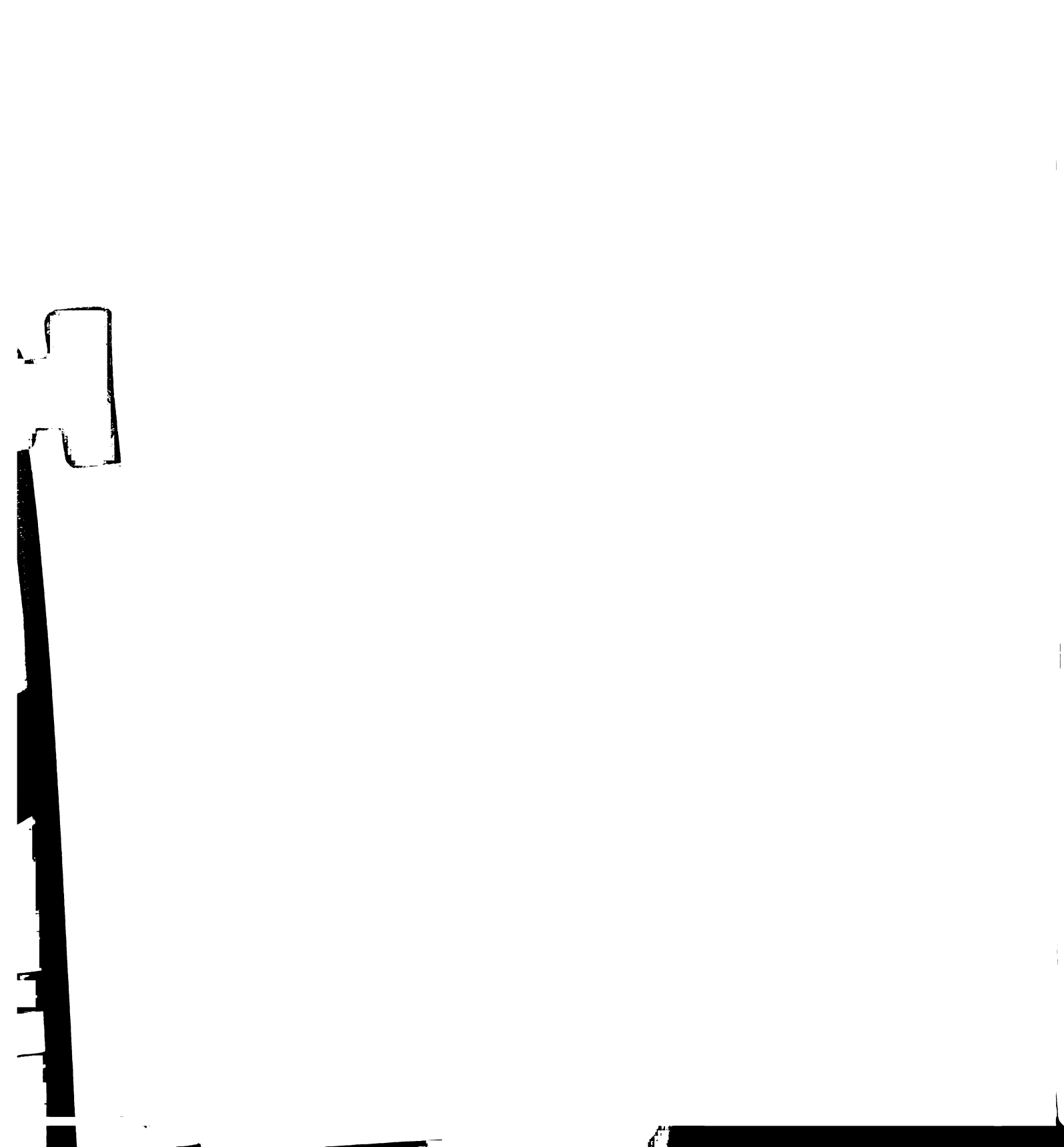


Figure 4.15: The PID histogram and the gates corresponding to different isotopes



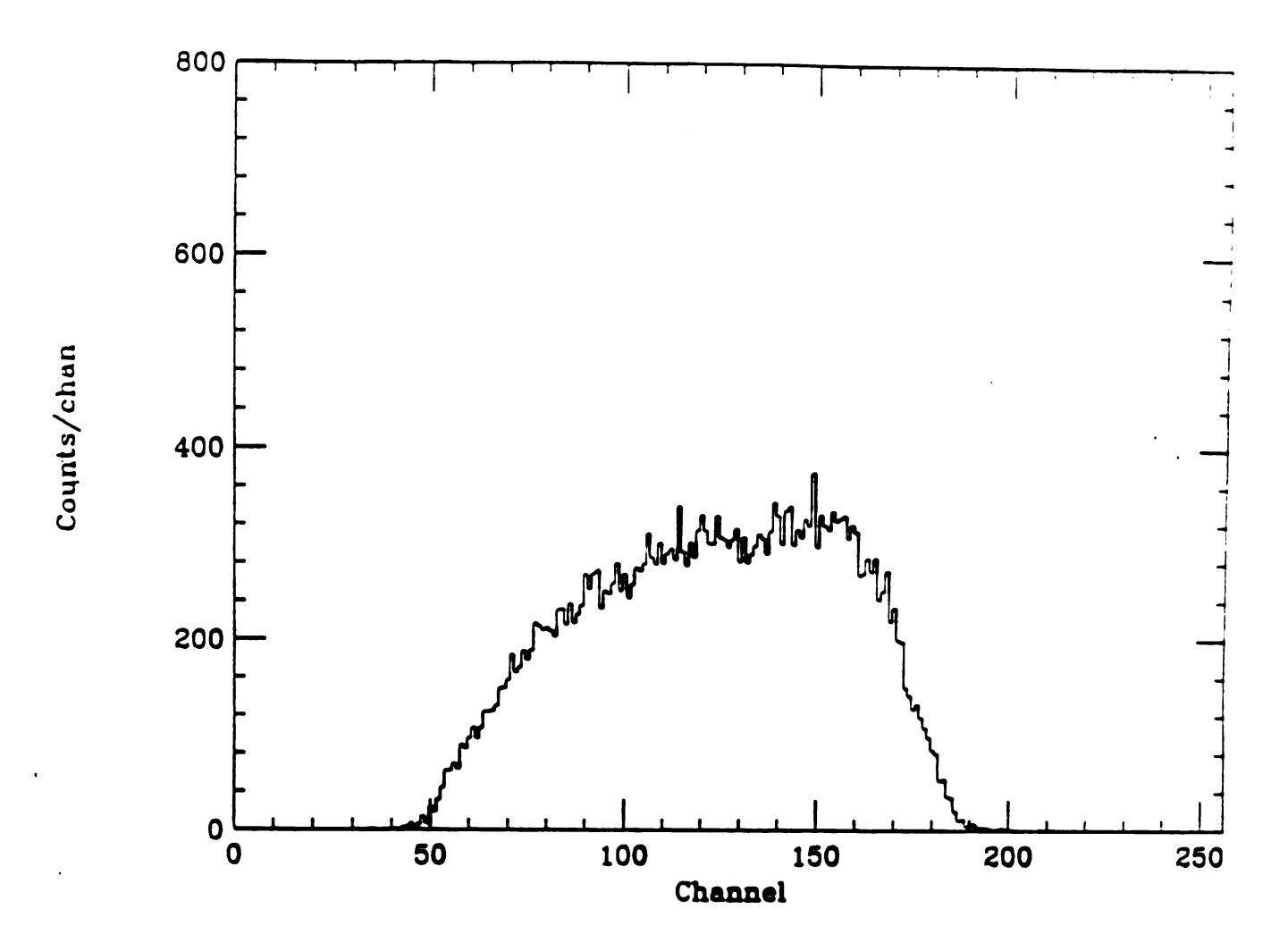


Figure 4.16: The position spectra of  $^{32}$ P nuclei measured by PPAC 1 at image #2. Target: Be, the dipole field of the first half of the A1200 B = 0.780 T

is the radius of the particle trajectory. The position spectra were then transformed into momentum distribution. The width of the momentum distribution was then extracted by fitting the measured distribution to a Gaussian curve plus a small constant background. In figure 4.17, the measured momentum distributions of A=32 nuclei and corresponding fitted curves are shown.

The widths of the momentum distribution obtained this way can be compared with model calculations such as Goldhaber's statistical model[Gol 74]. In this model, the nucleons in the projectile nucleus are considered to be independent particles moving inside a spherical potential well. The only correlation between the nucleons is from the momentum conservation, i.e. the total momentum of the nucleons in the rest frame of the projectile is zero. When part of the projectile is removed during collision with the target, it is assumed to carry away its relative momentum. Due to momentum conservation, the remaining part of the fragment recoils with an opposite momentum. If the motion of the nucleons in the projectile is isotropic, the recoil momentum distribution of the fragments, projected on a given coordinate is a Gaussian distribution. With the hypothesis of sudden fragmentation, i.e., a part is suddenly removed from the projectile by the interaction with target, it has been shown by Goldhaber that the width of the Gaussian distribution is as follows.

$$\sigma^2 = \sigma_0^2 \frac{A_F (A_P - A_F)}{A_P - 1}$$

where  $A_F$  is the mass number of the fragment,  $A_P$  is the mass number of the projectile, and the parameter  $\sigma_0$ , called the reduced width, is related to the nucleon momentum in the projectile by the expression:

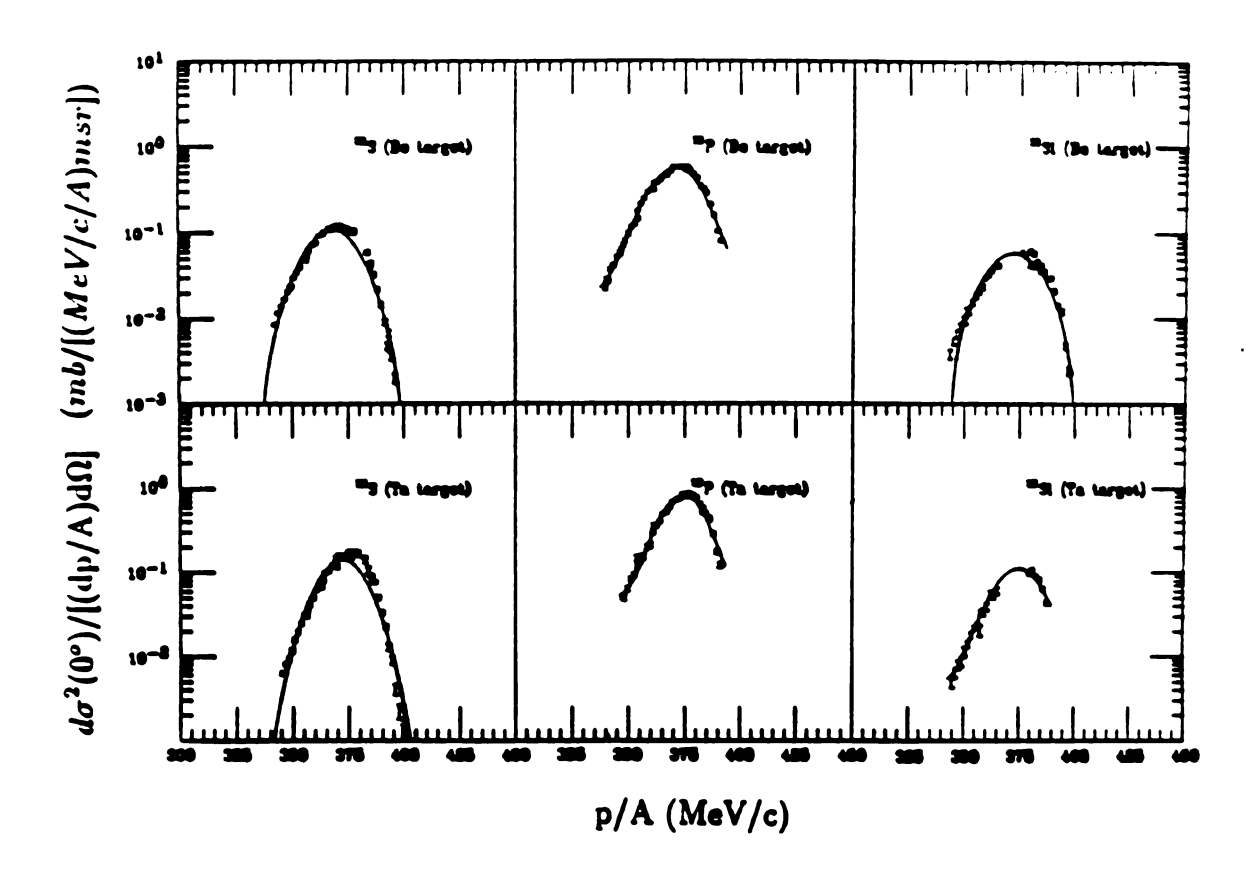
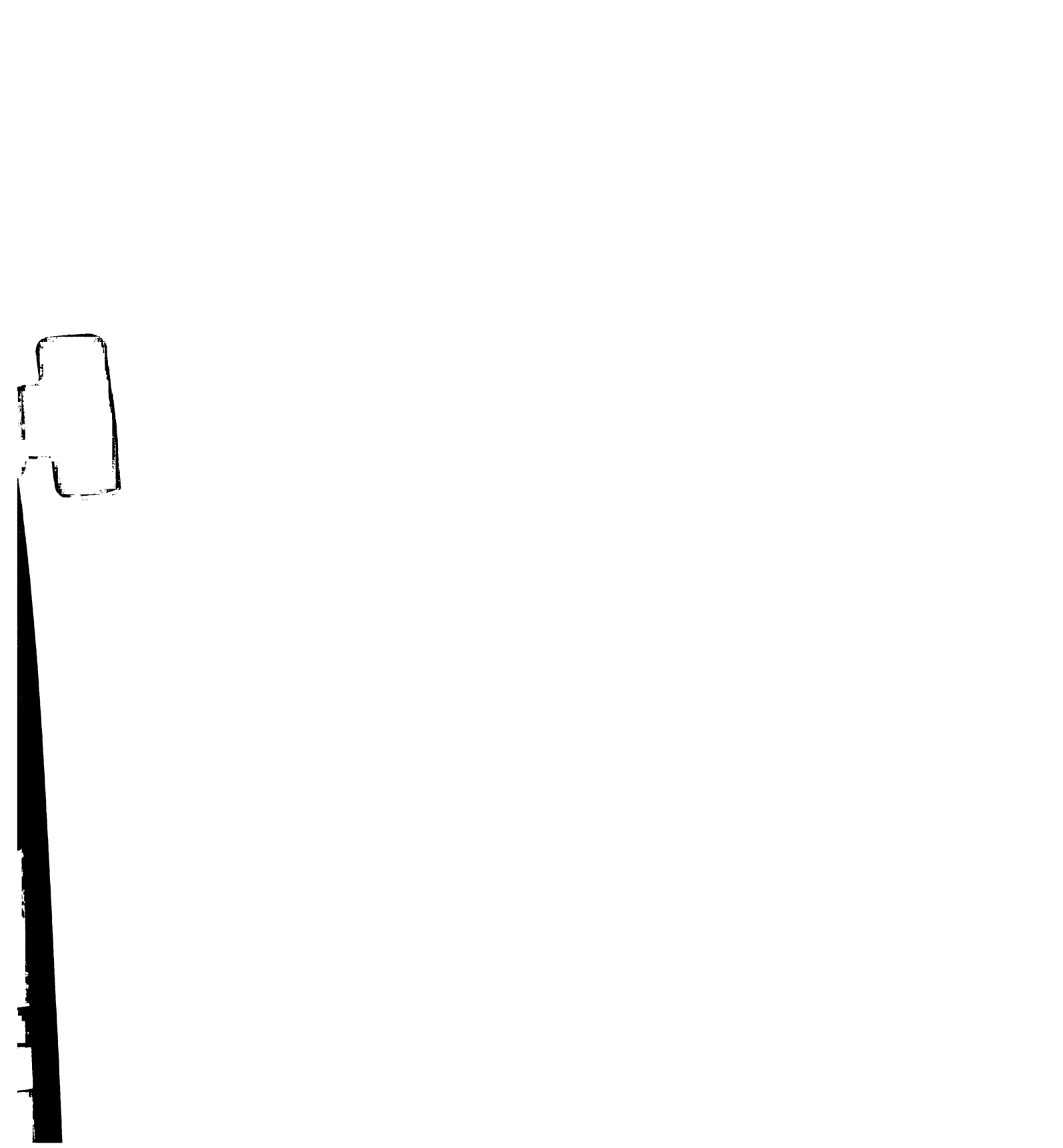


Figure 4.17: Measured momentum distributions of A=32 nuclei from the reactions of 80 MeV/A  $^{40}$ Ar on Be and Ta. The points with error bars are data points from the experiment and the solid line curves are fitted Gaussian distributions



$$\sigma_0^2 = \frac{\langle p_n^2 \rangle}{3}$$

where  $\langle p_n^2 \rangle$  is the average-square momentum of the nucleons in the particle. If the momenta of the nucleons in the projectile obey a Fermi distribution, we then have:

$$\langle p_n^2 \rangle = \frac{3}{5} p_{Fermi}^2$$

where  $p_{Fermi}$  is the Fermi momentum. The reduced width can then be written as:

$$\sigma_0^2 = \frac{p_{Fermi}^2}{5}$$

The value of the nucleon Fermi momentum  $p_{Fermi}$  has been obtained from experimental studies of electron quasi-scattering scattering[Mon71], and the value for  $^{40}$ Ar is 251 MeV/c  $\pm$  5 MeV/c. The predicted widths of the fragment distributions can then be calculated, and the results are plotted along with the measured widths, which have been corrected for multiple scattering in the target, in figure 4.18 and figure 4.19. One can see that the agreement between the pure theoretical result and the experimental data is not very good, but the trend of the data is correctly predicted by the formula with a fitted value of  $\sigma_0 = 89$  MeV/c and they will be discussed in the next chapter.

By integrating the momentum distributions, we can obtain the differential reaction cross section of the isotopes at 0°. In figure 4.20 those experimental differential reaction cross sections for Si isotopes are plotted as function of the mass number, and

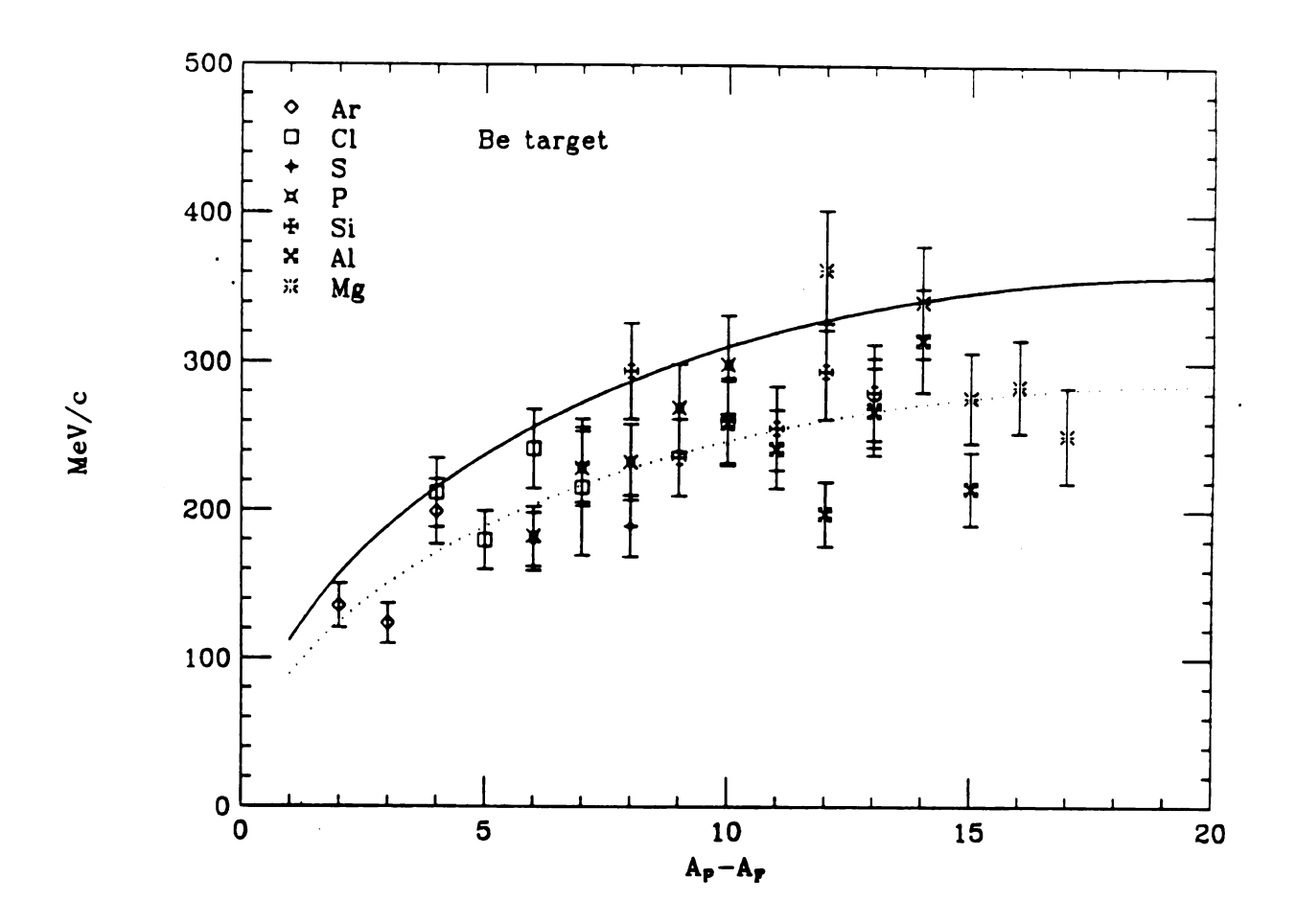


Figure 4.18: The widths of momentum distributions of different isotopes as a function of number of nucleons removed from the projectile. The data points represented by different symbols with error bars are the measured widths in the experiment with Be target and the solid line is from the calculation of Goldhaber model using the measured Fermi momentum value of  $^{40}$ Ar  $p_{Fermi} = 251$  MeV/c. The dotted line is a leastsquare fit of the data based on the Goldhaber model with a fitted  $\sigma_0 = 89$  MeV/c

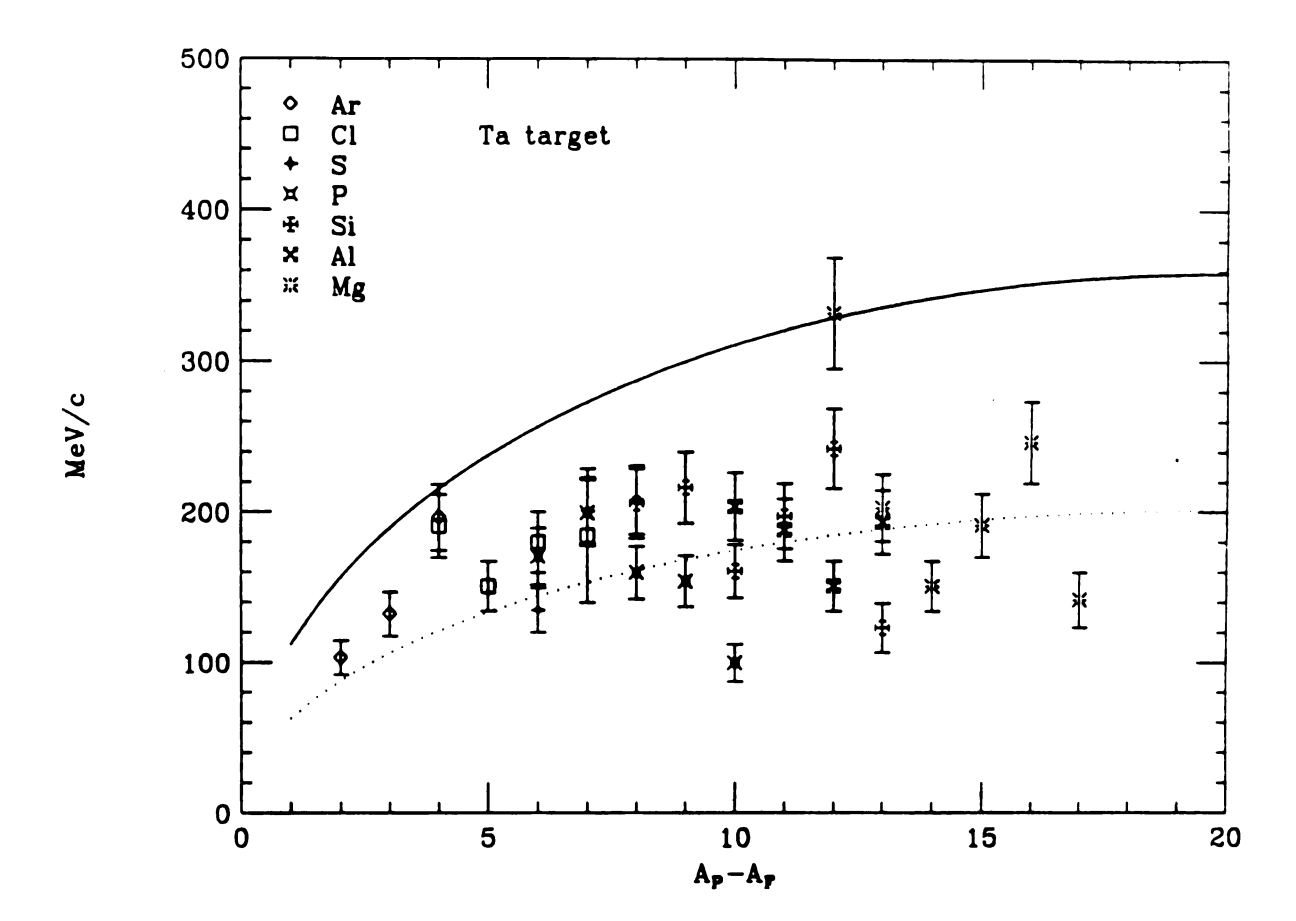
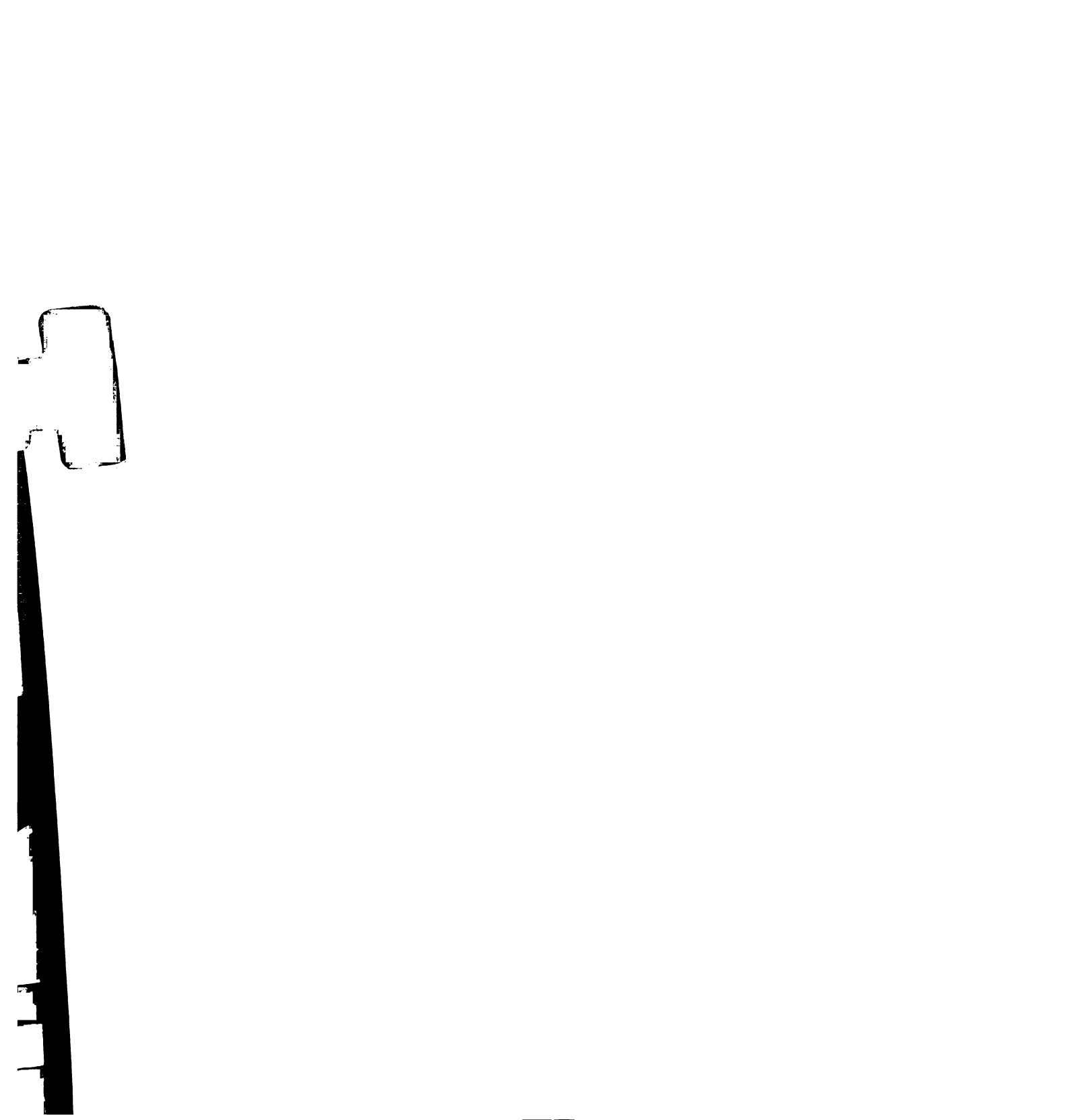


Figure 4.19: The widths of momentum distributions of different isotopes as a function of number of nucleons removed from the projectile. The data points represented by different symbols with error bars are the measured widths in the experiment with Ta target and the solid line is from the calculation of Goldhaber model using the measured Fermi momentum value of  $^{40}$ Ar  $p_{Fermi} = 251$  MeV/c. The dotted line is a leastsquare fit of the data based on the Goldhaber model with a fitted  $\sigma_0 = 68$  MeV/c



the results from empirical calculations using "INTENSITY" are shown plotted using a dotted line[Win 91]. In figure 4.21 – figure 4.26, the differential cross sections of several other isotopes are also shown. One can the see that the differential reaction cross sections as function of mass numbers for both experimental results and calculations show peaks near those isotopes the A/Z ratios of which are close to that of the projectile (40Ar). However, the calculated widths of those isotope distributions are large compared to the experimentally observed width. In most cases, the calculations underestimate the differential cross section for the lighter isotopes, and overestimate at the tail of the distribution. Generally, the agreement between the experimental results and empirical calculations is within a factor of 3 or less. Those results will be discussed in the next chapter.

In addition to the momentum distributions of the isotopes and the widths of the momentum distribution, one can also compare the measured centroids (in p/A) of the momentum distributions with the momentum/nucleon of the beam. The mean momentum/nucleon of the fragments can be simply calculated by energy conservation. If the initial kinetic energy of the projectile is  $T_P$ , and the energy required to remove  $\Delta A$  nucleons from the projectile is  $E_s$ , then the projectile kinetic energy at the moment of fragmentation is  $T_P - E_s$ , the fragment's mean energy per nucleon  $\frac{\langle T_F \rangle}{A_F}$  is given by the following formula

$$\frac{\langle T_F \rangle}{A_F} = \frac{T_P - E_s}{A_P}$$

The fragments's mean parallel momentum/nucleon can be easily obtained from this as

$$\frac{\langle p_F \rangle}{A_F} = \frac{1}{c} \sqrt{\frac{\langle T_F \rangle}{A_F} (\frac{\langle T_F \rangle}{A_F} + 2m_n c^2)}$$

where  $m_n$  is the rest mass of a bound nucleon ( $m_n c^2 = 931.5 \text{ MeV}$ ). Depending on

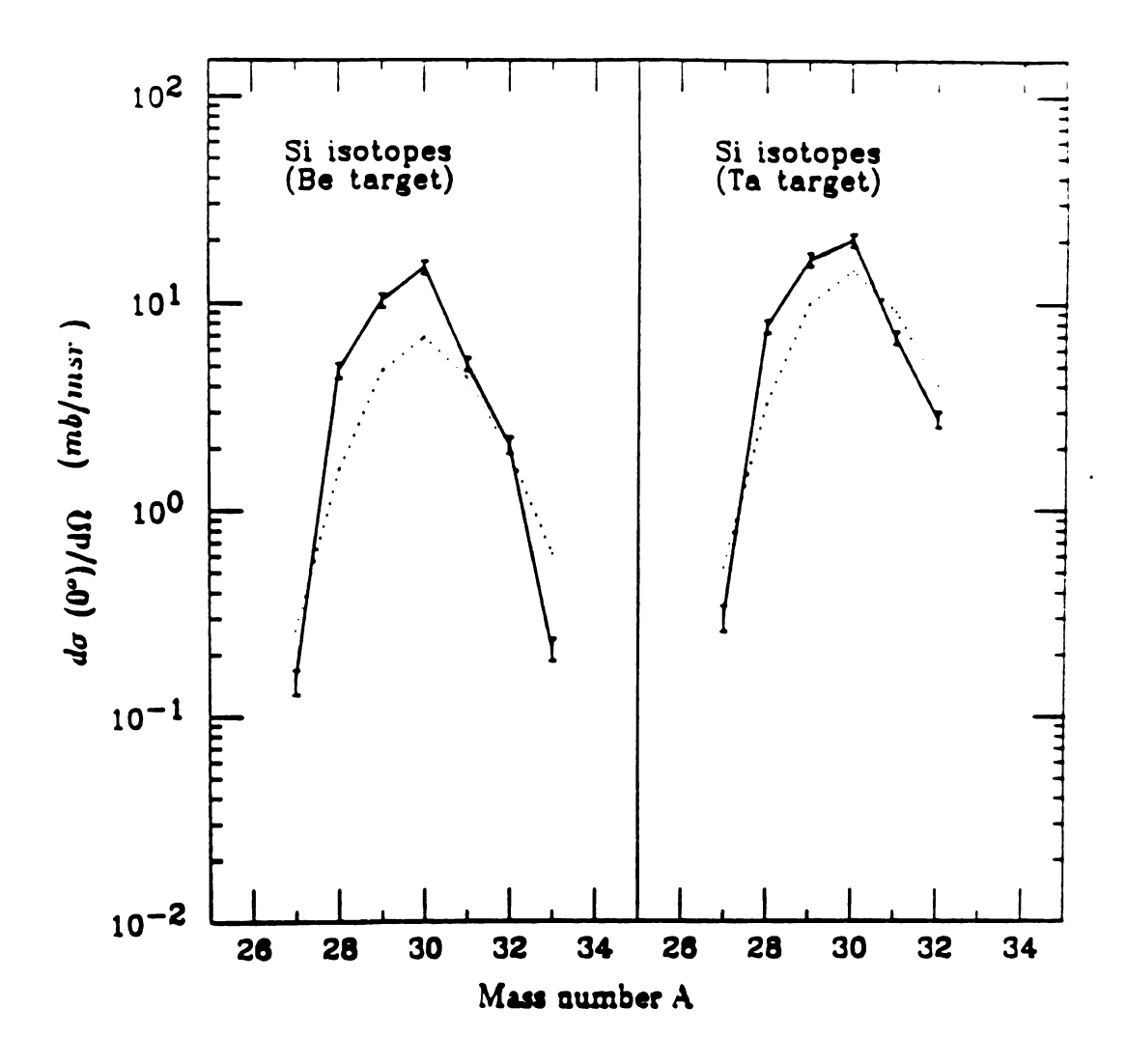


Figure 4.20: The differential reaction cross section of Si isotopes at 0° as functions of mass number A. The points connected by the solid lines are the experimental results, and the points connected by dotted lines are from calculations using "INTENSITY" [Win 91]

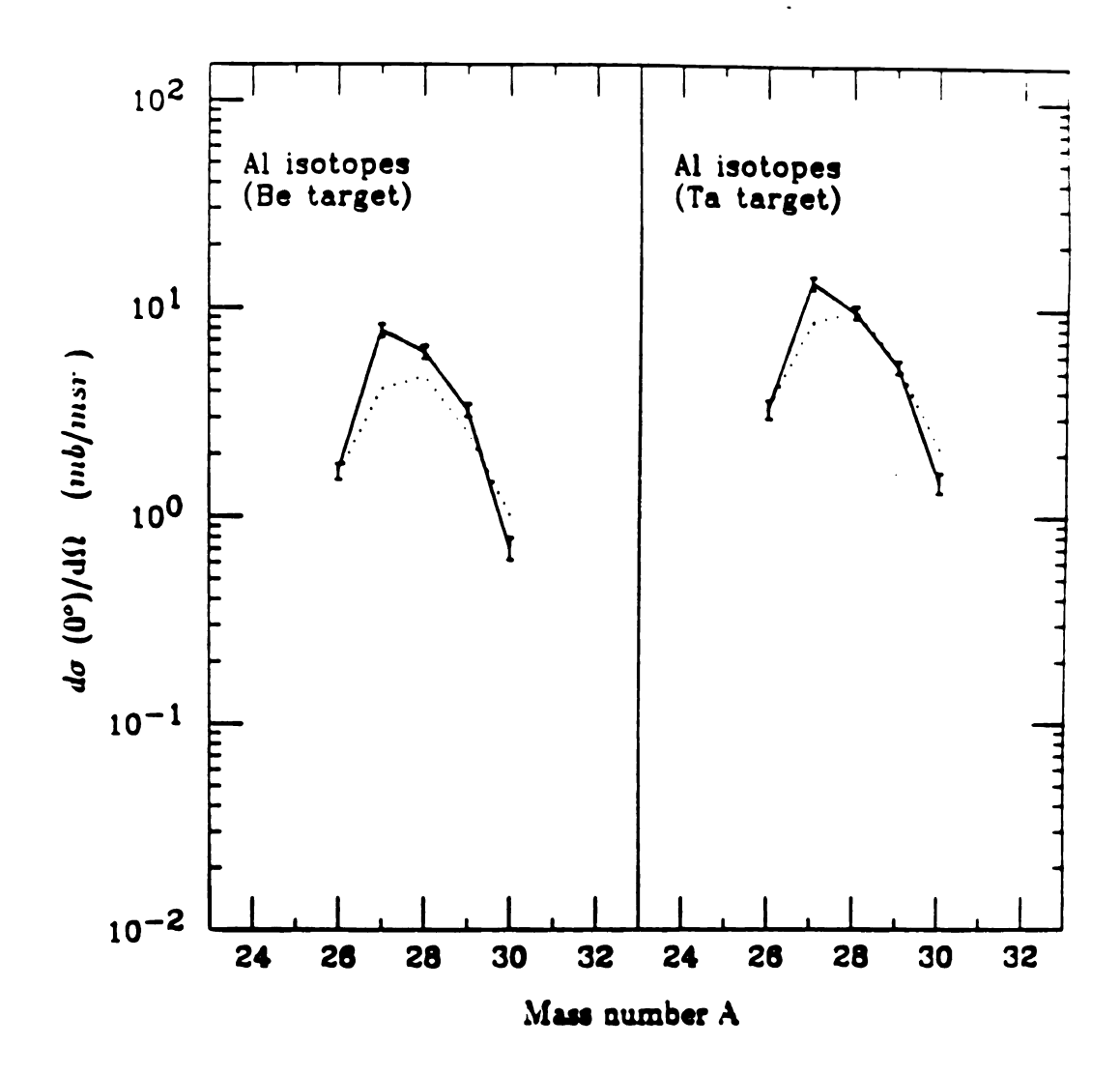
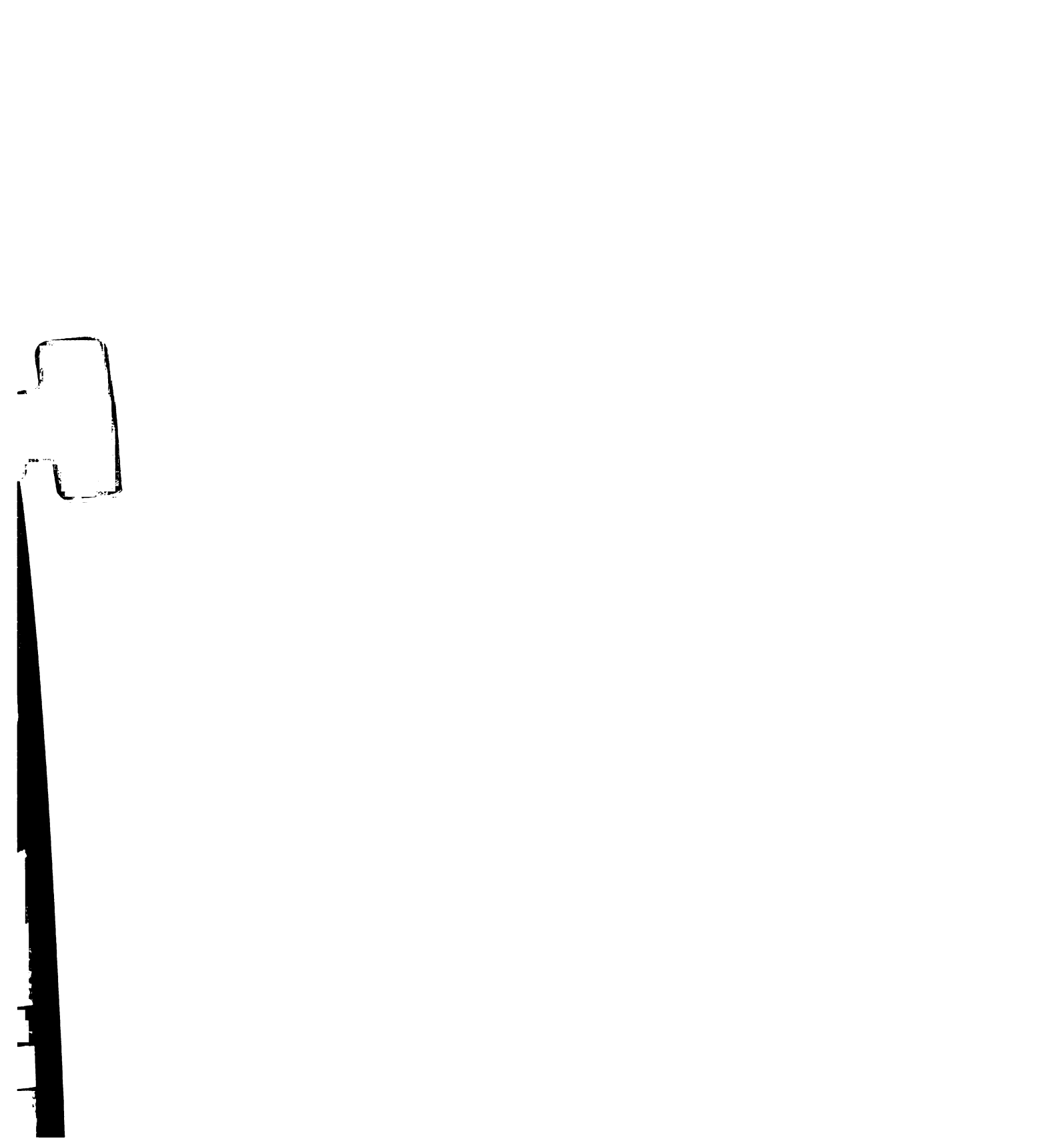


Figure 4.21: The differential reaction cross section of Al isotopes at 0° as functions of mass number A. The points connected by the solid lines are the experimental results, and the points connected by dotted lines are from calculations using "INTENSITY" [Win 91]



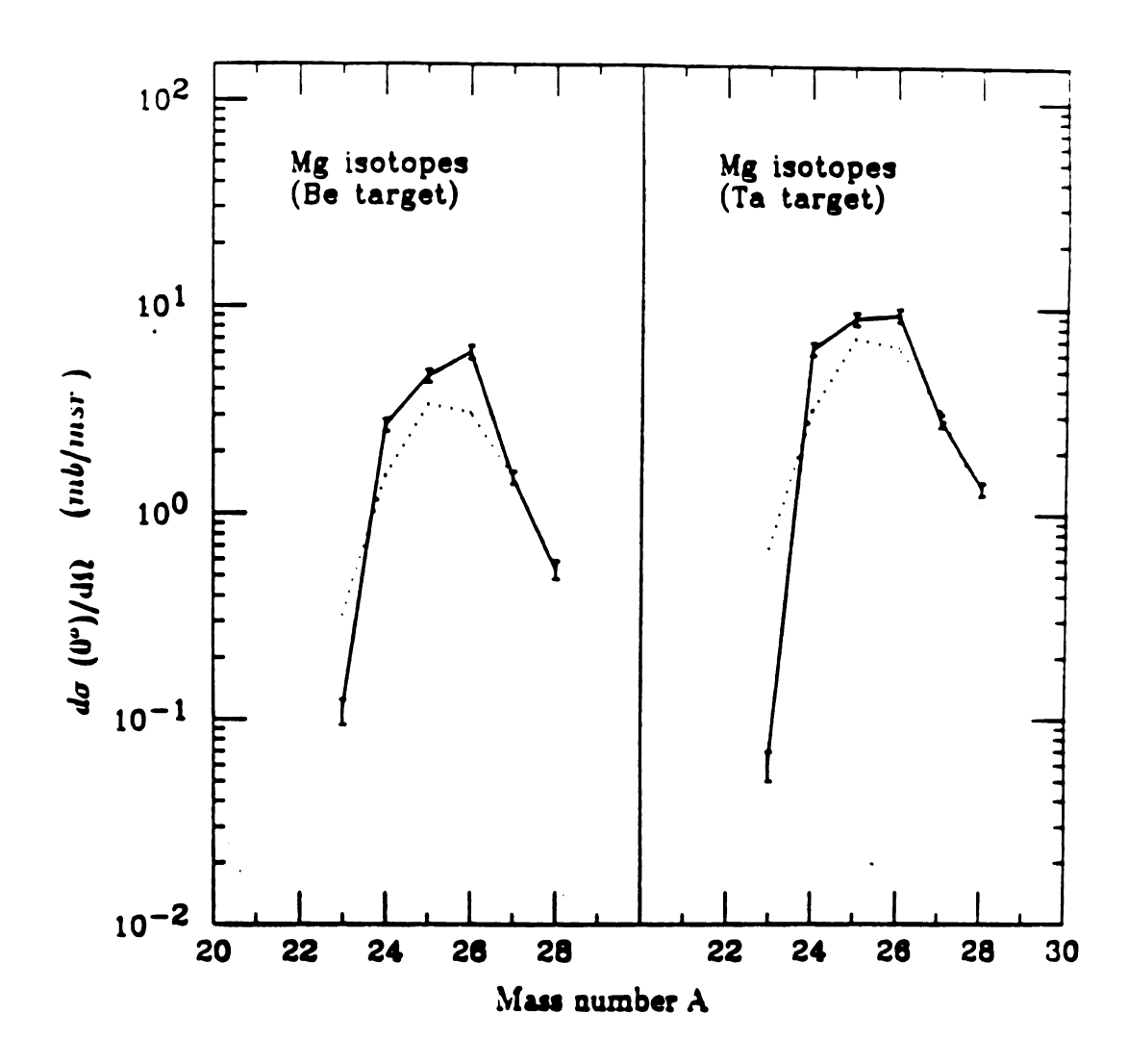


Figure 4.22: The differential reaction cross section of Mg isotopes at 0° as functions of mass number A. The points connected by the solid lines are the experimental results, and the points connected by dotted lines are from calculations using "INTENSITY" [Win 91]

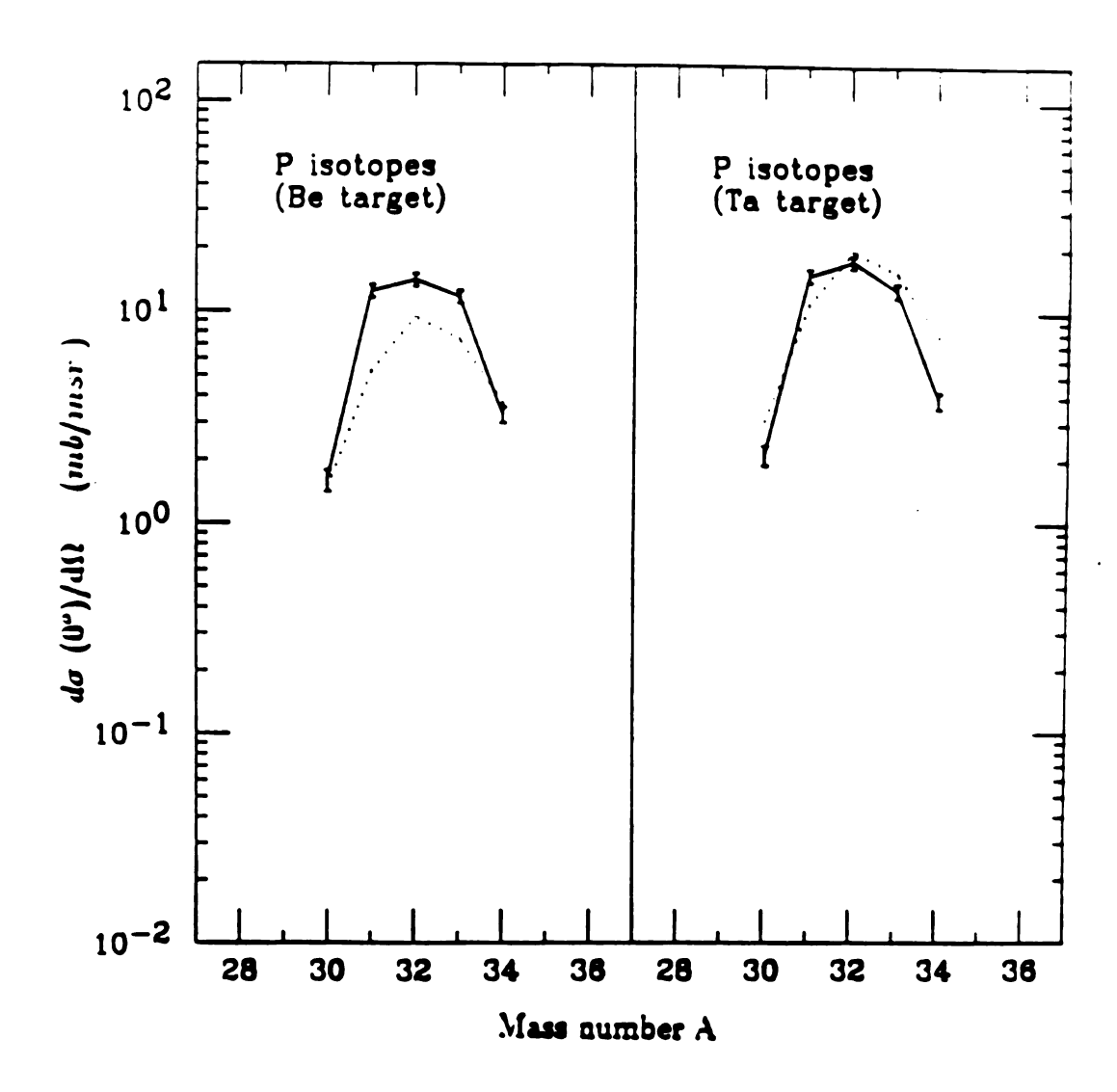


Figure 4.23: The differential reaction cross section of P isotopes at 0° as functions of mass number A. The points connected by the solid lines are the experimental results, and the points connected by dotted lines are from calculations using "INTENSITY" [Win 91]

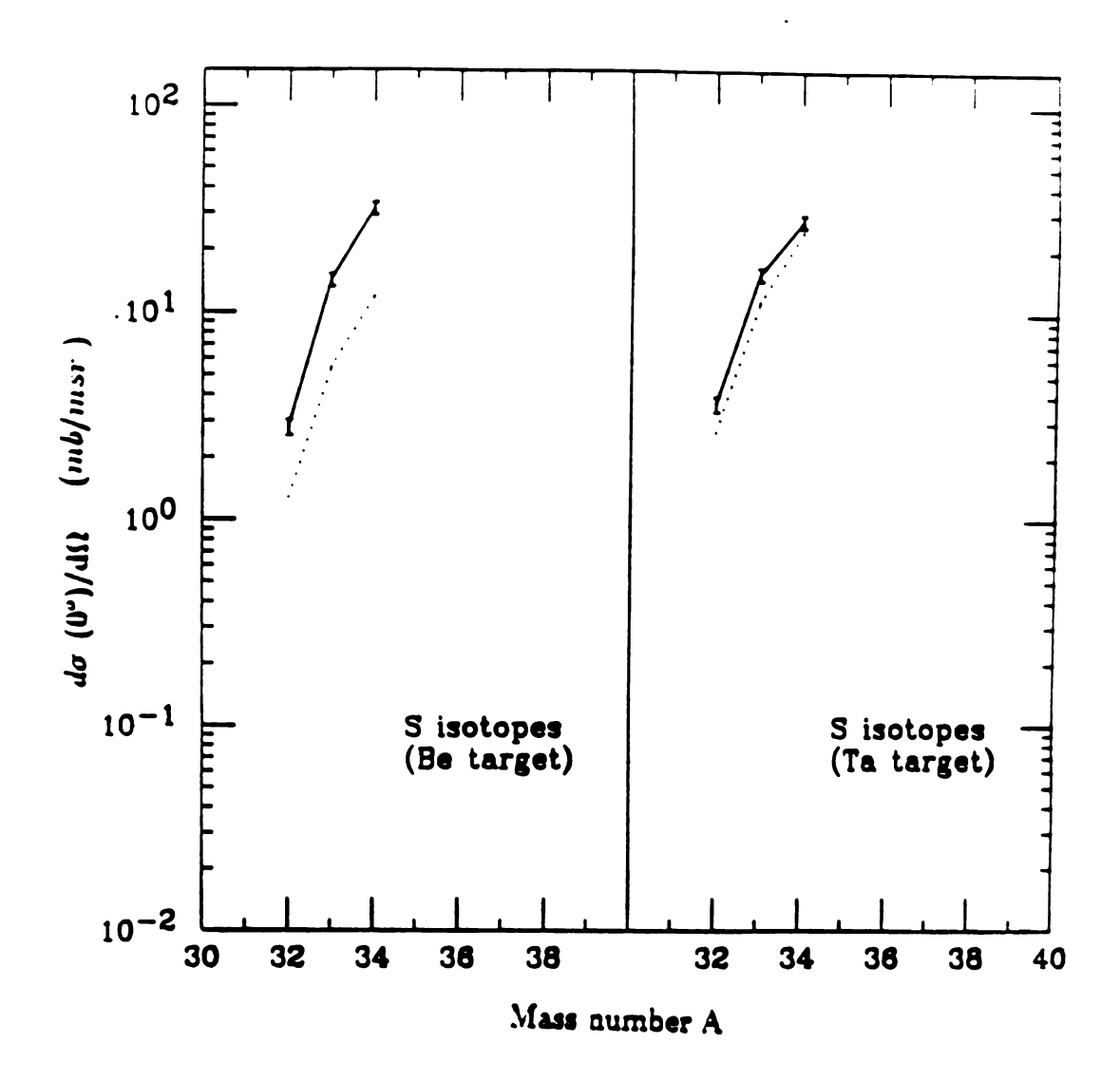
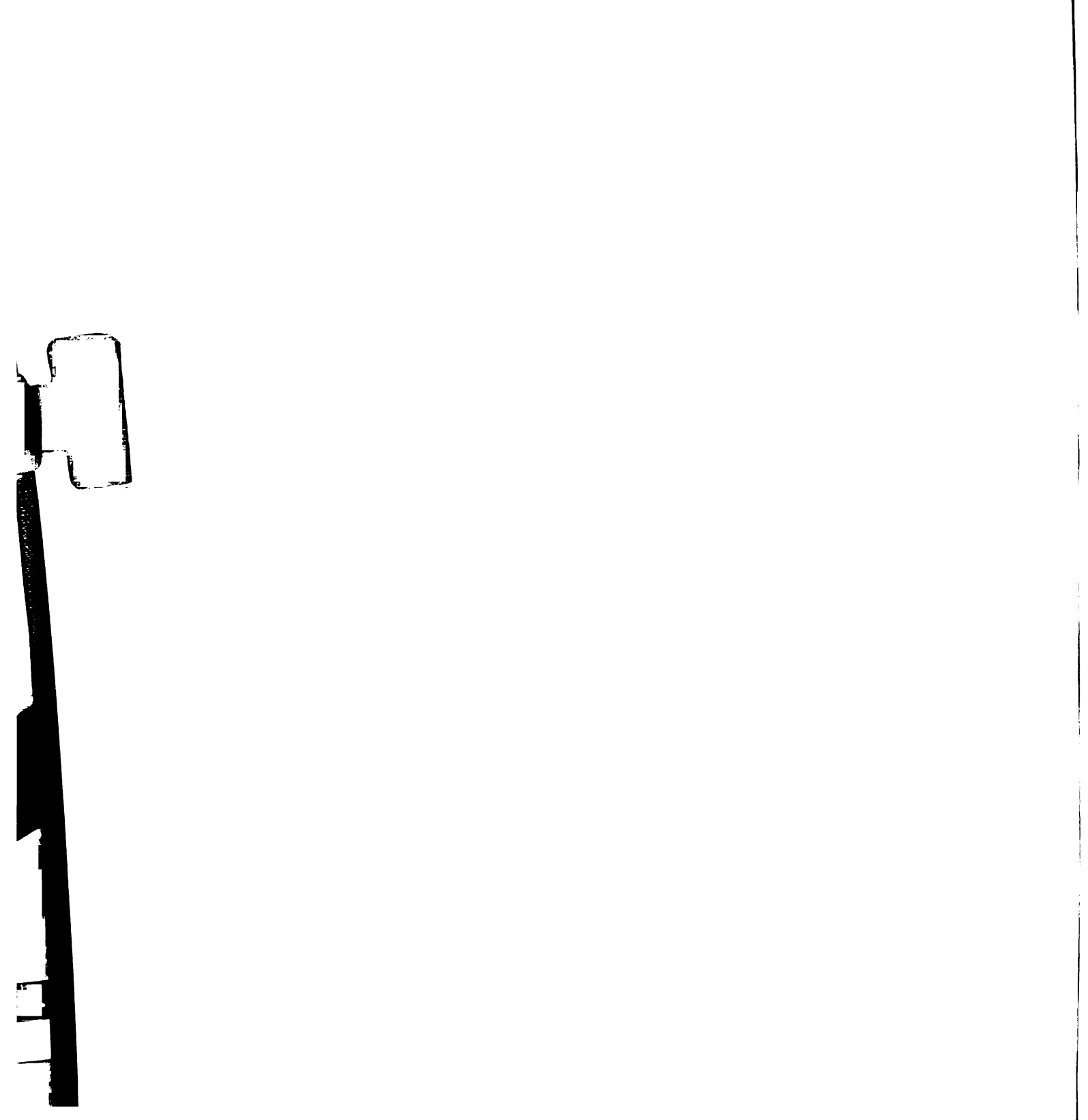


Figure 4.24: The differential reaction cross section of S isotopes at 0° as functions of mass number A. The points connected by the solid lines are the experimental results, and the points connected by dotted lines are from calculations using "INTENSITY" [Win 91]



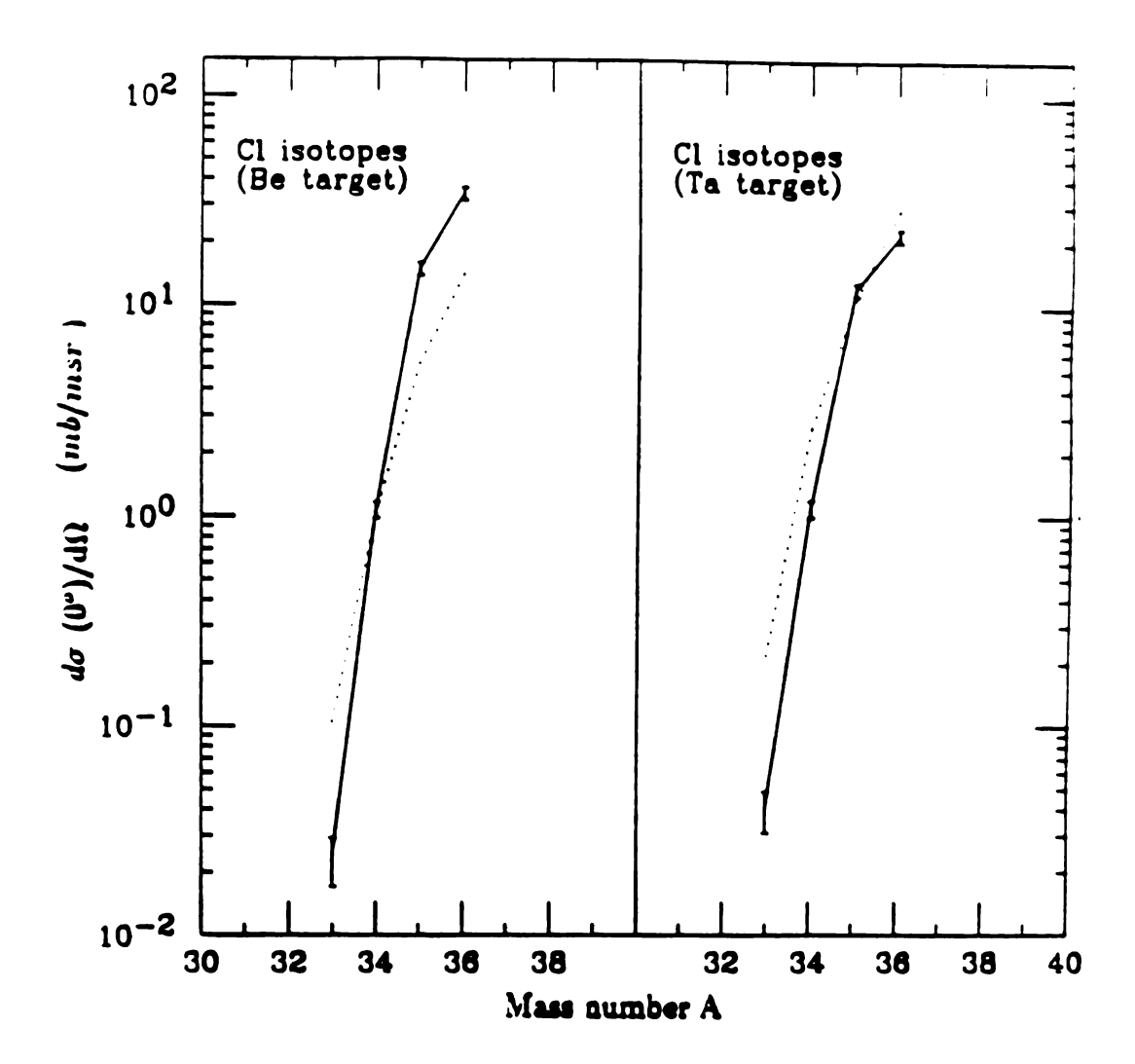


Figure 4.25: The differential reaction cross section of Cl isotopes at 0° as functions of mass number A. The points connected by the solid lines are the experimental results, and the points connected by dotted lines are from calculations using "INTENSITY" [Win 91]

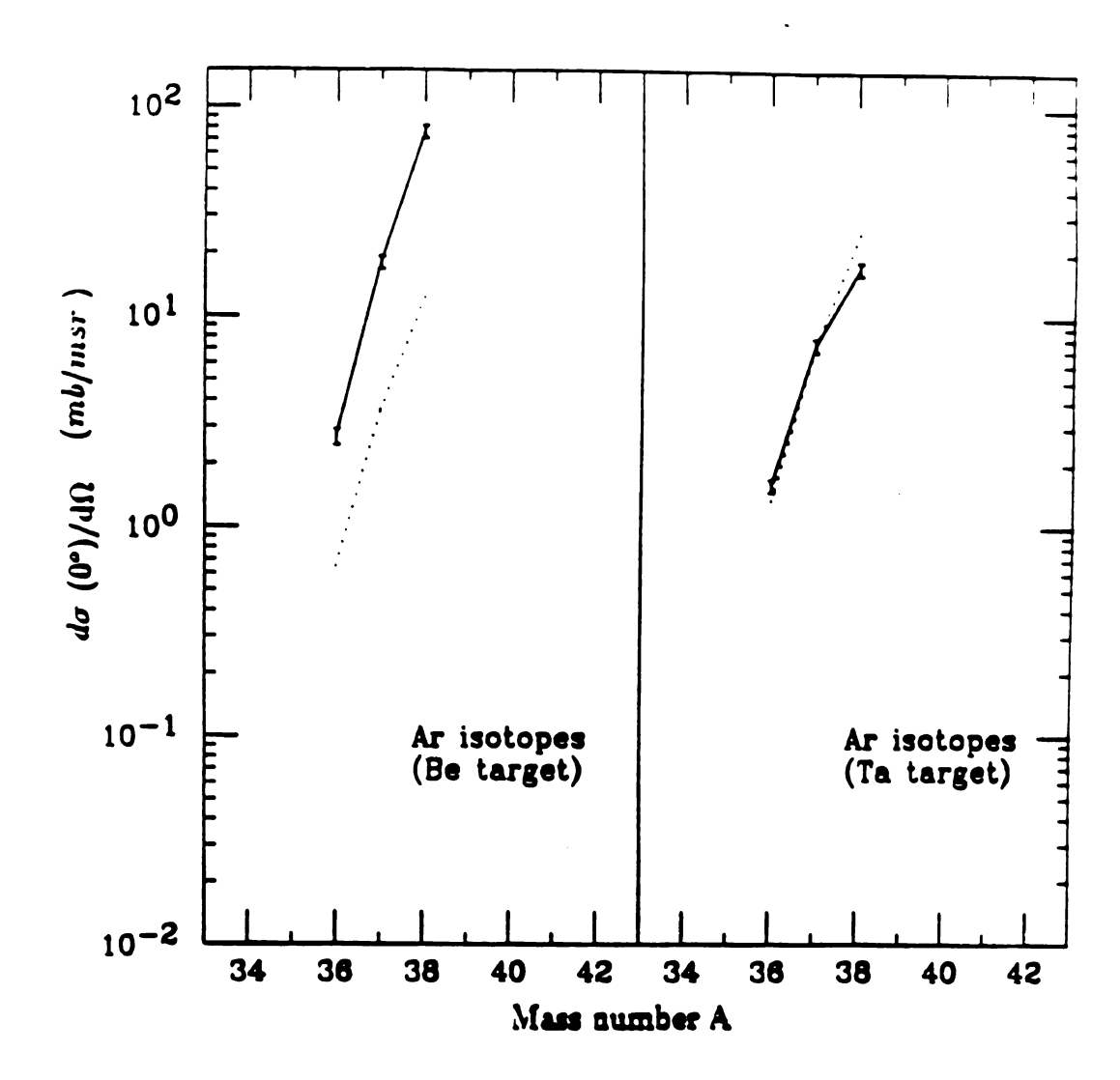
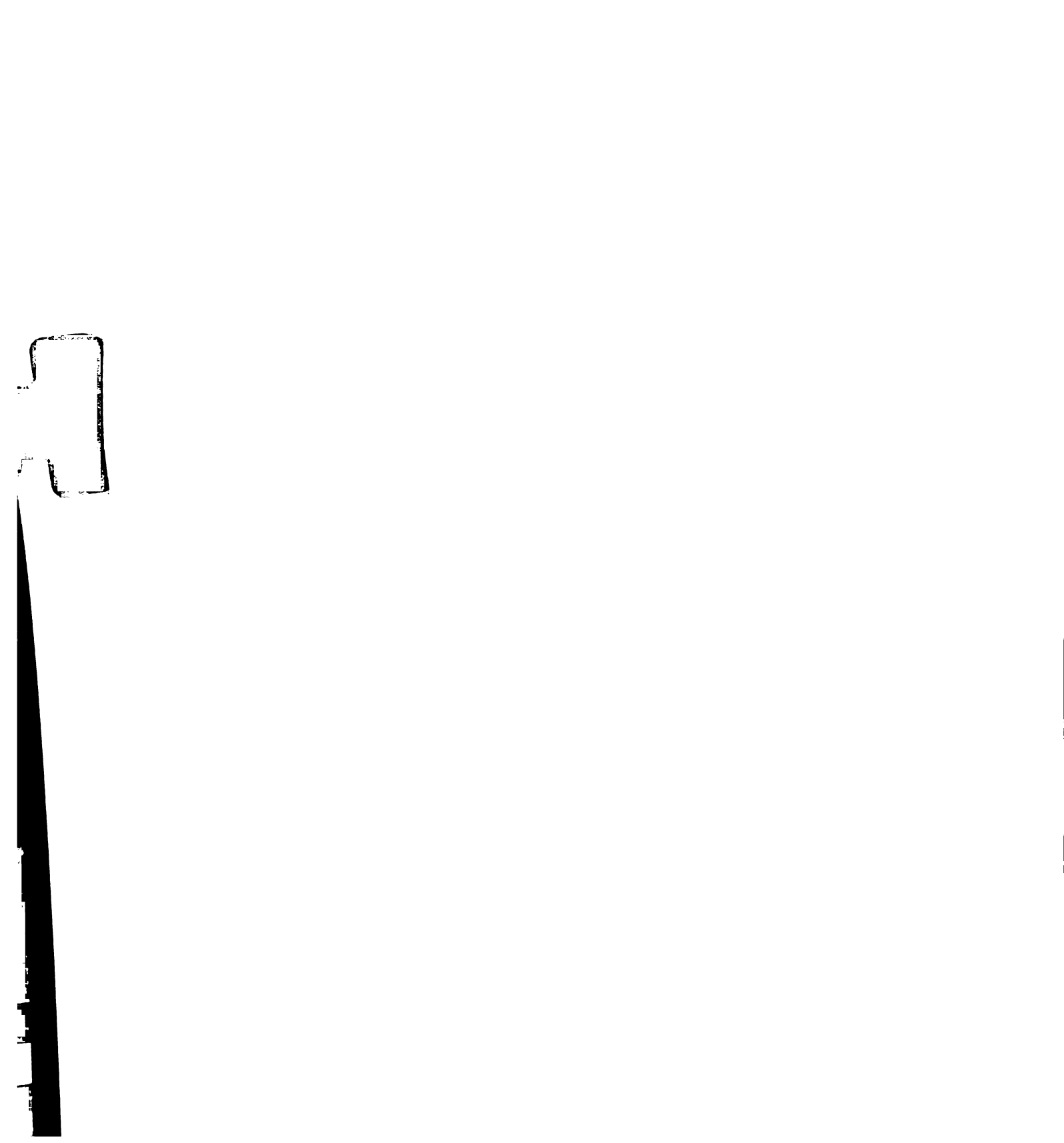


Figure 4.26: The differential reaction cross section of Ar isotopes at 0° as functions of mass number A. The points connected by the solid lines are the experimental results, and the points connected by dotted lines are from calculations using "INTENSITY" [Win 91]



the assumptions about the mechanism of the removal of nucleons from the projectile, one can get different estimates of  $E_s$ . But for a stable projectile, the energy required for the removal of a few nucleons is always non-negative, therefore the fragment's mean momentum/nucleon should be lower than that of the beam. To get a quantitative comparison between experimental results and the theoretical calculation, one also has to include the effect of energy loss of both the fragment and the projectile in the target. To simplify this comparison, we compared our experimental results with the output of the program 'INTENSITY'. The program calculation takes the effect of the energy loss in the target into account and calculates the mean momentum/nucleon of the fragment at the moment of fragmentation by assuming that the nucleons are independent particles and the energy required to remove nucleon is given by:

$$E_s = E_{s,n} \Delta A$$

where  $E_{s,n}$  is the average separation energy per nucleon ( $\sim$ 8 MeV for medium and heavy nuclei). In figure 4.27—4.28, the centroids of the momentum distributions of various isotopes (in p/A) divided by the beam momentum/nucleon (corrected for beam energy loss) are plotted as a function of the projectile mass loss ( $A_P$ - $A_F$ ), and the calculated results using program 'INTENSITY' are plotted along with the experimental results. One can see that the agreements between the experimental data and program calculation is very good. This will be discussed in the next chapter.

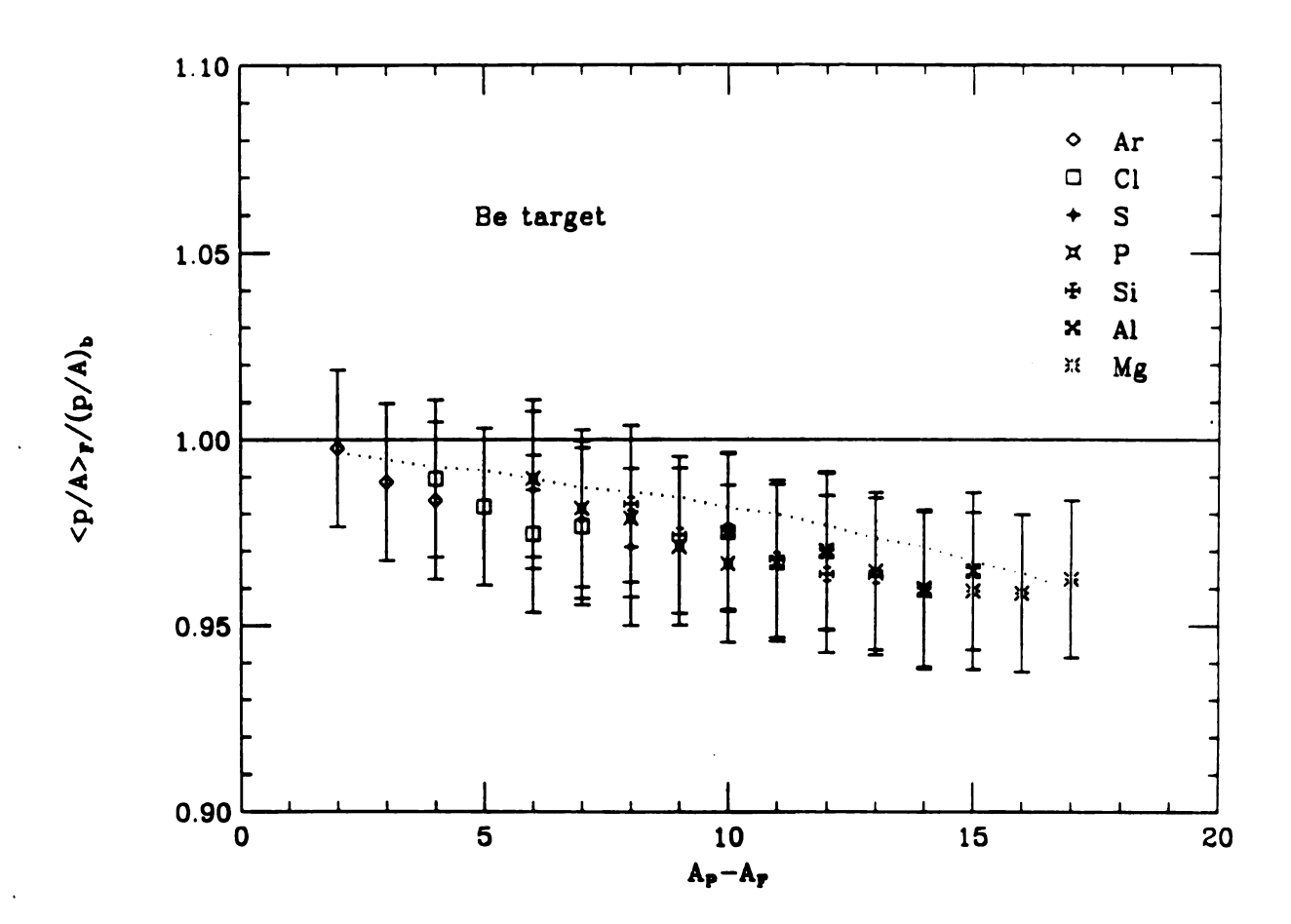


Figure 4.27: The centroids of the momentum distributions (in p/A) of various isotopes relative to the beam momentum/nucleon as function of projectile mass loss. The solid line represent the beam momentum/nucleon measured in the experiment with the same target. the dotted line is from the program calculation

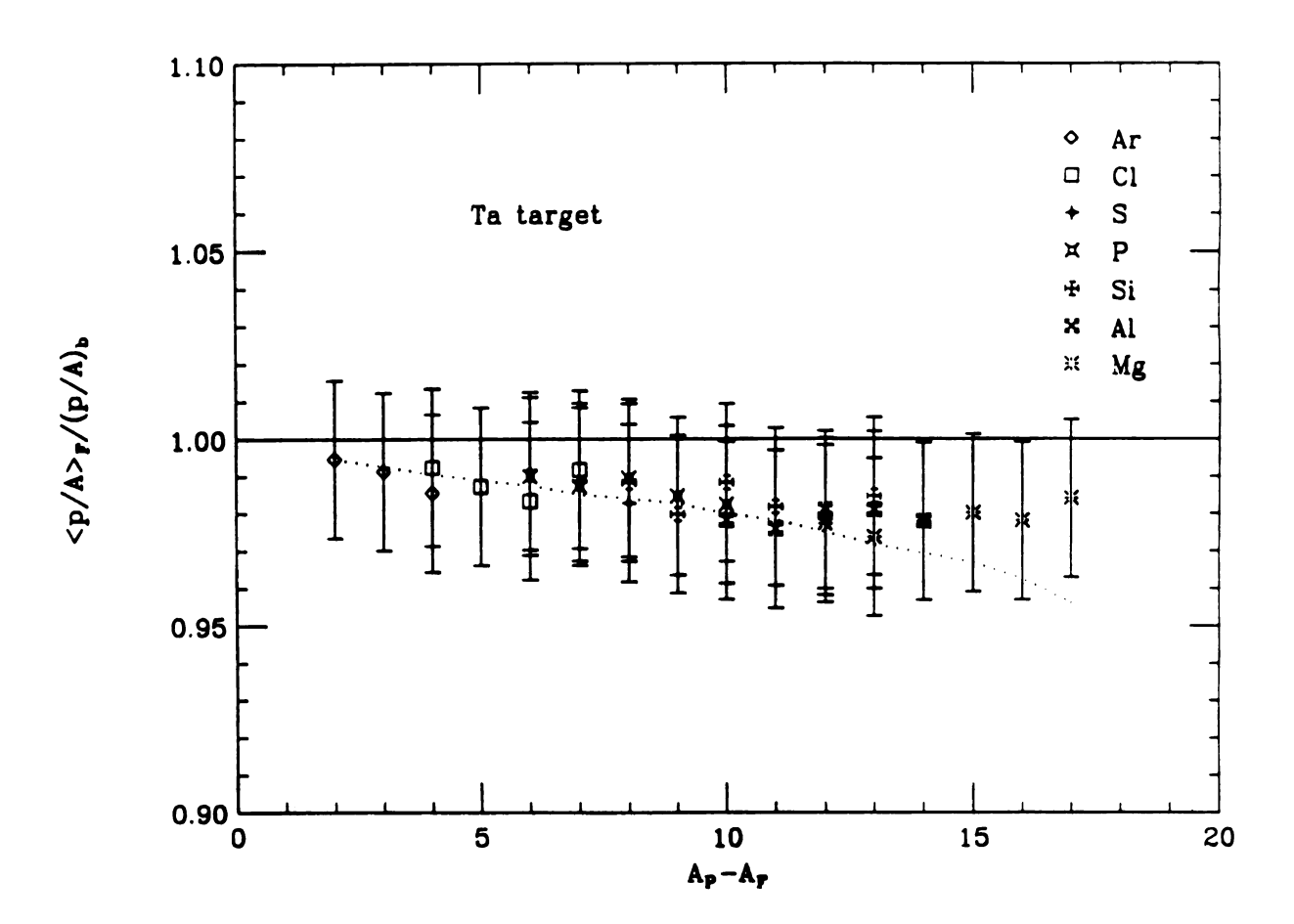


Figure 4.28: The centroids of the momentum distributions(in p/A) of various isotopes relative to the beam momentum/nucleon as function of projectile mass loss. The solid line represent the beam momentum/nucleon measured in the experiment with the same target, the dotted line is from the program calculation

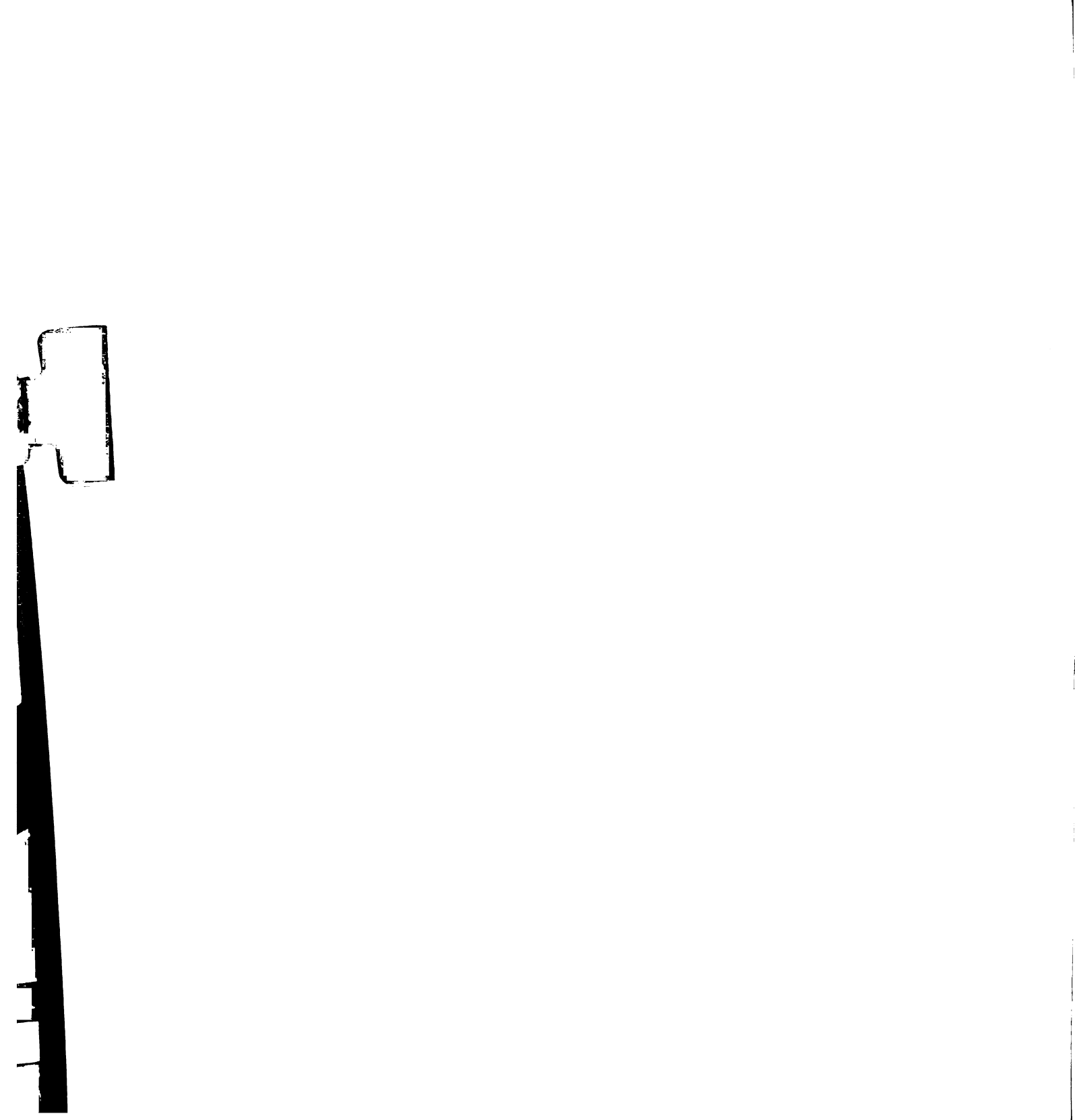
# Chapter 5

## Conclusion

#### I <sup>32</sup>Si half-life

As mentioned in the introduction, there are several previous measurements of the <sup>32</sup>Si half-life. To compare the present work to previous measurements, the result of this experiment (average of the two measurements) is plotted along with those of the other experiment in figure 5.1 [Kut 91]. In the figure, one can see that our result agrees with most of the AMS measurements but disagrees with the geophysical measurements, with the AMS measurement by Hofman et al [Hof 90], and with the real-time decay measurement of Alburger et al [Alb 86]. It is not clear how the present <sup>32</sup>Si half-life results of 132±12 years should be combined with previously published results in order to have the most reliable value of that half-life. Nevertheless, weighing the various data inversely with the square of the stated errors, we obtained 161±3 years. If instead we weigh the results inversely to the stated errors, including only AMS, Decay, and the current work, we obtain 147±4 years. Either value should be adequate for the geophysical applications of <sup>32</sup>Si.

Improvement in the method used in this experiment can be identified by looking at the sources of the uncertainty. As can be seen in table 4.5, statistical uncertainties



are negligible compared with uncertainties in the absolute efficiency of the activity counters and in the determination of the number of nuclei implanted in the sample. For a more accurate determination of the number of nuclei implanted, better separation of isotopes will help to reduce the number of adjacent reaction fragments being implanted, thereby allowing a more direct counting method to be used (such as a thin scintillator in front of the sample). This uncertainty contributed in two ways in the present uncertainty: 1.) in the number of <sup>32</sup>Si nuclei implanted, and 2.) in the number of <sup>32</sup>P nuclei implanted, as discussed earlier, the <sup>32</sup>P activity served to determine the efficiency of the activity counter. For more accurate counting efficiency during activity determination, a more precise control of the depth of implantation would eliminate the need of asymmetrical absorber correction. An accurate theoretical or experimental simulation of the sample-counter system efficiency would also help to reduce the uncertainty. Finally, an anti-muon coincidence setup which is stable over the long term can be developed. As can be seen from table 4.5, the decrease in background will make the sample decay rate determination more accurate.

#### II Momentum distribution

As shown earlier in figure 4.18 and 4.19, discrepancies exist between the experimentally obtained widths of the momentum distributions of various isotopes and the theoretical calculations, but the trends of the data are well reproduced by the model with fitted values of  $\sigma_0$ . The reasons may be as follows:

• The measured widths are obtained by fitting the measured momentum distributions with Gaussian distributions. For some isotopes, the measured distribution is of poor quality near the peak of the distribution due to the interference of a

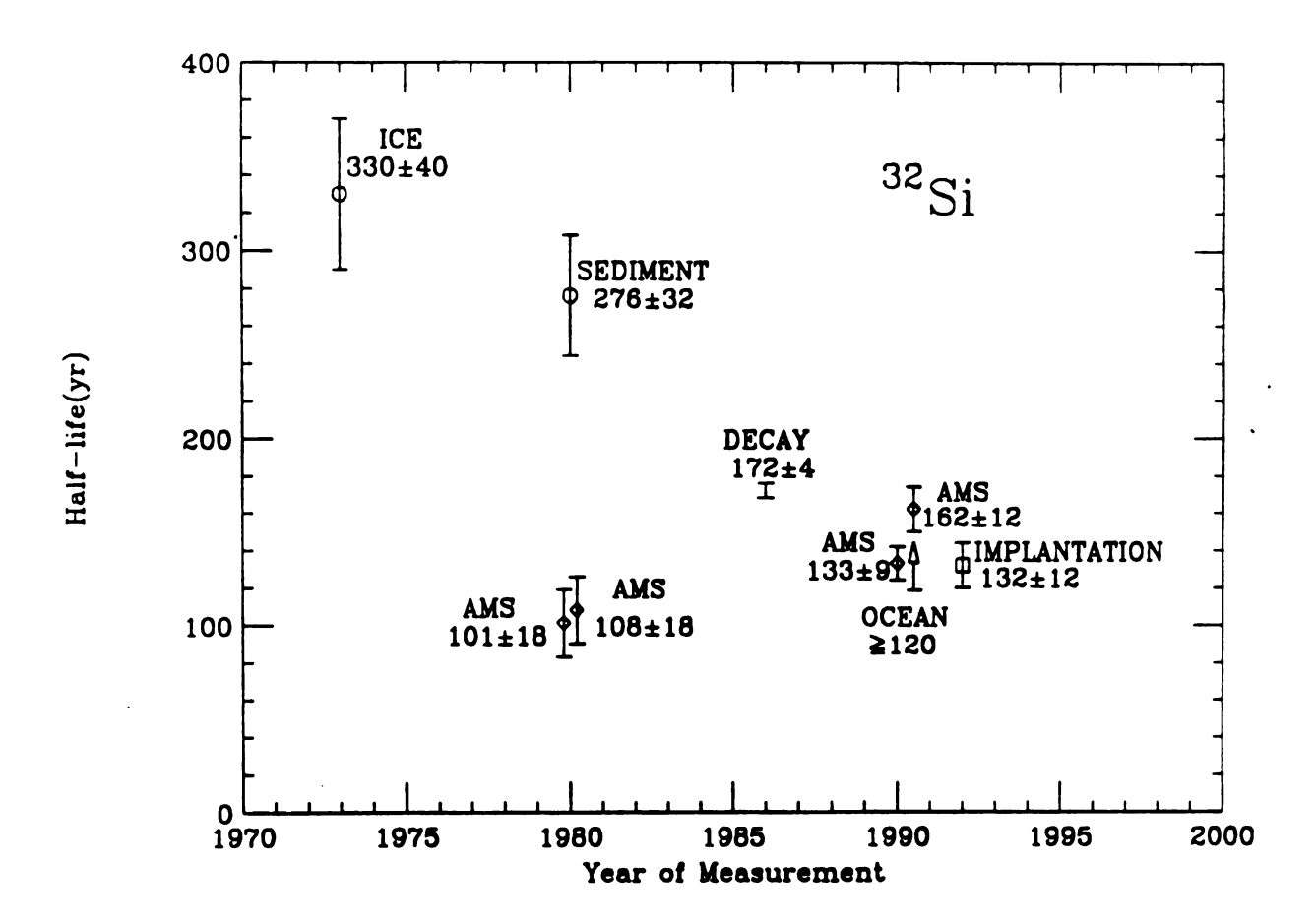


Figure 5.1: Summary of half-life measurements of <sup>32</sup>Si. The results are labeled by the method or the respective natural reservoir, and by the half-life value in years. The results except those from this experiment is taken from [Kut 91]

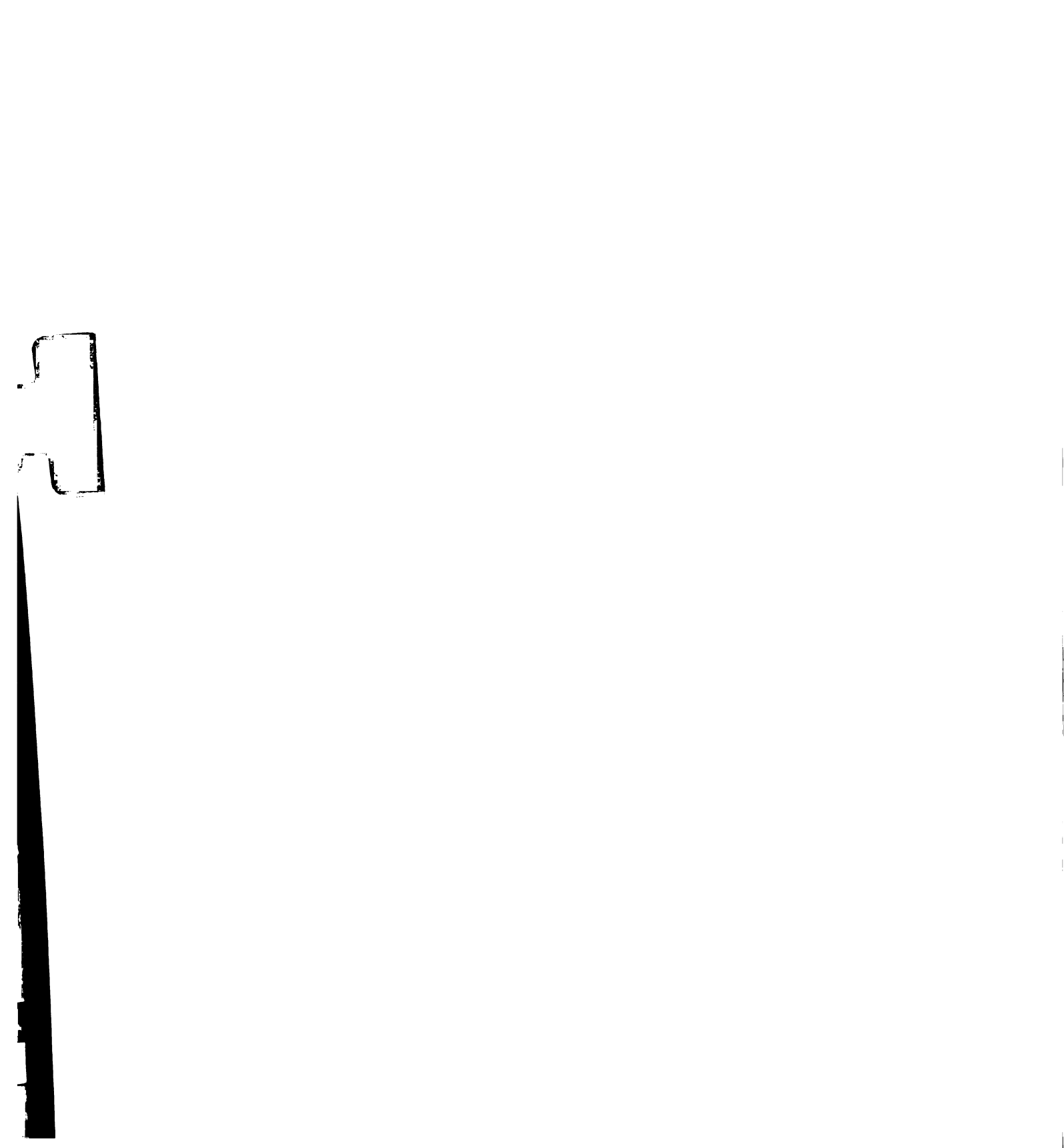
charge state of the beam. As a result, widths extracted are not very accurate. Also since the multiple scattering in the target contributes to the width of the distribution, the latter have to be corrected, and for some isotopes, for example for <sup>30</sup>P, the contribution from the multiple scattering is comparable to the width of distribution, making the intrinsic width of the distribution highly uncertain. Therefore, to improve upon those results, one needs to avoid beam charge states carefully and reduce the thickness of the targets.

• The Goldhaber model [Gol 74] is a simplified statistical model, which takes only the kinematics of the reaction into account. For example, it has been shown by Bertsch [Ber81] that the Pauli exclusion principle between identical nucleons reduces the widths of the observed momentum distributions. This occurs because two nucleons in close proximity tend to have opposite momentum. Therefore, calculations of  $\sigma_0$  using Fermi momentum distribution without taking this into account tend to overestimate the width of the distribution.

For differential reaction cross sections at 0°, the agreement between empirical calculation and experimental results is also not satisfactory. This may be explained by the fact that the calculation is based on parameterization of the data obtained in high energy reactions. It has been observed that at intermediate energies, other reaction channels (such as nucleon transfer) are also involved [Bor 86, Sou 91].

The results of the experiment agree much better with the program calculations in the case of centroids of momentum distributions. This is good news for planning new experiments with the program calculations, because It is very important to know the center of the momentum distribution accurately to setup the A1200 for maximum intensity of the secondary radioactive beam.

In conclusion, a detailed systematic study of the projectile fragmentation reaction at intermediate energy is very important for both theoretical understanding of the reaction mechanism and the purpose of reaction yield prediction. The ability to predicate momentum distribution, both their absolute cross section and shape, is of great practical importance, especially in planning secondary radio active beam experiments.



### References

- [Alb 86] D. E. Alburger, et al, Earth Plan. Sci. Lett. 78, 168 (1986).
- [Baz 90] D. Bazin, D. Guerreau, R. Anne, D. Guillemaud-Mueller, A. C. Mueller, and M. G. Saint-Laurent, Nucl. Phys. A515 (1990) 349.
- [Baz 91] D. Bazin, Private communication.
- [Ber 81] G. Bertsch, Phys Rev. Lett. 46 (1981) 472.
- [Bib 79] K. Van Bibber, D. L. Hendrie, D. K. Scott, H. H. Weiman, L. S. Schroeder, J. V. Geaga, S. A. Cessin, R. Treuhaft, Y. J. Grossiord, J. O. Rasmussen and C. Y. Wong, Phys. Rev. Lett. 43 (1979) 840.
- [Blu 86] Y. Blumenfeld, Ph. Chomaz, N. Frascaria, J. P. Garron, J. C. Jacmart and J. C. Rounette, Nucl. Phys. A455 (1986) 357.
- [Bon 71] J. P. Bondorf, F. Dickmann, D. H. E. Gross, and P.J. Siemens, J. Phys. (Paris) Coll. C6 (1971) 145.
- [Bor 86] V. Borrel, B. Gatty, D. Guerreau, J. Galin, and D. Jacquet, Z. Phys. A Atomic Nuclei 324 (1986) 205.
- [Bro 86] E. Browne, R. B. Firestone, "Table of Radioactive isotopes" p32-2 (John Wiley & Sons, Inc).
- [Cla 73] H. B. Clausen, J. Glaciology 12, 411 (1973).
- [DeM 80] D. J. DeMaster Earth Plan. Sci. Lett. 48 209 (1980).
- [Duf 88] J. P. Dufour et al, Phys. Lett. B206 195 (1988).

- [Ege 81] Ch. Egelhaaf, G. Bohlen, H. Fuchs, A. Gamp, H. Homeyer, and H. Kluge, Phys. Rev. Lett. 46 (1981) 813.
- [Elm 80] D. Elmore et al, Phys. Rev. Lett. 45, 589 (1980).
- [Fri 83] W. A. Friedman, Phys. Rev. C 27 (1983) 569.
- [Fox 89] R. Fox, R. Au, and A. VanderMolen, IEEE Trans. Nucl. Sci. (1989) 1562.
- [Gel 78] C. K. Gelbke, C. Olmer, M. Buenerd, D. L. Hendrie, J. Mahoney, M. C. Mermaz, D. K. Scott, Phys. Rep. 42 (1978) 311.
- [Gol 74] A. S. Goldhaber, Phys. Lett. 53B (1974) 306.
- [Gol 78] A. S. Goldhaber and H. H. Heckman, Z Ann. Rev. Nucl. Part. Sci. 28 (1978) 161.
- [Gre 75] D. E. Greiner, P. J. Lindstrom, H. H. Heckman, Bruce Cork, and F. S. Bieser, Phys. Rev. Lett. 35 (1975) 152.
- [Gre 75] D. E. Greiner, P. J. Lindstrom, H. H. Heckman, Bruce Cork, and F. S. Bieser, Phys. Rev. Lett. 35 (1975) 152.
- [Gue 83] D. Guerreau, V. Borrel, D. Jacquet, J. Galin, B. Gatty and X. Tarrago, Phys. Lett. 131B (1983) 293.
- [Hec 72] H. H. Heckman, D. E. Greiner, P. J. Lindstrom and F. S. Bieser, Phys. Rev. Lett. 28 (1972) 926.
- [Hof 90] H. J. Hofmann et al, Nucl. Instr. & Meth. B52, 544(1990).

- [Hom 84] H. Homeyer, M. Bürgel, Ch. Egelhaaf, H. Fuchs, and G. Thoma, Z. Phys. A Atoms and Nuclei 319 (1984) 143.
- [Huf 85] J. Hüfner, Phys. Rep. 125 (1985) 129.
- [Kno 89] G. F. Knoll, "Radiation Detection and Measurement" p718 (John Wiley & Sons, Inc. 1989).
- [Kut 80] W. Kutschera et al, Phys. Rev. Lett. 45, 592 (1980).!
- [Kut 86] W. Kutschera, Nucl. Instr. & Meth. B17, 377(1986).
- [Kut 91] W. Kutschera, to be published in RADIOCARBON.
- [McV 80] K. W. McVoy, M. C. Nemes, Z. Phys. A Atoms and Nuclei 295 (1980) 177.
- [Mon 71] E. J. Moniz, I. Sick, R. R. Whitney, J. R. Ficenec, R. D. Kephart, and W. P. Trower, Phys. Rev. Lett. 26 (1971) 445.
- [Mor 79] D. J. Morrissey, L. F. Oliveira, J. O. Rasmussen, and G. T. Seaborg, Phys. Rev. Lett. 43 (1979) 1139.
- [Mor 89] D. J. Morrissey, Phys. Rev. C 39 (1989) 460.
- [Mor 91] D. J. Morrissey, Private communication.
- [Mur 83] M. J. Murphy, R. G. Stokstad, Phys. Rev. C 28 (1983) 428.
- [Mus 84] et al, Phy. Rev. Lett. 53, 2544 (1984).
- [Oli 79] L. F. Oliveira, R. Donangelo, J. O. Rasmussen, Phys. Rev. C 19 (1979) 826.
- [She 89] B. M. Sherrill, W. Benenson, D. Mikolas, D. J. Morrisey, J. A. Nolen and J. A. Winger, in *Proceedings of the 1st International Conference on Radioactive Nuclear*

- Beams, Oct. 1989, Berkeley, California, edited by W. D. Myers, J. M. Nitschke, and E. B. Norman, (World Scientific, 1990), p. 72.
- [Sil 88] J. D. Silk, H. D. Holmgren, D. L. Hendrie, T. J. M. Symons, G. D. Westfall, P. H. Stelson, S. Raman, R. L. Auble, J. R. Wu and K. Van Bibber, Phys. Rev. C 37 (1988) 158.
- [Som 91] Somayajulu et al, Earth and Planetary Sci Letters, to be published.
- [Sou 91] G. A. Souliotis, D. J. Morrissey, and B. M. Sherrill, Rev. Sci. Instrum. 62 (1991) 342.
- [Sum 90] K. Sümmerer and D. J. Morrissey, in Proceedings of the 1<sup>st</sup> International Conference on Radioactive Nuclear Beams, Oct. 1989, Berkeley, California, edited by W. D. Myers, J. M. Nitschke, and E. B. Norman, (World Scientific, 1990), p. 122.
- [Swa 91] D. Swan Private communication.
- [Tho 92] M.S. Thomsen et al, Nucl. Phys. A534 327 (1991).
- [Viy 79] Y. P. Viyogi, T. J. M. Simons, P. Doll, D. E. Greiner, H. H. Heckman, D. L. Hendrie,
  P. J. Lindstrom, J. Mahoney, D. K. Scott, K. Van Bibber, G. D. Westfall, H. Wieman,
  H. J. Crawford, C. McParland, and C. K. Gelbke, Phys. Rev. Lett. 42 (1979) 33.
- [Win 91] J. A. Winger, B. M. Sherrill, and D. J. Morrissey, Proc. EMIS Conf. (1991), in press.
- [Zel 85] A. F. Zeller, R. T. Swanson, J. A. Nolen, D. Landry, M. J. Dubois and J. C. Dekamp, in Proceedings of the 9<sup>th</sup> International Conference on Magnet Technology (1985), edited by C. Mazinucci and P. Weymuth (Swiss Institute for Nuclear Research, Zurich, 1985), p. 160 and J. C. Dekamp, C. T. Magsig, J. A. Nolen and A. F. Zeller, IEEE Trans. in Mag., MAG-23 (1987) 524.
- [Zem 71] H. Zemann et al, Nucl. Phys. A175 385 (1971).